AMERICAN UNIVERSITY OF BEIRUT

SYNTHESIS OF NEW ZINC OXIDE AND GOLD
NANOPARTICLES CONJUGATED TO CURCUMIN FOR
ENVIRONMENTAL AND BIOMEDICAL APPLICATIONS

by
RASHA NAWAF MOUSSAWI

A thesis
submitted in partial fulfillment of the requirements
for the degree of Master of Science
to the Department of Chemistry
of the Faculty of Arts and Sciences
at the American University of Beirut

Beirut, Lebanon
December 2014

AMERICAN UNIVERSITY O`F BEIRUT

# SYNTHESIS AND CHARACTERIZATION OF NOVEL ZINC OXIDE AND GOLD NANOPARTICLES CONJUGATED WITH CURCUMIN TOWARDS ENVIRONMENTAL AND BIOMEDICAL APPLICATIONS.
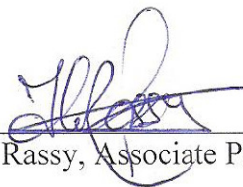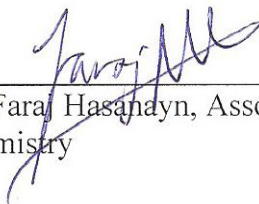
by
## RASHA NAWAF MOUSSAWI

Approved by:

_____

Dr. Digambara Patra, Associate Professor         Advisor
Chemistry

_____

Dr. Houssam El Rassy, Associate Professor       Member of Committee
Chemistry

_____

Dr. Faraj Hasanayn, Associate Professor       Member of Committee
Chemistry

Date of thesis defense: Dec 10, 2014

# AMERICAN UNIVERSITY OF BEIRUT

# THESIS, DISSERTATION, PROJECT RELEASE FORM

Student Name:

_____

               Last                            First                     Middle

◯ Master's Thesis        ◯ Master's Project        ◯ Doctoral Dissertation

☐     I authorize the American University of Beirut to: (a) reproduce hard or electronic copies of my thesis, dissertation, or project; (b) include such copies in the archives and digital repositories of the University; and (c) make freely available such copies to third parties for research or educational purposes.

☐     I authorize the American University of Beirut, **three years after the date of submitting my thesis, dissertation, or project,** to: (a) reproduce hard or electronic copies of it; (b) include such copies in the archives and digital repositories of the University; and (c) make freely available such copies to third parties for research or educational purposes.

_____

Signature                          Date

# ACKNOWLEDGMENTS

# AN ABSTRACT OF THE THESIS OF

Rasha Nawaf  Moussawi    for Master of Science
                         Major: Chemistry

Title:   Synthesis of new zinc oxide and gold nanoparticles conjugated with curcumin for environmental and biomedical applications

Curcumin-conjugated ZnO nanostructures (Zn(cur)O) were synthesized through a simple precipitation method where the curcumin employed during the synthesis process got conjugated to ZnO through strong interactions. The compound was characterized with SEM, FTIR, XRD, ZP, UV–Vis absorption spectroscopy, and photoluminescence spectroscopy. The absorption spectra confirmed sensitization of ZnO to the visible light. Photoluminescence properties of Zn(cur)O and ZnO were compared and found that exciton emission was enhanced in Zn(cur)O and the visible emission suppressed. The environmental potential application of the compound was explored by removing toxic pollutants as arsenic and three PAHs from water samples.  High concentrations of perylene, fluoranthene, and chrysene were removed faster using the modified ZnO than bare ZnO depending on the extent of curcumin incorporated during synthesis. The degradation was found to be faster for PAHs having less number of aromatic rings; with 167 mg/L Zn(cur)O loading, 93% removal of 11.4 µg/L fluoranthene after 25 minutes was achieved, 88% for 12.6 µg/L perylene after 3.4h, and 93% for 11.1 µg/L chrysene after 2.2h . Adsorption and fluorescence sensing potential was also tested on arsenite. With relatively low material loading (43 ppb), the Zn(cur)O nanostructures removed As(III) below the minimum contamination level (MCL) from 100 ppb samples within 30 minutes. The compound reached up to 75% removal/adsorption capacity with 903 ppb concentrations after 3 hours with the same loading. Bare ZnO didn't bring down the arsenic contamination below its MCL even after 3 hours. Kinetics of adsorption fitted very well to pseudo second order model with exceptional adsorption rates that reflected the high affinity of the compound to As(III). These results presented the compound as an attractive alternative for a simple single-step treatment option to treat arsenic-contaminated natural water with high adsorption rates without the pre-treatment requirement for current industrial and environmental practices. Monitoring the curcumin's fluorescence with increasing arsenite concentrations showed a linear response up to 3 ppm revealing a potential for applying it as an optical As sensing material. Gold nanorods were synthesized through the seed mediated method where curcumin was used as the reducing agent. When CTAB-capped gold seeds were used, high aspect ratio NRs (15) along with nanospheres were obtained. When citrate capped seeds were used, polydisperse NRs and shape contaminations resulted. The visualization of micellar templates in SEM images seemed to stress the micelle-templated growth of nanorods over the preferential binding of CTAB onto specific gold facets. The addition of silver resulted in different outcomes depending on the capping agent of the seed used; the hydrophobic interaction of the CTAB alkyl chain with curcumin prevented its interaction with silver whereas such an interaction couldn't be

avoided with citrate capped seeds which prevented the reduction of curucmin at the gold surface and consequently hindered any NRs formation. Curcumin conjugated nanoparticles proved to yield nanorods in principle. The Resonance Rayleigh Scattering response for curcumin conjugated NPs showed a linear increase with increasing concentrations of RNA and DNA which rendered the method eligible for their determination in the concentration range
3.33μg/mL – 100μg/mL.

# ILLUSTRATIONS

# TABLES

# CONTENTS

# CHAPTER I
# INTRODUCTION

The study of nano-scale particles is driven by the change in physical and chemical properties as compared to those of the bulk. The size, shape, and surface properties of nanoparticles dictate the physicochemical properties of nanomaterials and consequently their applications. The design of functional nanomaterials has fueled the advance of nanomaterials and nanotechnology through the production of special materials with novel properties for potential applications in chemical, biological, and technological domains. Modifications to nanoparticles are done through incorporation of organic and inorganic systems on the surface of these nanoparticle or embedding in polymer matrices to yield hybrid materials with novel properties and functions[1-2]. For inorganic systems, the proper surface functionalization enhances their stability, biocompatibility and functionality in physiological environments enabling their targeted use in bioapplications. For instance, organic-inorganic hybrid nanomaterials exhibited a promising potential for imaging and therapeutic applications[3]. Other organically modified metal oxide matrices have demonstrated great potential to make optical devices[4]. One important requirement for the environmental and/or biomedical applications of these modified nanomaterials is their established safe profile. Among inorganic systems, the systems we chose to work with are zinc oxide and gold nanoparticles, both of which have demonstrated biocompatibility and are already employed in many biomedical applications. However, for instance, gold nanoparticles (AuNPs) where citrate[5], CTAB[6], and PEG[7] are used in the synthesis have limited utilization in biomedicine due to their demonstrated toxicity. Thus, nontoxic modifiers

are needed. Furthermore, modifiers with the added advantage of being readily available and cost-effective for various practical applications become challenging to find. For instance, a modifier with these characteristics is especially desirable for the biomedical and environmental applications for zinc oxide. ZnO absorbs only in UV (wide band gap ~3.37 eV at room temperature)[8] which limits some of its applications (e.g. photocatalysis) and thus sensitization of ZnO towards the visible light or in other words narrowing its band gap or splitting it into sub-gaps is required. This have been done through various methods such as creating oxygen vacancies[9-10], semiconductor coupling[11], metal and non-metal doping, and surface modification by incorporation of organic materials[12-13] such as fullerenes [14] and polymers[15-16]. There is good research on the optical properties of polymer doped ZnO[17] and surface modification of ZnO by polymers [16], however, research work on dye sensitized zinc oxides and their respective optical and catalytic properties remains limited. The search for a safe, readily available, and cost-effective sensitizer has prompted the research on natural dyes obtained from plant sources and sensitizers such as chlorophyll derivatives, natural porphyrins[18] and anthocyanins [18-22] have been investigated. A natural dye, which is worth to investigate is curcumin. Curcumin or diferuloylmethane (1,7-bis-(4-hydroxy-3-methoxy-phenyl)-hepta-1,6-diene-3,5-dione), a polyphenolic diketone, is an active constituent of the spice turmeric obtained from the dried root of the perennial herb *Curcuma longa* cultivated extensively in Southeast Asia, India, China, and other countries with a tropical climate. Curcumin is an orange-yellow pigment fraction of turmeric containing mixture of curcuminoids that are almost insoluble in water but highly soluble in organic solvents. Curcumin accounts as the major component (approx. 77 %) in the curcuminoid complexes[23]. It is easy to extract, applicable without further

2

complicated purification and is already used a nontoxic food additive. Curcumin has high thermal and chemical stability and an intense long wavelength absorption in the visible region of 420–580 nm. Curcumin is well-known for its pharmaceutical applications and medicinal potential in therapy of many diseases such as cancer[24], cardio-vascular disease[25], and rheumatoid arthritis[26]. These features highly nominate curcumin as a promising natural dye sensitizer to extend visible light response of ZnO.  It should be noted, however, that the optimum potential of curcumin is limited by its lack of solubility in aqueous solvents, its poor bioavailability, and lack of targeted specificity. Of the attempts to improve on these limitations was its encapsulation with nanoparticulate formulation[27] or immobilization unto polyelectrolyte multilayer (PEM) thin films[28].

The structural formula of curcumin is shown in Fig. 1.1, it exists in 2 forms: the keto form which is the dominant form in the solid phase and the enol form in the aqueous phase. There are two kinds of acidic hydrogens in curcumin[29]; one is a phenolic hydrogen, the other is an active methylene hydrogen of β-diketones. The pka values for the dissociation of these acidic protons in curcumin were reported to be 7.80, 8.5 and 9.0, respectively.
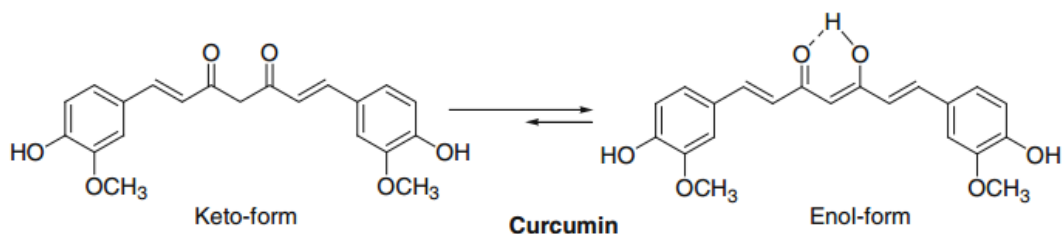


**Figure 1.1: Tautomers of curcumin**

ZnO presented itself as a special material with great potential and thus has attracted

research to study this semiconductor in the form of powders, single crystals, thin films,

or nanostructures. ZnO has a high binding exciton emission (60 meV) at room

temperature[30]. ZnO is biocompatible, chemically stable, and environmentally friendly

rendering it suitable for biomedical and environmental applications such as, transparent

conducting electrodes in solar cells[31] , photocatalysts for degradation of organic

pollutants in wastewaters [32], UV lasers[33], and chemical and biological sensors[34].

ZnO occurs as the rare mineral zincite, usually appearing as a white powder, it's

almost insoluble in water but soluble in acids and alkali. It crystallizes in three different

structures[35]: wurtzite, zincblende and rocksalt. The wurtzite structure (Fig. 1.2c) of

ZnO is the thermodynamically stable phase; the two other structures of ZnO, the

zincblende (Fig. 1.2b) and the rocksalt (Fig. 1.2a) are metastable and only occur under

certain conditions. The zincblende structure is obtained through epitaxial growth of

ZnO on a suitable cubic substrate, while the rocksalt (NaCl-type) structure is observed

when subjected to high pressures (~9 GPa at 300 K). Nearly all photocatalytic studies

are focused on the wurtzite structure.
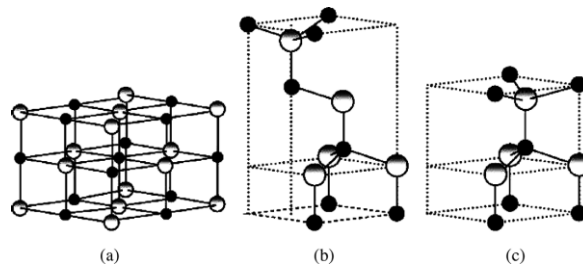


**Figure 1.2: Stick and ball representation of ZnO crystal structures: (a) cubic rocksalt; (b) cubic zincblende; (c) hexagonal wurtzite. The shaded white and black spheres denote Zn and O atoms, respectively[36].**

Various methods are used to synthesize ZnO nanostructures with different morphologies, sizes, and functionalities, such as vapor phase transport[37], hydrothermal process[38] , chemical solution[39], metal-organic CVD (MOCVD)[40], chemical vapor deposition[41] and template-directed growth[42].

Reports on curcumin as sensitizer are scarce. Among those few[43] reported that curcumin-derived dye can be used as a sensitizer in dye sensitized solar cells (DSSC) with photocurrent density of 1.66 mA cm$^2$. Curcumin has very exciting photophysical and fluorescence properties in heterogeneous environments[44]. It can make metal complex to various metal ions[45-47]. It also makes a Zn-curcumin complex by reacting with zinc salt [48-49]. Recently Khalil et al have reported synthesis of ZnO from a curcumin zinc precursor[49]. Hariharan et al have anchored curcumin and its metal complexes on the surface of ZnO/PVA nanocomposites by vacuum evaporation method[16]. In this work we attempted to prepare a new curcumin-zinc oxide material where curcumin was incorporated with ZnO during the synthesis process through the hydrothermal method. The first part of this thesis constitutes the work on curcumin-conjugated ZnO nanostructures (Zn(cur)O); its synthesis and characterization by SEM, FTIR, XRD, ZP, UV–Vis absorption spectroscopy, and photoluminescence spectroscopy. Known for its adsorption capacity and photocatalytic activity, the potential of the new material was tested for environmental applications, specifically on removing carcinogenic pollutants as arsenic and three selected polycyclic aromatic hydrocarbons (PAHs); namely chrysene, fluoranthene, and perylene from water.

Nanostructures made of noble metals, such as gold, have attracted intense research because of their fascinating optical, electronic, and chemical properties as well as biocompatibility[50-51]. These properties in addition to the photo-stability and ease of functionalization of gold nominate it as an ideal candidate for promising applications in nano-electronics, biomedicine, sensing, and catalysis [52-53].  In addition, gold is suitable for basic research because it holds a simple face-centered cubic (fcc) crystalline structure which would render the understanding of growth processes easier. The interesting optical properties of metals in general stem from the excitation of the free electrons on their surface which results in surface plasmon resonance (SPR)[54-61]. Factors such as the particle's size, shape, and particle-to-particle interaction dictate the surface plasmon modes of metal nanoparticles [62-73]. Anisotropic (non-spherical shapes constituting nanocubes, nanoprisms, nanorods, and nanowires) particles allow for a greater degree of tunability of the SPR while keeping almost the same volume in comparison to spherical particles that show a limited tunability accompanied with a significant change in volume. For example, spherical Au particles spanning a diameter of 10 to 100 nm (volume changes by 1000 times) show a ∼50 nm tunability of SPR wavelength (520 to -570 nm)[74]. This same tunability, on the other hand, is attained for Au nanorods when a slight change in aspect ratio (length-to-diameter ratio AR) from ∼2.5 to ∼3 (volume increases only by a factor of 1.2) can lead to a 50 nm red shift of the longitudinal plasmon mode. This high tunability of anisotropic particles is due to their "extreme sensitivity to factors such as particle shape (e.g., nanorods), the shape anisotropy (e.g., aspect ratio of nanorods), and tip truncation (e.g., the case of nanoprisms)[75-78]. Various wet chemical techniques have been established to produce gold nanoparticles with various shapes such as rods[79-81], wires[82-83], plates[84-85],

prisms[86-87], cubes[88], polyhedral [89-90], and branched particles[91-92]. The first

encountered anisotropic nanostructures were the rod-shaped nanoparticles in late 1990s.

A "nanorod" is defined to be a nanoscale particle with an aspect ratio (length/width

ratio) that is between 1 and ~20–25; higher aspect ratio materials we will call

"nanowires" (as long as the diameter is less than ~100 nm)[93]. Spherical gold NPs in

the range ~5–50 nm (in diameter) show one plasmon band at ~520 nm in aqueous

solution. On the other hand, nanorods' optical properties are mainly controlled by the

rods' aspect ratio and would show two plasmon bands attributed to light absorption (and

scattering) along the long axis ("longitudinal plasmon band") and the short axis

("transverse plasmon band") of the rods. The position of the plasmon band is affected

by the environment's local polarizability and the aggregation state of the particles. As

the aspect ratio increases, the position of the longitudinal plasmon band red-shifts, and

the transverse plasmon band position stays relatively constant at ~520 nm. Gold

nanorods of moderate aspect ratio (2–5) display plasmon bands with tunable maxima

from ~700 to 900 nm, and high-aspect ratio nanorods (>5)exhibit a longitudinal

plasmon band past 1500 nm [94-97].


As the plasmon is created upon light absorption, it gives rise to large electric

fields near the nanoparticle surface, enhanced particularly at the tips for nanorods. The

applications for such an enhancement means an improved sensitivity for chemical

sensing such as surface-enhanced Raman scattering (SERS), where the Raman signals

from molecules increase enormously in intensity, if the molecules are in close

proximity (within ~10 nm) of a metal nanoparticle surface[97-99]. Such an

enhancement has been utilized in specific molecular diagnosis of cancer. Also the

tunability of the plasmon band position of nanorods by changing its AR promises to have huge potential in biological applications. Gold nanorods serve as promising tools for photothermal targeted therapy, in which near-infrared light illumination leads to heat that can destroy diseased cells[100-105]. This's attributed to the tunability of the plasmon band to the near-infrared "water window" of the tissue and the large extinction coefficients of the plasmon bands of gold nanorods leading to strong absorption, followed by heat release to the environment. The strong light absorption and scattering are utilized for disease detection through optical cellular imaging. Of course, issues of toxicity, biodistribution, and metabolism must be addressed for true in vivo applications. Full realization of gold nanorods potential in all of these applications requires improvements in fundamental understanding of the crystal growth processes that allows controllable rods synthesis [67,106]. For example, it is not yet possible to know a priori what specific reaction conditions will yield gold nanorods with 5 nm in diameter and AR corresponding to light absorption at 1200 nm.

Gold nanorods can be obtained via many ways, from lithographic deposition of thin gold films on a substrate followed by various chopping procedures[107], to electrochemical deposition in hard nanotube templates[108-109], to photochemical reactions in solution[81]. The seed mediated method is the state of art synthesis of gold nanorods introduced by Murphy and co-workers [80]. It's a multistep controlled redox reaction that is performed at room temperature aqueous solution which generally involves two main steps[80]. The method utilizes small spherical seed particles (~1.5–4 nm diameter) that are first synthesized from~$10^{-4}$ M gold salt (HAuCl$_4$) and excess strong reducing agents agent (e.g., sodium borohydride) to promote isotropic growth over anisotropic growth in the presence of a stabilizing agent (citrate or

cetyltrimethylammonium bromide CTAB). These seed particles are then added to a growth solution that contains additional gold salt, a weak reducing agent, and a "structure-directing agent" to control the final particle shape. The choice of the reducing agent determines to a great extent the rate of formation of the nanorods and the final shape and anisotropy. Ascorbic acid is the secondary mild reducing agent usually used because it is too weak to reduce the additional gold salt in the growth step from $Au^{3+}$ to $Au^{0}$ alone. This allows for the growth to occur over a long time (minutes to hours), which aids in anisotropic growth. The structure directing agent used is CTAB, a cationic surfactant well-known to form rod like micelles on its own in water[80].

What Murphy and co-workers did specifically in their work is that they synthesized - through optimizing the concentration of CTAB and ascorbic acid - high aspect ratio nanorods (low yield of 4%) using 3.5-nm gold seed particles reduced by sodium borohydride in presence of citrate that acts as a capping agent. Later on, they improved the method to obtain monodisperse gold nanorods of high aspect ratio in high yield (~90%) [110], just through pH control. The pH of the growth solution was adjusted to 3.5 and 5.6 (previously was 2.8), and resulted in forming gold NRs of aspect ratio 18.8±1.3 and 20.2±1.2, respectively. For high aspect ratio rods (aspect ratio ~20) where rods of increasing aspect ratios (from ~4 to 18) can be obtained [80], also a three-step seeding method is used where the timing of the reaction in each step is adjusted. The general procedure starts with preformed seed particles, as described above, and three sets of growth solutions containing additional gold salt and CTAB. The first growth solution is seeded with the seed particles; 10–15 s later, an aliquot of this solution is used as the seed for the next growth solution; and so on. After three steps of seeding, gold nanorods of aspect ratios ~18 can be obtained, albeit in low absolute yield (~4%).

A main disadvantage of this method is the large proportion of gold nanospheres and other shapes that are formed, greatly reducing the yield of rods. Purification of the longest rods relies on gravity for their slow settling out of solution.

The factors controlling or affecting shape control are not yet well defined and many efforts have been made to understand the mechanism of the growth process. Aspect ratio, monodispersity, shape, and the yield of the gold nanorods were demonstrated to be influenced by a number of factors, such as the stability of the seed, temperature, and the nature and concentration of surfactant. For instance, the choice of the capping agent used for Au seed was found to be an important factor that affects the yield of nanorods since it affects the crystal structure of the seed itself. Jana et al. used citrate-stabilized seeds and obtained a low nanorod yield ($\sim$15%)[80]. The method was optimized later on by Nikoobakht and El-Sayed by using CTAB-stabilized Au seeds overcoming much of the limitations of the previous method such as formation of $\varphi$-shaped particles, which appear as hybrids between spheres and rods, in addition to contamination by spherical particles. The method yielded outstanding $\sim$99% nanorods where AR could be tuned from 1.5 up to 5. HR-TEM studies have indicated that the CTAB-capped seeds used for nanorod growth are single crystalline with well-developed facets [111]. Single crystalline (as opposed to penta-twinned) nanorods are produced if CTAB protected Au seeds, rather than citrate capped seeds, are employed in the growth process. The surfactant structure including the choice of the head group, hydrocarbon chain length, and counterion is found to play a crucial role in preparing these high aspect ratio gold nanorods. For example, having $CTA^+$ cation kept intact, bromide was found to be far superior to chloride or iodide for nanorod production[11].

In the silver-assisted method, the amount of silver nitrate added affects the final aspect ratio of the rods [79]. The resulting rods cannot be used in multistep as seeds to grow longer rods as their silverless counterparts; rather the synthesis must be repeated with a higher concentration of silver nitrate to obtain higher aspect ratio gold NRs. Low aspect ratio nanorods (~1–6), (up to ca. 90 nm in lengths) starting from 1.5 nm CTAB capped Au seeds [97,112] can be synthesized with high yield (~90%) after two rounds of purification by centrifugation[93]. Nonetheless, the overall yield relative to the initial gold ions is less than 15% [79]. The excess unreduced metal ions and CTAB are thought to be important in promoting anisotropic growth as it's noticed that reducing the concentrations of all reagents in the synthesis decreases nanorod yields.

Monodisperse tunable Au NRs with negligible shape impurities (<1% of the total number of particles) were obtained with aromatic additives. This account of research, in addition to the known reducing ability of curcumin and its safe profile for biomedical and environmental applications, made it attractive to use this molecule in the synthesis of nanorods as a reducing agent and to test if it had similar effects as the aromatic additives reported earlier. Research on the seed mediated method have studied the effects of many parameters including the gold seed, concentration of reactants, temperature, duration of growth, additives…etc. [74,110,113-115]. However, little research is done on the nature of the reducing agent. In this work we altered the conventional reducing agent (ascorbic acid) with curcumin and we systematically changed some reaction variables, such as pH, concentrations of reactants, addition of silver, and the capping of the gold seed. These modifications had been carried out to explore any distinctive features arising and to help gain a better understanding of the reaction mechanism hoping it serves one of the aims of materials science in defining

and understanding the mechanisms that eventually dictate crystal shape for better

design.

# CHAPTER II
# SYNTHESIS, CHARACTERIZATION, AND PHOTOLUMINESCENCE OF CURCUMIN CONJUGATED ZINC OXIDE NANOSTRUCTURES

## A. Experimental

### 1.  Materials

Zinc nitrate hexahydrate ($Zn(NO_3)_2 \cdot 6H_2O$, 98% extra pure was obtained from Acros Organics, curcumin was obtained from Sigma, acetone (HPLC grade) was obtained from Sigma Aldrich and potassium hydroxide from AnalaR. All the solutions were prepared with deionized water unless otherwise mentioned.

### 2. Synthesis

Zn(cur)O was prepared by taking 0.5 mg (0.001 mmol), 1.0 mg (0.0027 mmol), 1.5 mg (0.004 mmol), or 2.0 mg (0.0054 mmol), of curcumin in 50 mL of double distilled water (close to neutral pH) at $80 - 90$ $^{o}$C. When curcumin was solubilized completely, 50 mL of 0.1 M $Zn(NO_3)_2$ (5 mmol) solution prepared in double distilled water was added to it. The yellowish solution was refluxed for 1 hour at 85-90 $^{o}$C. After that, the solution was cooled down and 5 mL of 0.2 M KOH (1 mmol) was added slowly at 4 $^{o}$C. An orange yellow gel-like suspension was observed. The solution was centrifuged at 5000 rpm and the precipitate was washed with water till no more yellow color was observed in the supernatant. Acetone washes were necessary to remove any unanchored curcumin after which the final wash was with water. The precipitate Zn(cur)O was vacuum dried at room temperature. A control ZnO was synthesized by taking 50 mL of 0.1 M $Zn(NO_3)_2$ solution prepared in double distilled water and then

adding 5 mL of 0.2 M KOH slowly in an ice bath at 4 $^{o}$C. The white suspension was centrifuged at 5000 rpm, washed with water and vacuum dried just like Zn(cur)O . In another control experiment, ZnO anchored with curcumin (cur@ZnO) was prepared by adding 2 mg of curcumin to the white ZnO obtained from the above procedure. The mixture was refluxed for 3 hours at 85 -90 $^{o}$C. A yellow solid precipitated and was centrifuged and washed with water at 5000 rpm. The yellow precipitate was also washed with acetone to remove unbound curcumin. It's worth noting that for Zn(cur)O only one acetone wash was enough for any unbound curcumin to come out, while for cur@ZnO, curcumin kept coming out and the supernatant kept appearing yellowish even after several washes with acetone. The precipitate appeared lighter in color (whitish yellow) with every wash.

### 3. Characterization

The apparent zeta potential was measured using a Malvern Zetasizer Nano ZS (M3-PALS) using the Non-Invasive Back Scatter technique. The instrument was equipped with a monochromatic red laser operating at 632.8 nm and the data were analysed with the Malvern Dispersion technology software. Z-average values for three measurements were recorded. The Thermogravimetric Analysis (TGA) and Differential Scanning Calorimetry (DSC) measurements were done using a Netzsch TGA 209 in the temperature range 0 to 800 $^{o}$C with an increment of 30 K/ 10 minutes in a $N_2$ atmosphere. Scanning electron microscopy (SEM) analysis was carried out using Tescan, Vega 3 LMU with Oxford EDX detector (Inca XmaW20) SEM. The sample was deposited on a carbon film for SEM analysis. Transmission electron microscopy (TEM) measurement was carried out with a JEOL 2200FS double aberration corrected

FEG microscope, operating at 200 kV. TEM samples were prepared by casting a drop of the nanoparticle suspension onto copper grids covered with holey carbon films. The fluorescence image was recorded using a high sensitive STED confocal set up consisted of confocal microscope (Leica TCS SP5 STED, Leica Microsystem), APD detector and an Argon laser with 430 nm excitation wavelength. Zn(cur)O was excited by a wavelength of 430 nm and typical emission wavelengths were 490 –600 nm. The X-Ray Diffraction (XRD) data were recorded using a Bruker d8 discover X-Ray diffractometer equipped with Cu-Kα radiation (λ = 1.5405 Å). The monochromator used is Johansson Type. The step size is 0.02 s and the scan rate is 20 s per step.

Zn(cur)O, ZnO and cur@ZnO were srudied by FTIR spectroscopy. A Thermo Nicolet 4700 Fourier Transform Infrared Spectrometer equipped with a Class 1 Laser was used for this purpose. The KBr pellet technique is applied to perform the transmission experiments in the range between 4000 and 400 $cm^{-1}$. The absorption spectra were recorded at room temperature using a JASCO V-570 UV-VIS-NIR Spectrophotometer. UV-visible Diffuse Reflectance spectra were measured using a JASCO V-570 UV-VIS-NIR Spectrophotometer in the range 200 to 800 nm. The steady-state fluorescence spectra (excitation and emission) were recorded at room temperature using Jobin-Yvon-Horiba Fluorolog III fluorometer and the FluorEssence program where the excitation and emission slits width were 5 nm. The source of excitation was a 100 W Xenon lamp, and the used detector was R-928 operating at a voltage of 950 V.

**B. Results and discussion**

*1. Synthesis of Zn(cur)O*

The Zn(cur)O particles were prepared through wet chemistry by the precipitation method having zinc nitrate, curcumin, and potassium hydroxide as starting materials. After a specified amount of curcumin was solubilized in 50 mL D.D.W at 85–90$^o$C, zinc nitrate was added and the mixture refluxed for an hour and the yellow colored solution was cooled to 0$^o$C in an ice bath and subsequently potassium hydroxide solution was added slowly. The yellowish precipitate obtained, Zn(cur)O, was centrifuged and washed. It should be noted that curcumin degrades in alkaline medium, but addition of potassium hydroxide to curcumin and zinc nitrate did not show any degradation or color change of curucmin. Zn(0.5cur)O, Zn(1.0cur)O, Zn(1.5cur)O, Zn(2.0cur)O particles were synthesized respectively by using 0.5 mg, 1.0 mg, or 2.0 mg of curcumin. Two controls ZnO and cur@ZnO (anchoring of curcumin on ZnO surface) were prepared. In case of cur@ZnO, washing with acetone could easily remove curcumin (yellowish curcumin appearing in the wash solution) during centrifugation and yellowish color faded with each washing. On the other hand washing of Zn(cur)O with acetone didn't alter its yellowish color and no curcumin was detected in the wash solution. Curcumin-anchored ZnO (cur@ZnO) is prepared by the physical method which means mixing of polymers/organic molecule with the nanoparticles or nanostructures in solutions to which are said to be connected physically, i.e., via static interactions, van der Waals forces or Lewis acid–base interactions. On the other hand, there is the chemical method where bonding of polymers or organic ligands with the nanoparticles via chemical bonds takes place. The products of this method are more stable because of stronger interactions. Besides the consistency of the yellow color observed for curcumin

conjugated ZnO (Zn(cur)O) after several washes, reflecting the strong interaction between curcumin and ZnO, the compound also satisfies features this method implies upon the products such as, perseverance after solvent washing, i.e., the products can be isolated from the reaction system by non-solvent methods[116] or centrifugation–redispersion treatment[117]; there is no significant phase separation under TEM or AFM observation; and IR spectra show the signals of chemical bonds as will be seen later on.

## 2. Characterization

a. X-ray Diffraction Analysis

The XRD pattern of Zn(cur)O is shown in Fig. 2.3a. All the Zn-O hexagonal phase diffraction peaks were found at 2θ of 31.80$^o$ (100), 34.51$^o$ (002), 36.26$^o$ (101), 47.49$^o$ (102), 56.61$^o$ (110), 62.99$^o$ (103), 66.55$^o$ (200), 67.84$^o$ (112), 69.19$^o$ (201) and 77.53$^o$ (202). These observed peaks are in good agreement with those for hexagonal ZnO with wurtzite structure as reported earlier[118]. The additional peaks found at 37.03$^o$, 37.80$^o$, 43.23$^o$ and, 64.35$^o$ were attributed to curcumin. The sharp diffraction peaks apparent in the figures indicate good crystallinity of the ZnO nanoparticles. No characteristic peaks of any other phase of ZnO or of any impurity were observed which indicates the relatively good purity of the compounds. The pattern of pure curcumin shows sharp characteristic peaks of curcumin[119] at 2θ of 20$^o$-30$^o$. However, the characteristic peaks of curcumin were not observed when coated on ZnO in the XRD patterns of (0.5 and 1.0), and only three peaks at 26.0, 26.8, and 29.45 for 2 mg were attributed to curcumin in this range. The reasons for the absence of curcumin peaks could be due to that: (1) the amount of curcumin was too small to be detectable in XRD,

and (2) curcumin had lost its crystallinity after dissolving it with ZnO. Furthermore, it is noticed that the addition of the small amounts of curcumin didn't change profoundly the crystallinity of ZnO, however, the addition of 2 mg curcumin effected the crystallinity of ZnO where some peak seemed to disappear.

The Scherrer equation[120] relates average crystallite size of the sample with the line broadening at full width at half maximum (FWHM) and thus the average crystallite sizes of samples were determined using the Scherrer equation:

$$d_{XRD} = \frac{0.9\,\lambda \times \beta}{\cos\theta} \quad (2.1)$$

where $D_{XRD}$ is the average crystallite sizes (nm), $\lambda$ the X-ray wavelength ($\lambda = 1.5406$ Å), $\beta$ the full-width at half-maximum (FWHM) of the highest intensity peak in radians, and $\theta$ the half of diffraction peak angle. The peak of the 110 plane (strongest peak) was monitored to evaluate relative crystallite size with respect to curcumin concentration used during synthesis of Zn(cur)O. Crystallite sizes of 24.63 nm, 20.18 nm, 26.06 nm, and 20.04 nm were obtained for ZnO, Zn(0.5cur)O, Zn(1.0cur)O, and Zn(2.0 cur)O respectively. As the curcumin increased from 0.0013 mmol (0.5 mg) to 0.0027 mmol (1 mg) the crystalline size increased (a decrease in FWHM) but further increase to 0.004 mmol curcumin (2 mg) decreased the crystalline size.
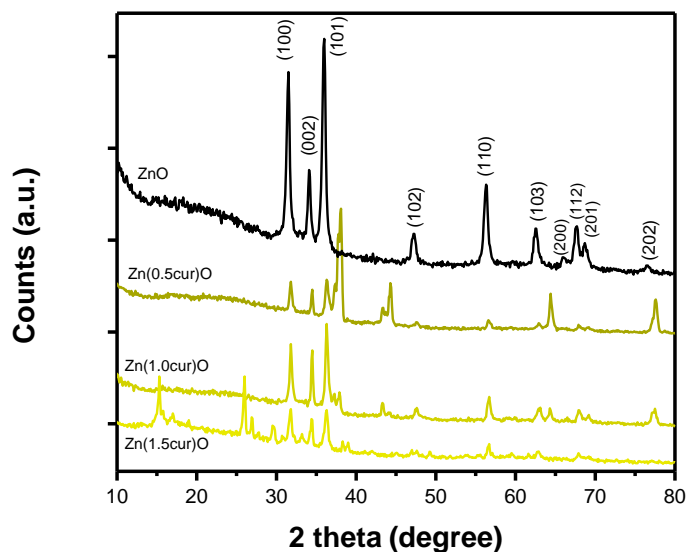
**Figure 2.3: (a) X-ray diffraction patterns of Zn(cur)O nanoparticles as prepared using 0.5 mg, 1.0 mg or 2.0 mg of curcumin.**

b. Zeta Potential

The apparent zeta potential gives supp related to surface charge. The measurements were done in double distilled water where the pH is 6.8 - 7.0. As depicted in Fig. 2.4 the zeta potential measurement of curucmin in water showed a value close to –40 mV whereas that of ZnO was found to be nearly 0 mV in water. When curcumin was mixed with zinc nitrate, a zeta potential value slightly negative but close to zero was observed. This observation is not surprising as $Zn^{2+}$ can form a complex with curcumin by helping to neutralize the negative surface charge of curcumin solution. Now for Zn(cur)O, the zeta potential remarkably changed to +40 mV confirming that Zn(cur)O has a positive surface charge and is relatively stable reflecting the strong interaction between curcumin and ZnO.
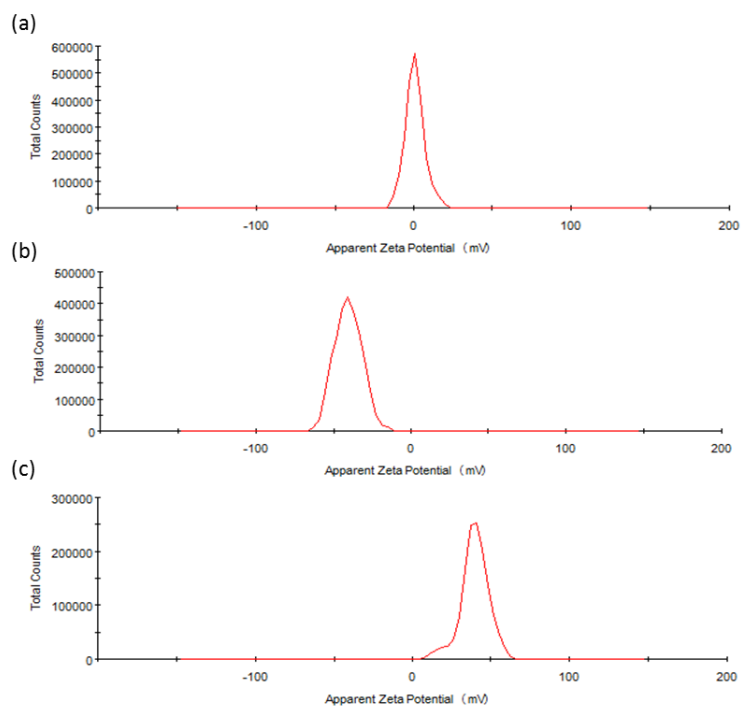
**Figure 2.4: Apparent Zeta Potential distribution of (a) ZnO, (b) Curcumin and (c) Zn(cur)O.**

c. TG-DSC analysis

The TG–DSC curves of the precipitates Zn(cur)O, ZnO, cur@ZnO and raw curcumin are shown in Fig. 2.5. The TG curve indicates that a remarkable mass loss (~23%) occurred during the thermal decomposition of Zn(cur)O and a range of 3-4 % mass loss for ZnO and cur@ZnO. The precipitate Zn(cur)O began to decompose when the temperature was above 180 $^{\circ}$C, and  the decomposition was complete at ~240 $^{\circ}$C. The weight-loss in raw curcumin occurs around 260°C till around 550 °C, whereas the weight loss for ZnO occurred in the range 220 – 280 °C (Fig. 2.5b). The derivative of differential scanning calorimetry (DSC) showed a minimum at around 250 °C for ZnO. For raw curcumin the minima was found to be at around 180 °C and for Zn(cur)O at around 230 °C.  The maxima at 160°C for raw curcumin could be detected in Zn(cur)O in addition to maxima at around 200 °C due to the main weight loss of Zn(cur)O, but one of the major maximum at around 540 °C in raw curucmin was not found in

20

Zn(cur)O. The small maximum found at around 105 °C in Zn(cur)O is similar to one obtained in ZnO. However, cur@ZnO showed similar TGA and DSC data like obtained for ZnO as shown in Figure 2.5b. Interestingly, weight loss in curcumin and cur@ZnO follows a gradual decrease whereas in ZnO and Zn(cur)O the weight loss occurred more rapidly. This, along with the shift in peaks in thermogram of Zn(cur)O compared to ZnO clearly indicates that Zn(cur)O is different from ZnO anchored with curcumin (cur@ZnO) or ZnO.
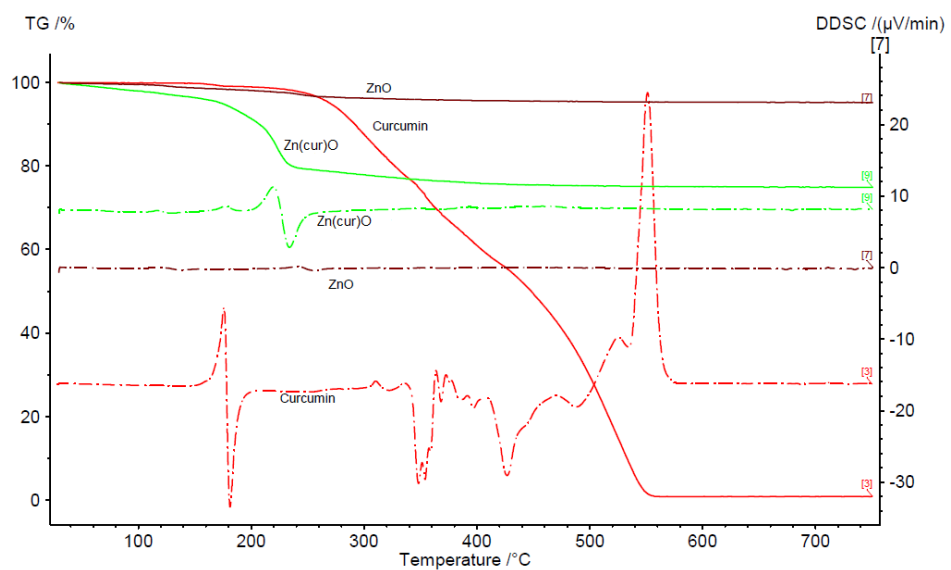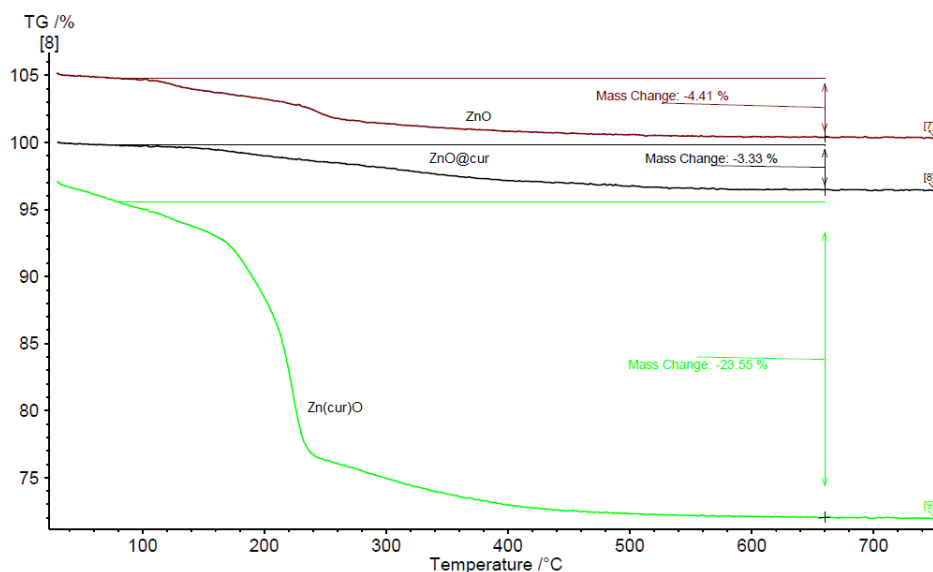
**Figure 2.5: (a) TG analysis of Zn(cur)O and compared with ZnO alone, (b) Derivative of DSC**

d. SEM

The SEM images of the as-synthesized ZnO, cur@ZnO and Zn(cur)O particles are presented in Figure 2.6. The particles were of sizes ranging from 200 – 600 nm width and 600 – 2000 nm length. There were also particles of smaller sizes. The particles looked similar to grain or half grain. Zn(cur)O particles (Figure 2.6 c & d) were found to be not different in their appearance and morphology compared to ZnO(Figure 2.6b) and cur@ZnO (Figure 2.6c). Closer SEM images of these grain shapes Zn(cur)O were recorded in 200 nm resolution as shown in Fig. 2.7 showed that these grain appearing particles were assembled of nano-sized particles. It should be noted that changing the concentration of curcumin (0.5 mg, 1.0 mg, 1.5 mg or 2.0 mg) during preparation of Zn(cur)O did not have any foremost impact on the morphology of these particles, although Zn(cur)O prepared using 2 mg curcumin were found to have more number of smaller or half-broken particles (Figure 2.7c). The morphology of these particles was also clearly visible in fluorescence STED microscope (Figure 2.7d). The

22

fluorescence coming out from the whole region indicates curcumin is present all over the particle.
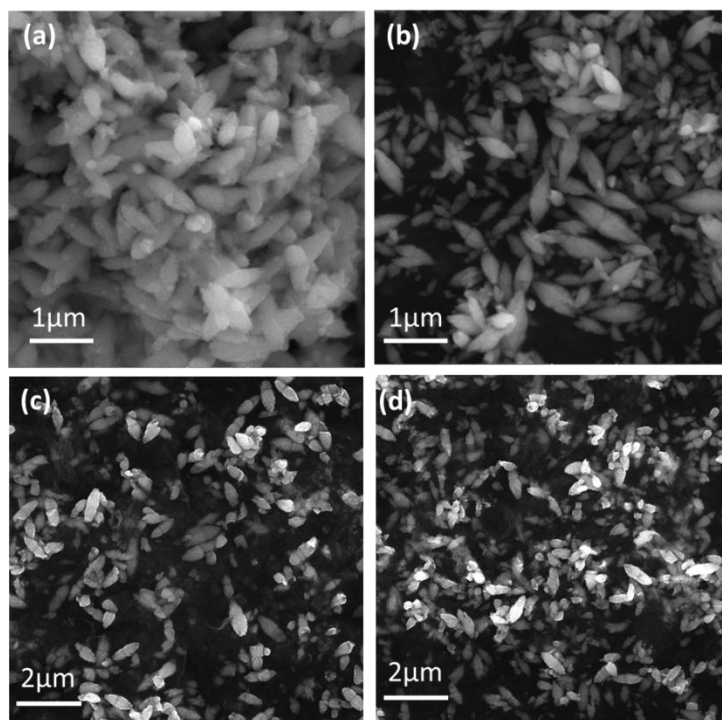


**Figure 2.6: SEM images of (a) ZnO, (b) ZnO anchored with curcumin (cur@ZnO), (c) Zn(0.5cur)O and (d) Zn(1.0cur)O**
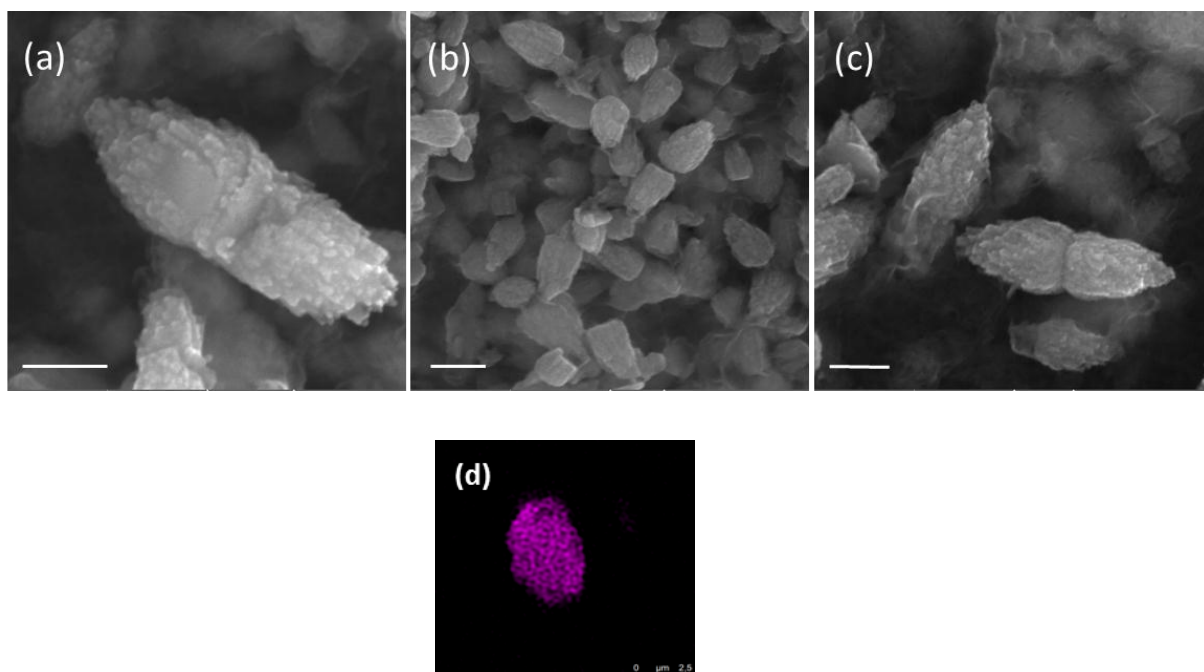
**Figure 2.7: SEM images of Zn(cur)O using (a) 0.5 mg, (b) 1.0 mg and (c) 1.5 mg of curcumin. (d) STED image of Zn(cur)O particles. The scale bar for SEM images is 200 nm.**

e. FTIR spectroscopy

FT-IR spectroscopy was done to inspect the interaction of curcumin with ZnO through the fingerprint vibrations of both curcumin and ZnO and of Zn(cur)O as shown in Fig. 2.8. Bare ZnO has a characteristic strong and broad absorption peak around 442 $cm^{-1}$ assigned to Zn–O bond[121]. No bands appear around 3500 $cm^{-1}$ nor 1600 $cm^{-1}$ which are usually attributed to O–H stretching vibration peak of the hydroxyl functional group and to the bending vibration of the surface H–OH which means that no hydroxyl groups adsorption on the surface of ZnO takes place and what we have is ZnO rather than $Zn(OH)_2$ . The peak at 442 $cm^{-1}$ in ZnO is shifted to 484 $cm^{-1}$ in Zn(cur)O and is less pronounced  suggesting the presence of an altered Zn-O bond due to its interaction with curcumin. The frequency region of both phenolic v(OH) vibrations of the curcumin was computed to be at 3595 $cm^{-1}$,  but was shifted to lower frequency at

3510 cm$^{-1}$ due to intramolecular and intermolecular H-bonding in curcumin[122]. In Zn(cur)O the location of the band is screened by the broad band at 3430 cm$^{-1}$ attributed to the water hydroxyls groups adsorbed at the surface off the compound.

Curcumin molecule has one of the most prominent functional group—the β-diketone group—at the center which has high driving force to form chelation with metal ions. The β diketo system in curcumin was found to form charge transfer complexes with TiO$_2$ nanoparticles[23]. This could be due to the co-existence of keto and enol groups in curcumin molecules. In this respect, it is not surprising to have an interaction—be it weak or strong—of this β-diketone moiety with Zn$^{2+}$ at the bulk surface. However, for the case of curcumin-ZnO nanostructures, its corresponding FTIR dismisses such an interaction. In fact, the curcumin spectra doesn't show any peak in the carbonyl region (1800–1650 cm$^{-1}$) as reported earlier neither in the solid state nor in solutions indicating that curcumin exists mainly in the enol form. However, two peaks show in this region at ~1650 cm$^{-1}$ and at 1756 cm$^{-1}$ for the ZnO-curcumin compound, where the 1650 cm$^{-1}$ peak could be due to $\nu$(C=O) of curcumin. The other peak at 1756 cm$^{-1}$ could be related to the carbonyl's asymmetric mode of vibration in its diketo solid form (the symmetric mode is unseen usually because its intensity is too low).

The weak experimental bands observed in the IR spectrum (3079–3000 cm$^{-1}$) are assigned to the aromatic C-H stretches while the lower frequency bands are attributed to the methyl group motions[122]. Theoretical calculations show that the enolic $\nu$(OH) mode is at 2979 cm$^{-1}$ [122]. Experimentally, this band usually appears weak and broad as it did in this case. The absence of a clearly defined $\nu$(OH) band has been previously discussed by Tayyari et al.[123]: "the intensity and broadness of the enol band is dependent on the strength of the intramolecular hydrogen bond where it would decrease

in intensity and increase in broadness as the strength of the hydrogen bond increases".

Also in their work on dibenzoylmethane (DBM), a β-diketone system, similar to curcumin, they suggested that the π-systems, such as the phenyl groups increase the H-bond strength through conjugation with the enol ring. The hydroxyl and methoxy groups on the phenyl rings of curcumin are electron donating systems expected to even cause stronger hydrogen bond effect. So any weakening of these groups' electronegativity (phenyl ring and/or the existing methoxy and hydroxy groups on it) by forming bonds or conjugating with other moieties would cause the hydrogen bond strength to decrease thus allowing the enol peak to appear more clearly. This is what we observe in the Zn(cur)O sample, where the enol band appears sharper and more intensified, suggesting the hydrogen bond strength in the anchored curcumin decreases due to probably the involvement of the ZnO with the hydroxyl or methoxy groups on the phenyl ring. The carbonyl and hydroxyl groups of curcumin can bind to the surface of ZnO particles, making way for electron transfer from the excited curcumin molecule to the conduction band of ZnO.  This could be supported also by the disappearance and shifting of the bands at 960 and 855 cm$^{-1}$ in Zn(cur)O  which are attributed to $\nu$(C-O) vibrations. It worth noting that the peaks in the range 2830-3000 cm$^{-1}$ could also be attributed to C-H stretches interfering with the enolic $\nu$(OH).

The peak in curcumin at ~1630 cm$^{-1}$ has a predominantly mixed $\nu$(C=C) and $\nu$(C=O) character. The very low intensity peaks in the region 2700 – 3000 cm$^{-1}$ is due to aliphatic C-H stretches in curcumin. The most prominent band in the curcumin spectrum was found at 1510 cm$^{-1}$ attributed to highly mixed vibrations of $\nu$(C=O), d (CC=O), and d (CCC)[122]. The IR bands in frequency region 1430–1460 cm$^{-1}$ are due to deformation vibrations of the two methyl groups. Based on earlier work[122], most

bands in frequency region 1450–1300 cm$^{-1}$ are highly mixed. The bands at 1290 and 1282 cm$^{-1}$ belong to the pure in-plane COH vibrations of aromatic rings. The bands in 1277–1188 cm$^{-1}$ are attributed to the in-plane deformation vibration of phenyl rings and skeletal in-plane deformations. The band at 886 cm$^{-1}$, belonging to the COH out-of-plane vibration of aromatic rings, could be described as pure vibrations. The IR bands at 864 and 856 cm$^{-1}$ are assigned to the highly mixed □ COH and □□CCH (Ph). Generally, the bands between 870 cm$^{-1}$ and 710 cm$^{-1}$ could be attributed to different COH out-of-plane aromatic and skeletal motions.
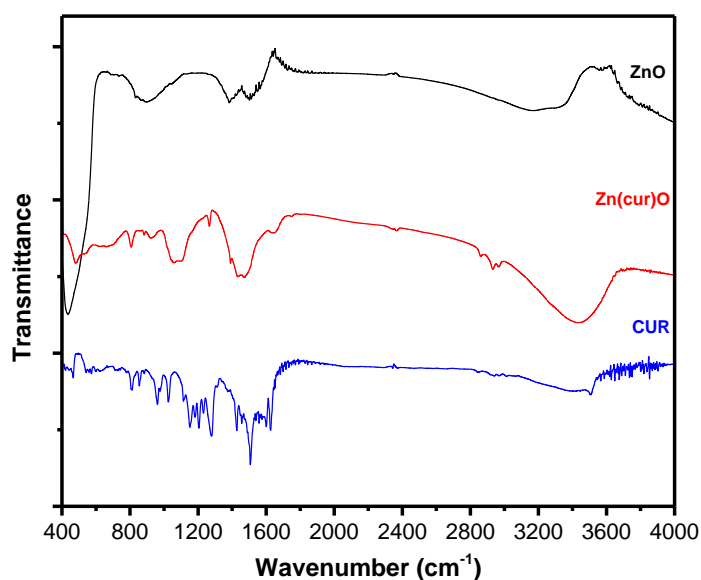


**Figure 2.8: FT-IR spectra of as-synthesized ZnO, curcumin, and Zn(cur)O nanostructures at room temperature.**

f. UV−Vis diffused reflectance spectroscopy (DRS)

UV−Vis diffused reflectance spectra of the Zn(cur)O, ZnO and cur@ZnO are depicted in Fig. 2.9. All of them show a similar broad and strong absorption spectrum with an onset at 400 nm and a maximum at about 343 nm, which is characteristic of ZnO wide-band semiconductor. Another strong absorption maximum was found at

around 445 nm with an absorption onset at ~570 nm for Zn(cur)O confirming the presence of curcumin. For cur@ZnO, the absorption peak intensity was less and the onset had a broader tail. The position of the curcumin peak is red shifted compared to curucmin in solution. This shift in absorption spectra could be due to the interaction of curucmin with zinc.
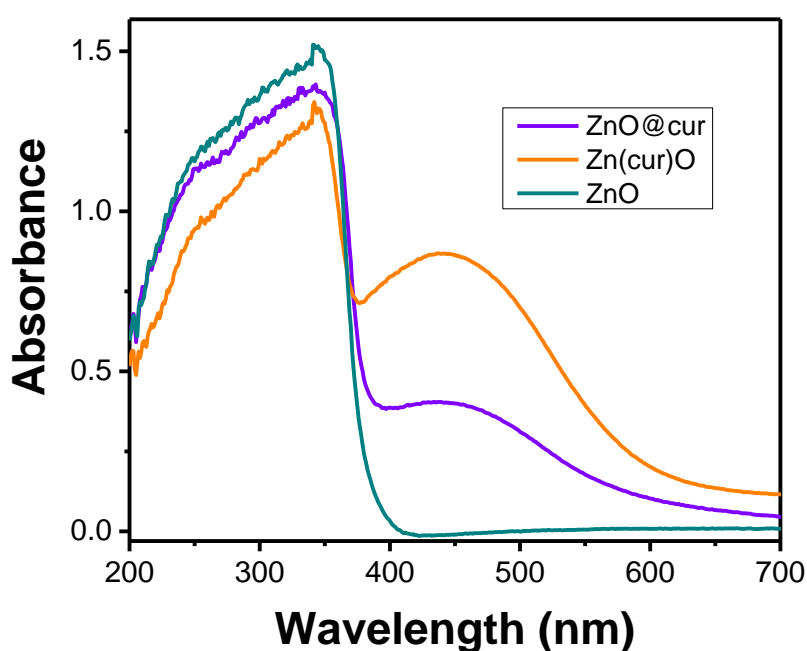


**Figure 2.9: UV–visible diffuse reflectance spectra of the as-synthesized ZnO, Zn(cur)O and cur@ZnO nanostructures at room temperature.**

g. Photoluminescence study

Usually the photoluminescence (PL) of ZnO nanoparticles has two main components[124]: "the typical exciton emission or near-band-edge emission, i.e., photo-generated electron recombination with holes in the valence band or in traps near the valence band". This process produces UV light of about 370 nm because the ZnO band gap is 3.37 eV at room temperature. The other component is visible emission (Green

emission, also called deep-level emission) related with oxygen vacancies and zinc interstitials, but its corresponding mechanism is controversial and not clear so far[124]. Room-temperature PL spectra of ZnO can exhibit a number of different peaks in the visible spectral region, which have been attributed as mentioned earlier to the defect emission. Emission lines are reported at 405, 420, 446, 466, 485, 510, 544, 583, and 640 nm[125].

Two popular mechanisms for the ZnO visible emission have been suggested (Scheme 1): one is recombination of a shallowly trapped electron with a hole in a deep trap[126-127] and the other is recombination of an electron in singly occupied oxygen vacancies (i.e., deeply trapped) with a photo-generated hole in the valence band[128-129]. Since it is difficult to determine the exact location and the energy level of the deep traps, scientists weren't able to decide on one mechanism and both are still coexistent. Nonetheless, both models agree that ZnO visible emission intensity depends on its defect concentration. Also, there is some convincing evidence that the type of defect responsible for the green emission is located at the surface. It was shown that coating ZnO nanostructures with a surfactant suppressed green emission[125]. Another factor could be the possible presence of $Zn(OH)_2$ at the surface, especially for nanostructures prepared by solution methods, which could affect the emission spectra from ZnO nanostructures[130].

The ZnO luminescent properties are influenced by the preparation method and they are essentially associated to electronic and crystalline structures. Therefore, preparation methods such as pyrolysis, chemical vapor deposition and molecular beam epitaxial growth at high temperature, are common methods to produce highly crystallized and purified ZnO nanocrystals[8] with fine UV emission. On the other

hand, sol–gel techniques and sonochemical synthesis at room temperature are the

methods usually used to obtain ZnO with highly visible emission as the resulting

samples usually-still small enough- contain a lot of defects as they lose

crystallinity[131-132].
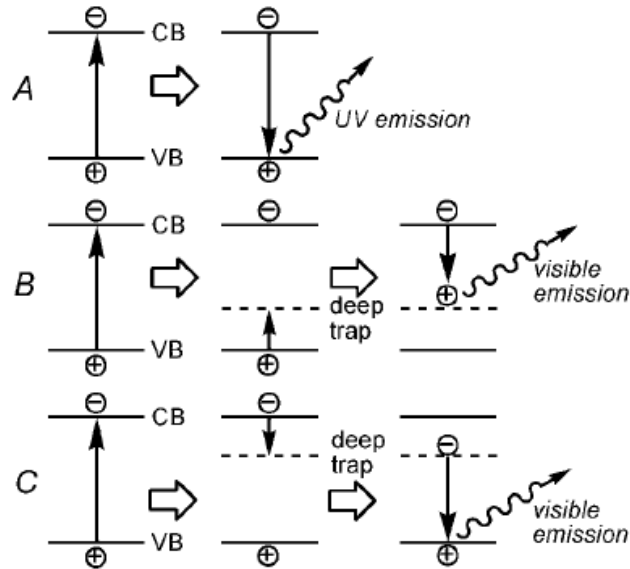


**Scheme 2.1: Photoluminescent processes suggested for ZnO nanoparticles. (A) Typical exciton emission, (B) recombination of a shallowly trapped electron with a deeply trapped hole, and (C) recombination of a shallowly trapped hole with a deeply trapped electron. In order to simplify the maps, the shallow traps near the valence band (VB) and the conductance band (CB) are not marked here.[124]**

The photoluminescence of Zn(2.0cur)O, ZnO, and cur@ZnO were measured at

three excitation wavelengths: 320 nm, 375 nm, and 425 nm (Fig. 2.10) in water. At 320

nm excitation wavelength, ZnO shows two emission bands, one in the UV range at

around 358 nm, which is associated with exciton emission, another in the visible range

at around 560 nm, which originates from electron – hole recombination at the deep level

caused by oxygen vacancy or zinc interstitial defects[124].  This result – the observation

of a visible PL in water - by itself is unconventional and interesting given the fact that

even small amounts of water would kill ZnO PL- namely visible fluorescence- as hydroxyl groups coordinate on the surface of ZnO NPs.

For the curcumin anchored on the surface of ZnO sample (cur@ZnO), the UV range emission band enhanced by ~6 folds, and the photoluminescence in the visible region was substantially quenched. Curcumin usually shows fluorescence in this region (around 530 nm), however its contribution in both Zn(cur)O and cur@ZnO was minimum or negligible. Similar quenching behavior has been observed and reported for capped ZnO compared with the uncapped ZnO[124]. Interestingly, and in comparison to ZnO, the UV emission of Zn(cur)O at 358 nm increased by ~4 fold (lower than that of cur@ZnO) and the visible photoluminescence reduced by ~ 10 folds. This trend has been related earlier to increased crystallinity and decreased surface defects[133]. Some polymer and/or organic ligands are thought to fill up (passivate) the defects on ZnO surface, which act as visible luminescence centers, resulting in quenching the ZnO visible emission and improving the UV emission[124]. This is what we think curcumin is doing. It is important to point out that the visible emission from ZnO cannot be fully explained by a single type of defect[134].

The highest enhancement of UV exciton emission is for cur@ZnO due to physical adsorption as observed previously for PVP[135]. The visible emission band of Zn(cur)O was found to be 10 nm red shifted compared to that of ZnO. Both Zn(cur)O and cur@ZnO gave an additional band at around 405 nm that was absent in ZnO. The emission line at 405 nm could be also related to defect emission caused by curcumin because we don't see any such peak in ZnO. Changing the excitation wavelength to 375 nm did not change the visible emission pattern of Zn(cur)O, cur@ZnO and ZnO; it was similar to the photoluminescence spectra observed at 320 nm excitation wavelength.

However, a line emission at 425 nm was observed for all three that could also be attributed to defect emission as this position (at around 420 nm) is reported in literature too[125]. The highest intensity was observed for ZnO then Zn(cur)O and cur@ZnO, this trend is opposite to what is observed at 320 nm excitation wavelength. At excitation wavelength of 425 nm, ZnO is not expected to have a good photoluminescence behavior due to poor light absorption (absorbance) in contrast to curcumin which has a strong light absorption (absorbance) at this wavelength and a well-known response in this region. Thus, the contribution of fluorescence of curcumin relative to ZnO is substantial at this excitation wavelength and the emission is largely due to curcumin rather than ZnO, seen in water at ~530 nm[136]. The peak at 495 nm could be scattering.

To examine the effect of solvent on the photoluminescence properties of Zn(cur)O, measurements were done in ethanol and water as depicted in Fig. 2.11. The PL spectra of Zn(cur)O showed sensitivity to the solvent environment where the emission wavelengths at ~358 nm blue shifted to 352 nm while going from a more polar (water) environment to a relatively less polar (ethanol) one at excitation wavelength 320 nm. Also, the broad peak around 405 nm in water became less broadened and blue-shifted to 398 nm in ethanol. The emission at 530 nm appearing in ethanol is attributed to curcumin's fluorescence and it should not be mistaken by the ~560 nm green emission observed in water (appearing very weak in fig. 2.11a, see inset for better visualization) attributed earlier to defects. Such effects due to solvent are expected for luminescent materials. Similarly, at excitation 425 nm which supposedly excites only curcumin, the photoluminescence intensity at 530 nm increased much more appreciably, > 10 fold, than in water. The emission line found in water around 495 nm is not detected

in ethanol. Thus, the increase in photoluminescence intensity is largely attributed to the fluorescence enhancement of curucmin rather than photoluminescence of ZnO as curcumin has a higher fluorescence quantum yield in ethanol compared to water[137].
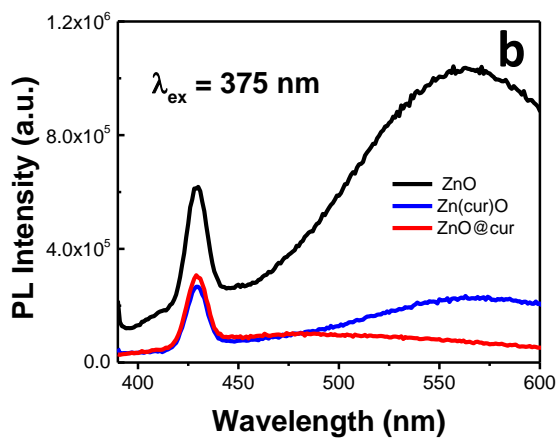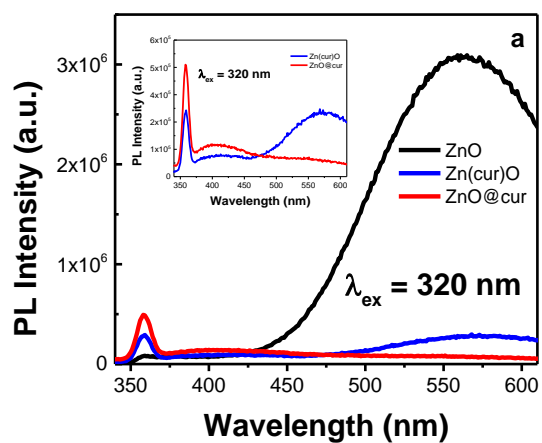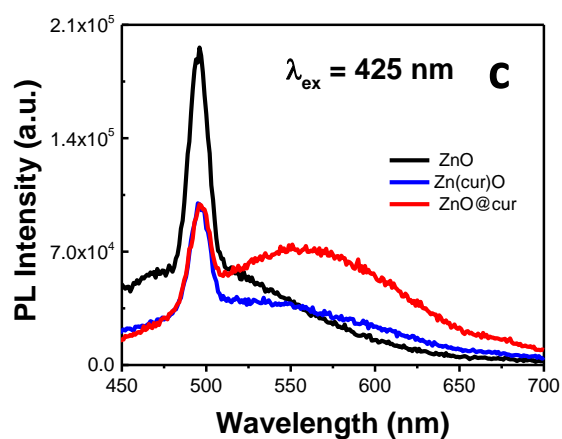
**Figure 2.10: Photoluminescence spectra of Zn(cur)O, cur@ZnO and ZnO in water at room temperature at excitation wavelengths (a) 320 nm (b) 375 nm (c) 425 nm.**
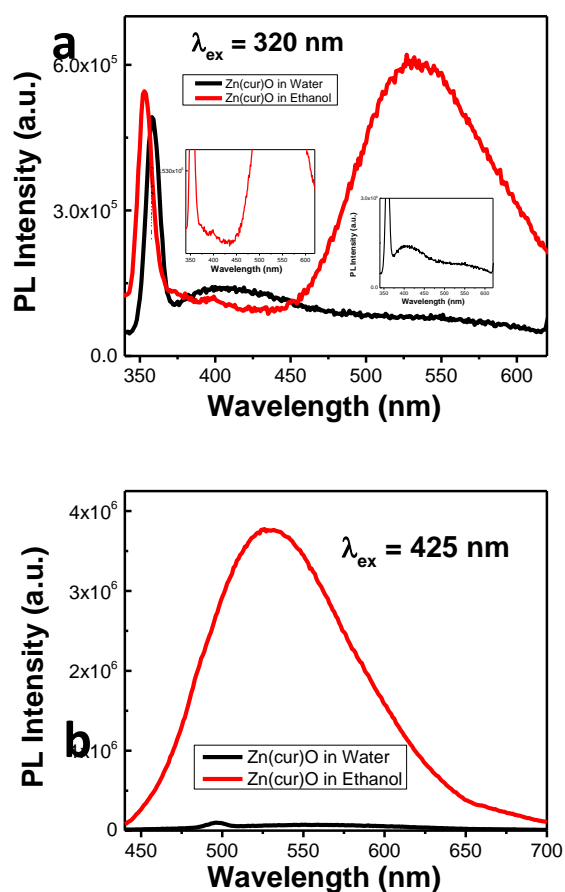


**Figure 2.11: Effect of solvent on photoluminescence spectra of Zn(cur)O at excitation wavelengths (a) 320 nm (b) 425 nm**

i.    Effect of changing curcumin content on curcumin-ZnO PL

The measurement of PL of Zn(xcur)O with different curcumin content in ethanol were recorded as shown in Fig. 2.12. At excitation wavelength 320 nm, the broad peak around 555 nm in PL spectra of Zn(0.5cur)O and the very weak peak around 400 nm in Zn(2.0cur)O blue shifted to ~530 nm and ~380 nm  respectively, whereas peak at 353 nm maintained its position with curcumin change.  The UV and visible emission show similar trends where all peaks showed decreased PL intensity as the curucmin increased. It appears that curcumin, besides lowering the number of defects, might also be separating charges where the electron-hole recombination is prolonged leading to loss of the exciton UV emission. In the case of Zn(2.0cur)O, the blue emission was almost completely quenched confirming what we previously suggested of having curcumin introducing this type of defect.

For an excitation wavelength at 375 nm, PL showed two peaks at ~ 421 nm and 527 nm showing opposite trends in intensity. The 527 nm peak of Zn(0.5cur)O had the lowest intensity and the other Zn(cur)O samples had comparable intensities. On the contrary, the 421 nm peak for Zn(0.5cur)O had a slightly higher intensity over the other samples of comparable intensities. The PL at 425 nm excitation showed a similar behavior as expected for curcumin band as seen in the preceding PL.
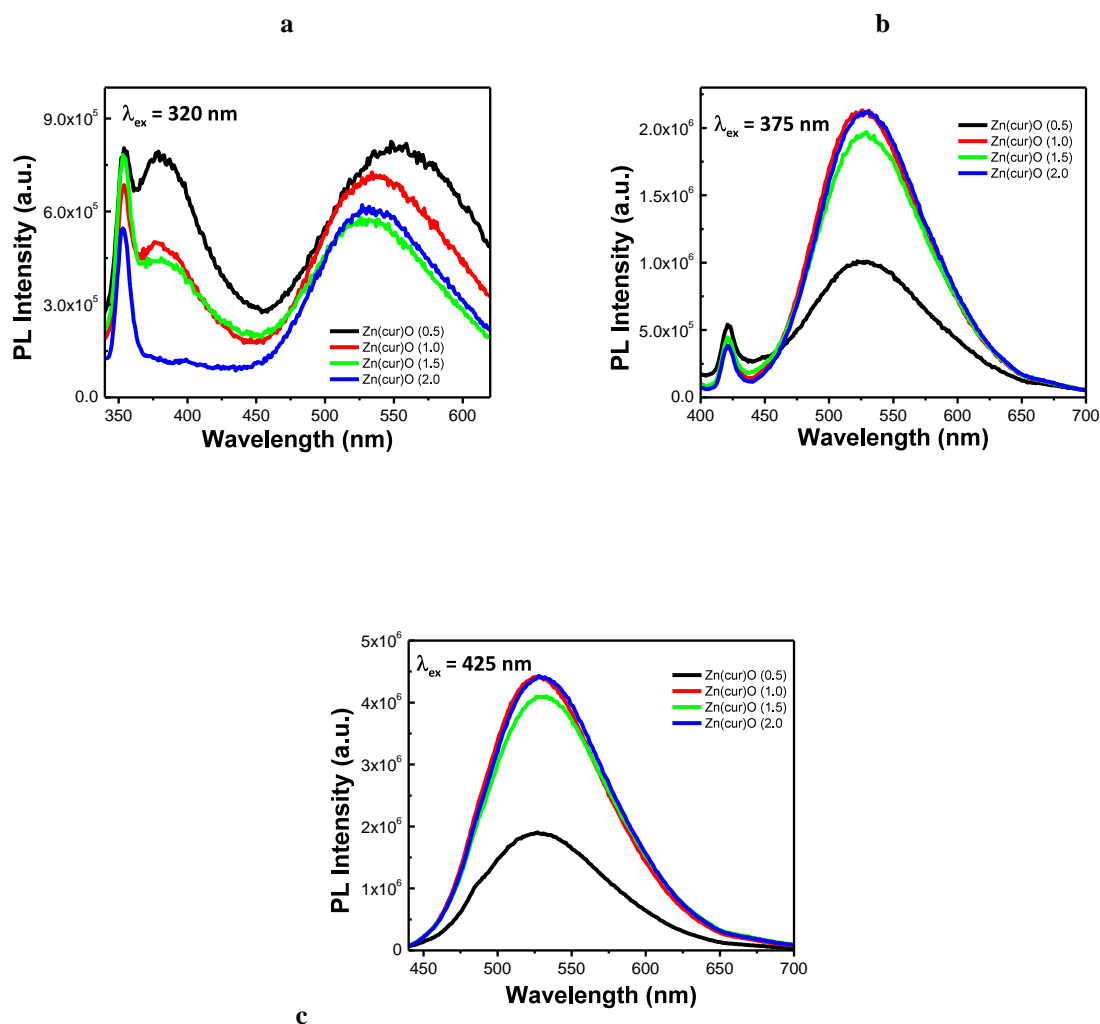
**Figure 2.12: Photoluminescence spectra of Zn(x.cur)O, in ethanol at room temperature at excitation wavelengths (a) 320 nm (b) 375 nm (c) 425 nm.**

i.      Solid State Photoluminescence

The solid state photoluminescence of powder Zn(x.cur)O was taken at different excitation wavelengths as given in Figure 2.13. The solid state PL is different from PL in solution and this is expected as the solvent environment directly or indirectly influences PL spectra in solution due to defects, whereas self-quenching of materials may shift the position of the spectrum and/or quench PL intensity in the solid state. The visible PL at 575 nm for the excitation wavelength at 320 nm decreased in comparison

to ZnO as the curcumin content was increased from 0.5 mg to 1.0 mg and 2.0 mg. The red shift of ZnO and Zn(cur)O visible PL compared to solution PL (water or ethanol) is expected because in the solid state the energy transfer or self-quenching is unavoidable. Two additional peaks at 400 nm and 423 nm were also found for ZnO, which decreased with the increase in curcumin content. For an excitation wavelength at 375 nm, it's noticed that the 575 PL peak didn't decrease substantially as before and the Zn(1.0cur)O and Zn(1.5cur)O peaks were almost similar in intensities, decreasing up to ~47% of the curcumin free ZnO intensity, except that Zn(1.5cur)O had a red shift by 10 nm. At 425 nm excitation wavelength, a very weak peak at 475 nm was observed for ZnO. As for the Zn(cur)O, the PL looks similar to what is observed at excitation 375 nm.

a                                                              b

c
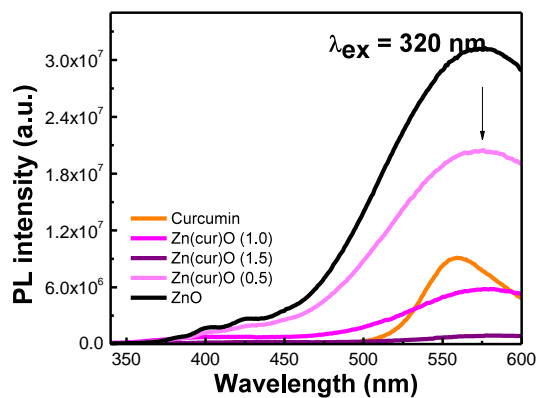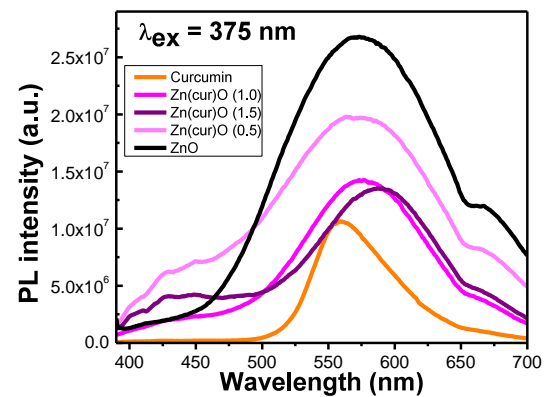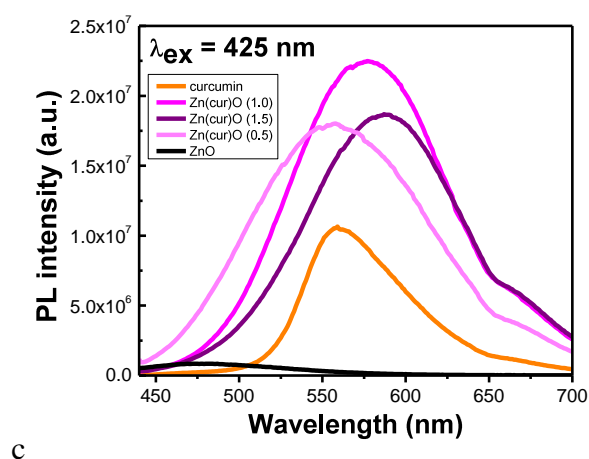
**Figure 2.13: Solid state Photoluminescence spectra at room temperature of ZnO and Zn(xcur)O at excitation wavelengths (a) 320 nm (b) 375 nm (c) 425 nm.**

## C. Conclusion

Curcumin conjugated ZnO nanostructures assembling into sub-micro grain-like structures were synthesized hydrothermally. The nanostructures synthesized possess the wurtzite hexagonal crystal structure of ZnO and show very good crystalline quality. FTIR spectra showed that the conjugation of curcumin to ZnO surface might be through the methoxy and/or hydroxyl groups present on its phenyl rings. The incorporation of curcumin into ZnO resulted in the enhancement of the exciton emission at 358 nm and the substantial decrease of the visible emission around 560 in comparison to ZnO PL. The compound's PL depended on the curcumin's concentration where increased curcumin content was accompanied by a decrease in the intensities of visible and UV emissions. Curcumin seemed to fill defects that were visible luminescence centers and at the same time prolonged e-h recombination resulting in lowering UV emission intensity. Solid state PL also showed –at different excitation wavelengths- that increased curcumin concentrations suppressed visible emission. The bare ZnO -prepared through the same method- showed, unexpectedly, visible PL in water. This could have

38

important applications in biological systems since the hindrance was always the loss of

PL in water.

# CHAPTER III
# APPLICATION OF CURCUMIN CONJUGATED ZnO FOR ENVIRONMENTAL APPLICATIONS

**A. Removal and Fluorescence Sensing of Arsenic**

*1. Introduction*

Arsenic contamination in natural water renders the lives of millions of people around the world at risk. Exposure to arsenic over extended periods of time leads to serious health problems, such as cancers of liver, lung, kidney, bladder, and skin[138-139] cardio vascular system problem[140], and affects the mental development of children[141]. Arsenic in natural water can be the result of leaching from arsenic containing source rocks and sediments. Its presence is generally associated to geochemical environments such as basin-fill deposits of alluvial lacustrine origin, volcanic deposits, inputs from geothermal sources, mining wastes and landfills[142-143]. In 2001, the US Environmental Protection Agency (USEPA) lowered the maximum contaminant level (MCL) for arsenic in drinking water from 50 to 10 μg/L (0.01 ppm)[144] which rendered the drinking sources all over the world unacceptable. The arsenic contamination of the groundwater of West Bengal in India is classified an environmental disaster. Other countries as Bangladesh, New Zealand, USA, Pakistan, Taiwan, Japan, etc., also have this problem. Therefore, research on arsenic removal from drinking water using low-cost and simple methods has greatly increased.

Arsenic exists in water as two major inorganic arsenic species, namely As(III) (arsenite, $AsO_3^{3-}$) and As(V) (arsenate, $AsO_4^{3-}$). The existence and ratio of these two forms of arsenic is dependent greatly on pH and the redox conditions of the environment in which they are present. Arsenates are stable under aerobic or oxidizing

conditions, while arsenites are stable under anaerobic or mildly reducing conditions[144]. Arsenite species exists in solution as $H_3AsO_3$ (arsenous acid) and $H_2AsO_3^-$ (dihydrogen arsenite) with $pK_a$ values of 9.2 & 12.7 respectively, and also includes $H_4AsO_4^-$. Arsenate species is present as $H_2AsO_4^-$ (dihydrogen arsenate) and $HAsO_4^{2-}$ (arsenate hydrogen ion) and the $pK_a$ values for arsenic acid ($H_3AsO_4$) are $pK_{a1}=$ 2.3, $pK_{a2}=6.8$, and $pK_{a3}=11.6$[145]. Of these two redox states of As, arsenite As(III) is the more toxic form than arsenate. Also, arsenate is easier to remove from water than arsenite, as it is an ionic species in the pH range typically found in the aquatic environment[146]. Arsenite, on the other hand, exists in nonionic form $H_3AsO_3$ in natural water with pH value ranging from weakly acidic to weakly alkaline, which renders the adsorption performance of various adsorbents on As(III) poor[147-149]. It would require additional oxidizers to oxidize arsenite to arsenate if pH is less than 10[146].Thus, oxidizing As(III) to As(V) and/or pH adjustment becomes necessary for its effective removal from water before coagulation–precipitation or adsorption processes[150-152]. As this would add to the complexity and cost of the treatment process, adsorbents able to effectively remove As(III) without the oxidation/pH adjustment is being developed.

The conventional methods[144] for arsenic treatment include coagulation and flocculation, precipitation, adsorption, ion exchange, and membrane filtration. Alternative unconventional methods like ozone oxidation, bioremediation and electro-chemical treatments are also used in the removal of arsenic. Among the various arsenic removal techniques, adsorption seems to be the simplest, cost-effective, and safer to handle process than precipitation, ion exchange, and membrane filtration.

Adsorption is a process whereby solids remove substances from either gaseous or liquid solutions. It involves moving a substance from one phase by accumulating it at the surface of another by van der Waals forces and electrostatic forces between adsorbate molecules and the atoms which compose the adsorbent surface[144]. It's a phenomenon observed in most natural physical, biological, and chemical systems. Thus, adsorbents require surface properties such as surface area and polarity and/or functionality. The solids employed in adsorption operations in industrial applications for water and wastewater purification are activated carbon, metal hydrides, and synthetic resins[144]. Other sorbent materials have been also used, including amorphous iron hydroxide[153] and ferric hydroxide[154-156]. Other types of ferric products, such as ferrihydrite[157], silica containing iron (III) oxide[158], iron-oxide impregnated activated carbon[159], Ce(IV)-doped iron oxide[160], iron oxide-coated sand[161], iron(III)-Poly(hydroxamic acid) complex[162], ferric chloride[163], Fe(III)-doped alginate gels[164], nanocomposite adsorbent based on silica and iron(III) oxide[165], and iron oxide-coated polymeric materials[166] are also used in arsenic treatment. It's worth noting that As(V) was found to be easier to adsorb than As(III)[144]. Activated carbon is commonly used as the material in arsenic adsorption treatment [167-169]. The iron oxide impregnated activated carbon has shown higher As(III) and As(V) removal compared with the non-impregnated carbon. But the use of commercial activated carbon is not suitable for developing countries because of its high cost. Iron oxides also have been widely used as sorbents to remove contaminants from wastewater and liquid hazardous wastes. Removal has been attributed to ion exchange, specific adsorption to surface hydroxyl groups or co-precipitation[153]. Most adsorption onto alumina or carbon takes place within 24 h[170].

Arsenic removal technology by adsorption with a commercial granular ferric hydroxide (GFH) has been developed in the early 1990s[155,171]. It can be applied in simple fixed bed reactors, similar to those for activated alumina or activated carbon. Simplified operation is a key benefit of the system, which will operate without the need for chemical pre-treatment or pH correction. Ruhland and Jekel[172] had evaluated three arsenic treatment techniques: direct filtration with $FeCl_3$, adsorptive filtration with $FeSO_4$ and adsorption on granulated ferric hydroxide (GFH) in a full scale water treatment plant. The adsorption on granulated ferric hydroxide is found to be the most preferred process for arsenic removal on the tested conditions providing greater operational reliability with least maintenance and monitoring efforts. Initial laboratory treatment studies with $[As]_{initial} = 9.8$ mg/L and coagulant doses of 500 to 1000 mg/L of $FeCl_3$ with hydrated lime resulted in arsenic removal 98%−99%. As for $[As]_{initial} = 31$ mg/L with dosages of $FeCl_3$ ranging from 200 to 1000 mg/L, 86%−93% arsenic removal were obtained. Multiple dosages of coagulants improved the degree of arsenic removal to 98%.

Also, it had been reported[173] the high and efficient As(III) removal effect by ZnO micro-tubes. These ZnO micro-tubes successfully removed the As(III) contamination completely from natural water samples of Lake Yangzonghai with a relatively low material loading ( 0.06 g/L (60 ppm)). The As(III) concentration in this contaminated lake water sample dropped to ~10 µg/L in 30 min, and further dropped to zero within 4 h.

Herein, we report the removal effect of the sub-micro curcumin linked ZnO structures (Zn(cur)O)synthesized via a simple precipitation process on As(III) with lab-prepared samples near pH ~6. Promising results were obtained as the nanostructures

removed As(III) concentrations found in most arsenic-contaminated natural water bodies with very economical material loading and good capacities. The compound could be used as an effective and economical method for arsenic removal.

## 2. Experimental

The potential application of the ZnO/curcumin system for arsenic removal was tested in comparison with naked ZnO. The same general procedure was followed for different concentrations of arsenic, mainly 100 & 903 ppb, using samples of Zn(cur)O that differ by their curcumin content. Briefly, a stock of 0.2 g/L (200 ppm) Zn(cur)O (and ZnO) solution is prepared by dissolving 1mg of the compound in 5 mL deionized water. A secondary stock of 1 ppm arsenic is prepared from a primary stock Element Reference Solution ($As_2O_3$ As(III) oxide, 1000 ppm, Matrix: 0.5 M $HNO_3$) supplied by Romil LTD and stored in the dark in a refrigerator. The stock solution was diluted to two initial As(III) concentrations (903 and 100 µg/L) as 903 µg/L falls in the high range of arsenic specie concentration found in natural water around the world, and 97.8 µg/L is in the middle to low range[173].

Using 1 ppm As stock solution, 100 ppb and 903 ppb arsenic concentrations were prepared by pipetting 1200 µL and 9500 µL respectively of the stock solution into a final volume of 12 mL. The final concentration of Zn(cur)O (for the different curcumin content and arsenic concentrations) was kept 42-43µg/mL for sake of comparison. The pH of the solution was about 6. During the As(III) removal experiment, and after adding the Zn(cur)O, the arsenic solution was placed on the vortex (speed was no more than 1200 rpm) and left shaking to disperse Zn(cur)O particles and ensure its good contact with the arsenic contamination.

Based on the Linear Dynamic Range indicated in the manual for arsenic measurements of the instrument used (LDR from 6 ppb up to 60 ppb), we set a low and a high standard concentration of 7 ppb and 55 ppb respectively. With proper dilutions, the samples were set to a final maximum arsenic concentration of 50 ppb.

Portions of 1 mL were withdrawn at different time intervals, and dumped directly into a 1 mL deionized water to obtain a final concentration of 50 ppb as a maximum. For the high arsenic concentration (903 ppb), proper dilution was also done. After dilution, the samples were filtered using a general use filter paper. The experiments were done in duplicate or triplicate and each measurement was repeated twice. For each set of measurements done together (7-8 samples), a series of 6 or 8 standards were freshly prepared. No calibration curve with a correlation coefficient $R^2$ less than 0.98 (minimum of 4 points) was accepted.

**Table 3.1. Concentrations and volumes used of As and Zn(cur)O in samples prepared**

| Sample | [As] ppb | V(As) μL | V(H$_2$O) μL | Zn(cur)O μL | [Zn(cur)O] μg/mL |
|---|---|---|---|---|---|
| ZnO | 100 | 1200 | 8300 | 2500 | 42 |
| Zn(cur)O (1.0) | 100 | 1200 | 8300 | 2500 | 42 |
| Zn(cur)O (1.0) | 903 | 9500 | - | 500 | 43 |

Measurements of arsenic concentration were analyzed by SOLAAR atomic absorption spectrophotometer (Thermo Labsystems) with ASX-510 autosampler, G95 graphite furnace, FS95 furnace autosampler, PLATON Hg sampling, MILESTONE

Ethos Plus microwave labstation, and SOLAAR data acquisition and analysis computer software.

The percentage adsorption of arsenic on adsorbate from aqueous solution was calculated as follows: Adsorption (%) = [($C_{int}$ - $C_{fin}$)/ $C_{int}$ ]*100 where $C_{int}$ and $C_{fin}$ are the initial and final arsenic concentrations in the solution, respectively.

### 3. Results and Discussion

a. Removal of arsenic by Zn(cur)O

When the initial As(III) concentration is 100 ppb (Fig. 3.1a), it is found that in just 30 minutes ~85, ~94, and ~90% of As(III) in the water sample could be removed with Zn(0.5cur)O, Zn(1.0cur)O, and Zn(2.0cur)O respectively, leaving As concentrations below MCL (7.865, 3.0845, and 4.679 respectively).  After 3 hours, the equilibrium As(III) concentration in the water sample was less than 5 ppb after the treatment, which meets the USEPA standard for arsenic in drinking water. Zn(1.0cur)O removed As(III) almost completely ($[As]_{180\ mins}$ = 0.933 ppb) with the highest adsorption percent (98%) followed by Zn(2.0cur)O (96%) and Zn(0.5cur)O (92%). Bare ZnO removed ~ 52% of the initial arsenic concentration after half an hour ($[As]_{60\ mins}$ ~20 ppb) and ~72% after 3 hours ($[As]_{180\ mins}$ ~ 14.6 ppb) failing to take arsenic down its MCL. When the initial As(III) concentration is 903 ppb ~71 and 67% of As(III) could be removed with Zn(1.0cur)O and Zn(2.0cur)O respectively in 30 mins. Even for such a high As(III) concentration, ZnO-curcumin nanostructures demonstrated an excellent removal effect given the low loading of 42 ppb (0.04 g/L). As(III) equilibrium concentrations of about 180 ppb were left after the treatment period of 3 hours achieving almost similar ~75% removal for both curcumin contents. Therefore, highly

efficient As(III) removal is possible with these curcumin-ZnO sub-micro-granules requiring no pre-treatment (oxidation and/or pH adjustment) and post treatment pH adjustment. It is expected that doubling or tripling the loading amount will remove the 903 ppb As contamination completely, even then the material loading is still considered economical.
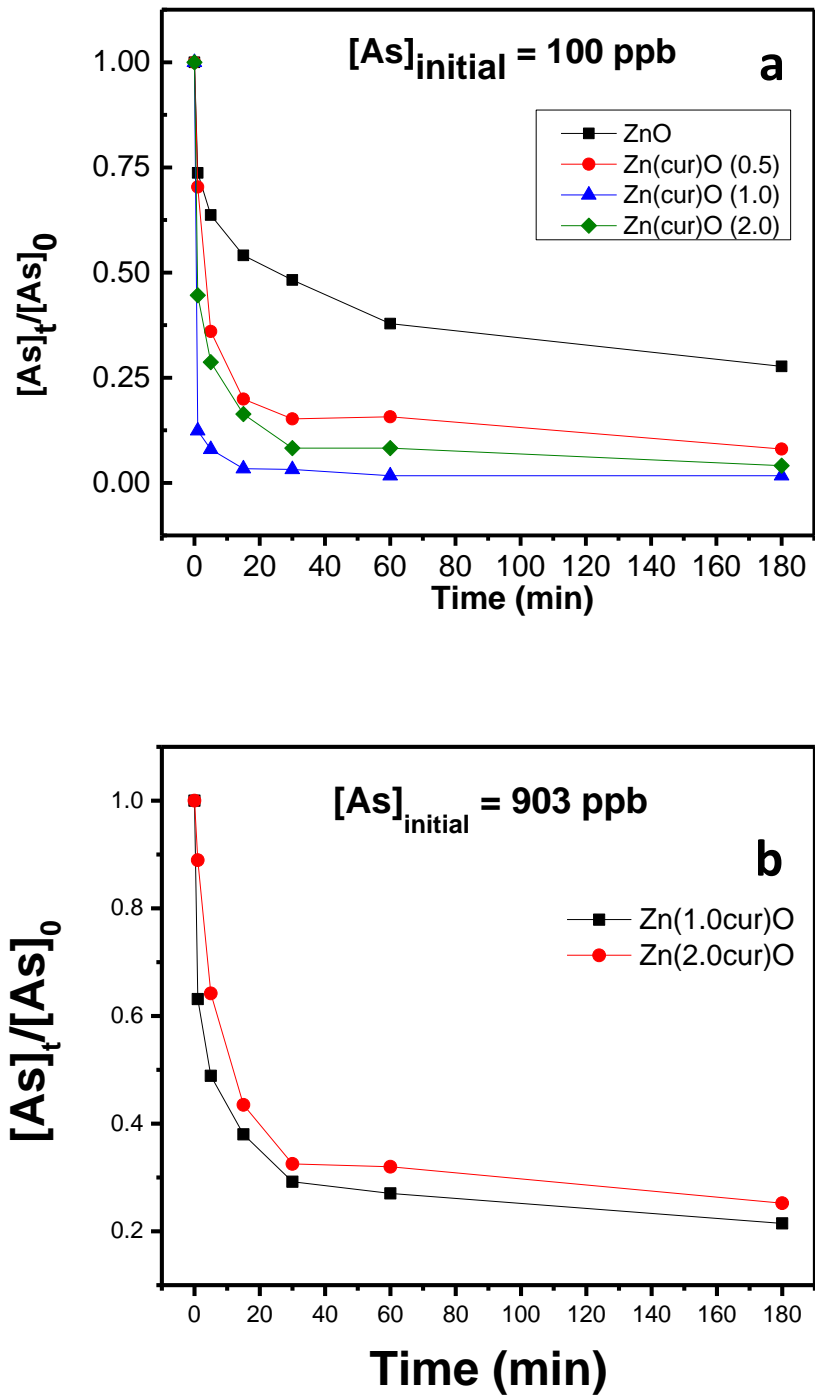
**Figure 3.1: Adsorption kinetics of As(III) on Zn(xcur)O and ZnO: a initial As(III) concentration is 100 μg/L and b initial As(III) concentration is 903 μg/L**
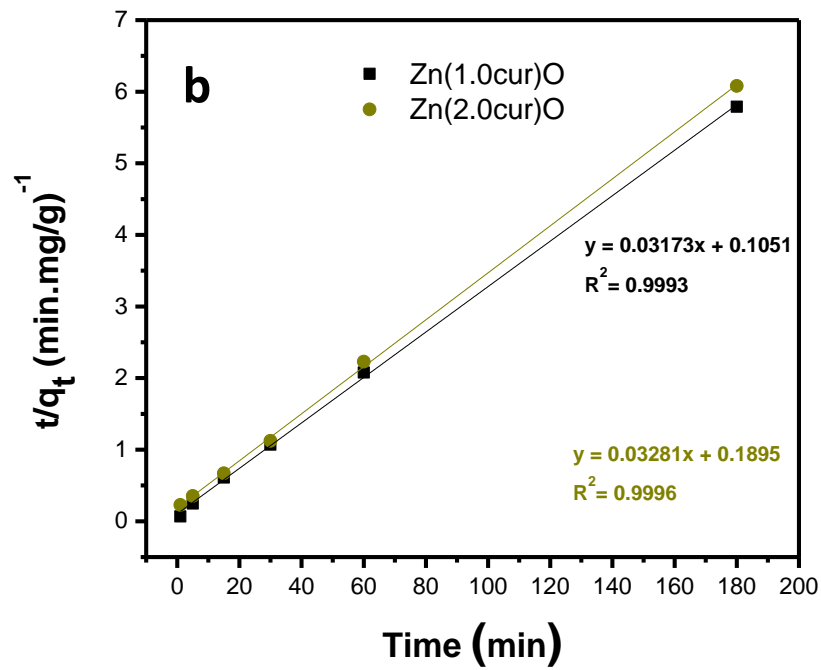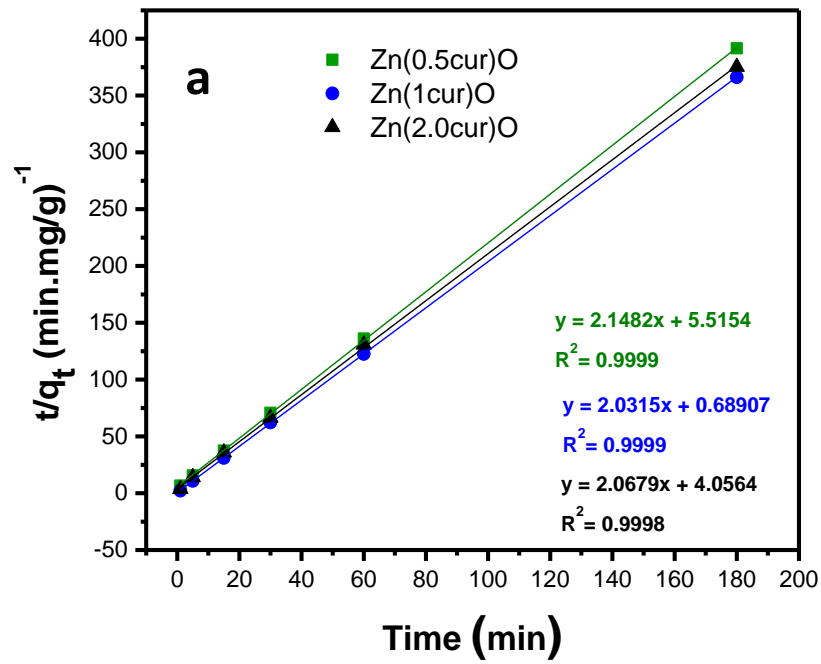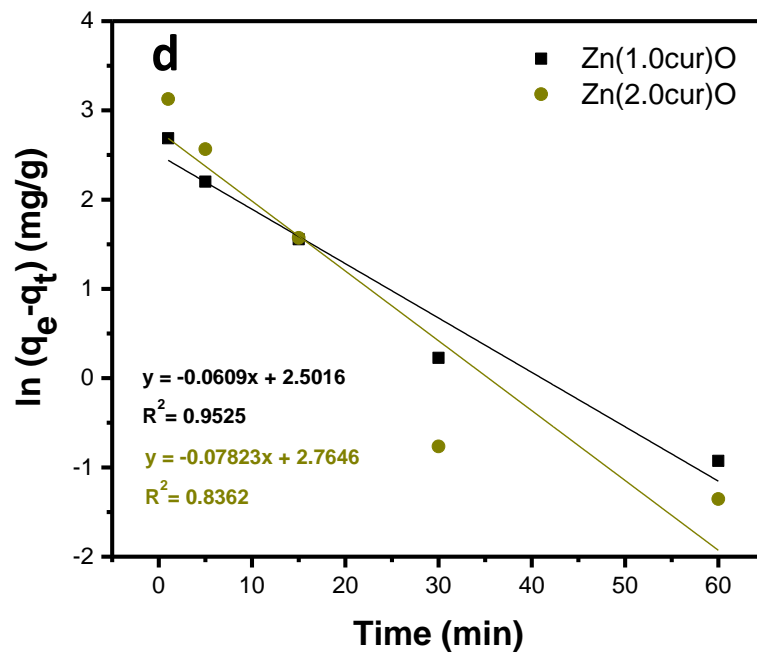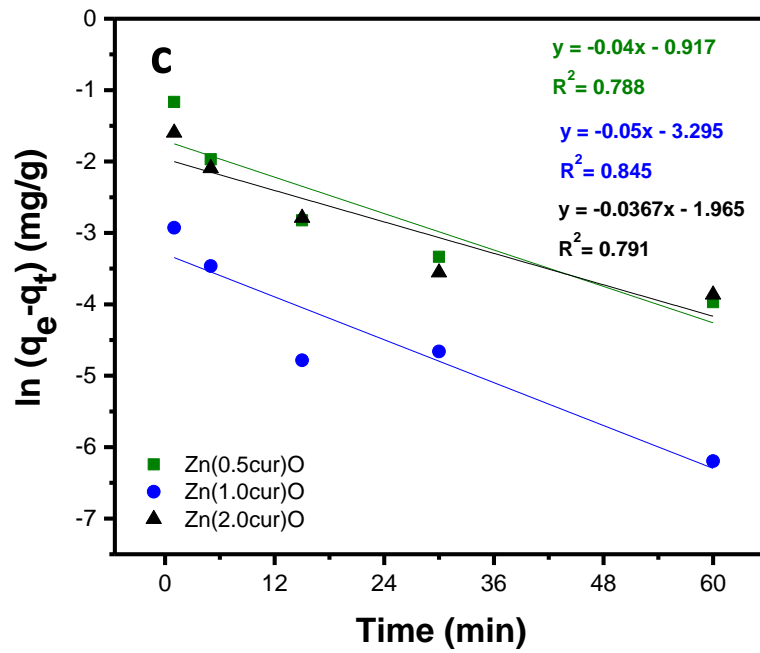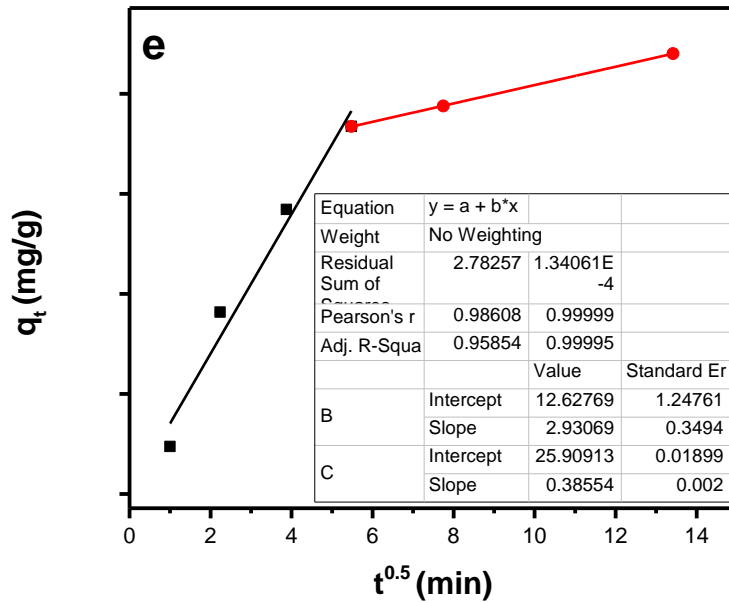
**Figure 3.2: (a) and (b) Pseudo-second-order rate kinetic model fitting of the adsorption kinetics studies demonstrated in Fig. 3.1a and 1b, respectively. (c) and (d) Pseudo-first-order rate kinetic model fitting of the adsorption kinetics studies demonstrated in Fig. 3.1a and 1b, respectively. (e) kinetics of arsenic adsorption (100 ppb) according to the intraparticle diffusion model for Zn(1.0cur)O**

Chemical kinetics is the study of rates of chemical processes and factors that affects reaching equilibrium in a reasonable duration. It also gives clue on the mechanism of the adsorption process, in addition to estimation of the loading of the adsorbent at equilibrium (capacity). To investigate the mechanism of adsorption, the Lagergren pseudo first-order and Lagergren pseudo second-order equations were used to test the experimental data of different curcumin content in the ZnO adsorbent. These are the common kinetic models. The linearized pseudo-first-order equation can be presented as[174]:

$$Ln\ (q_e-q_t) = -k_1t + ln\ q_e \qquad (eq.\ 3.1)$$

where $q_e$ and $q_t$ are the capacities (mg g$^{-1}$) of arsenic adsorbed at equilibrium and at time t, respectively, and $k_1$ is the pseudo-first-order rate adsorption constant (mg g$^{-1}$ min$^{-1}$).

Plot of ln ($q_e$-$q_t$) versus t for an adsorbent yields a straight line if the adsorption process follows pseudo-first-order kinetic behavior, usually governing the first 20-30 minutes of interaction. The rate constant was found to be dependent on the initial concentration of the adsorbate and varying greatly depending on the adsorption system.

The linearized pseudo-second-order equation is given as:

$$t/q_t = t/q_e + 1/(k_2\, q_e^2) \qquad \text{(eq. 3.2)}$$

$k_2$ is the pseudo-second-order rate constant and it depends on the operating conditions, such as initial pH and solution concentration, temperature, agitation rate, etc[174]. (All these parameters were kept constant for all the experiments). $k_2$ would decrease as the initial solution concentration increase as it takes a longer time to reach equilibrium.

If the adsorption system follows a pseudo-second-order kinetics, then a plot of $t/q_t$ versus t would be linear and $k_2$ and $q_e$ can be determined from the intercept and slope of the graph Eq. (3.2). Unlike the pseudo first order equation, the pseudo second order rate equation is likely to predict the behavior over the whole range of adsorption and the rate limiting step is assumed to be chemical adsorption[175] involving valency forces through sharing or the exchange of electrons between the adsorbent and the metal ion.

The amount of arsenic adsorbed at equilibrium was calculated by:

$$q_e = V(C_o - C_e)/m \qquad \text{(mg g}^{-1}\text{)} \qquad \text{(eq. 3.3)}$$

where $C_o$ and $C_e$ are the initial and equilibrium concentration (mg/L) respectively, m is the mass of dry adsorbent used (g) and V volume of solution (mL).

The kinetic study results could be best fitted into a pseudo second- order rate kinetic model as demonstrated in Fig. 3.2a and b. The kinetic parameters obtained in fitting the experimental data are summarized in Table 1. The applicability of the pseudo-second-order rate model was evaluated by the square of the correlation coefficient R ($R^2$), and

its closeness to 1 indicates that the model fits the experimental data accurately. The correlation coefficients for the second-order kinetic model are greater than 0.999 for all the fits.

Due to the differences in the experimental conditions, it is not possible to directly compare the adsorption efficiency among reports in literature. However, a rough comparison can be made. For instance, concerning relatively high arsenic concentrations, Yang and co-workers[173] synthesized ZnO micro-tubes which have a large specific surface area. In their study, the initial As(III) solution concentration is 0.9032 mg/L, pH value at 7.0, and the amount of ZnO loading at 0.08 g/L, the $k_{ad}$ is determined at 0.005 $mg^{-1}$ g $min^{-1}$; it increases to 0.015 $mg^{-1}$ g $min^{-1}$ upon loading with 0.1 g/L. In our study, having the same initial As(III) concentration, pH value at 6, and much lower adsorbent loading of 43 µg/L, the $k_{ad}$ is determined to be higher (0.0096 and 0.0057 $mg^{-1}$ g $min^{-1}$ for Zn(1.0cur)O and Zn(2.0cur)O respectively) (Table 1). For the low arsenic concentration range, the aforementioned study obtained 0.007 $mg^{-1}$ g $min^{-1}$ $k_{ad}$ with an initial As(III) solution concentration of 0.0978 mg/L, pH value at 7.0, and the amount of ZnO loading at 0.01 g/L (10 mg/L). In comparison, for almost similar As concentration of 0.1 mg/L and material loading 230 times less, we obtained much higher $k_{ad}$ of 0.837, 5.99, and 1.05 $mg^{-1}$ g $min^{-1}$ for curcumin contents of 0.5mg, 1.0mg, and 2.0mg respectively. These ZnO micro-tubes themselves have surpassed the nanocrystalline $TiO_2$ with a large specific surface area of 330 $m^2$/g synthesized by Meng and co-workers[173]. In their study, the initial As(III) solution concentration is 2.0 mg/L, the pH value is 7.0, and the amount of $TiO_2$ is 0.2 g/L. They reported $k_{ad}$ to be 0.00025 $mg^{-1}$ g $min^{-1}$. The surface area of the adsorbent is not the only property that ensures the efficiency of the adsorbent; other factors are critical which include the type

and number of surface functional groups on the adsorbents. And as the surface area of

these nanostructures is no greater than the nanocrystalline $TiO_2$ and probably the ZnO

microtubes, these significant results suggest that curcumin conjugated ZnO

nanostructures possess an excellent affiliation to As(III) due to the functionalities of the

curcumin.

**Table 3.2: Kinetic parameters of Zn(x.cur)O nanostructures adsorption on As(III) at initial concentrations of: (a) 100 ppb and (b)903 ppb**

| a) | $q_{e(cal)}$ (mg g$^{-1}$) | $k_{ad}$ (mg$^{-1}$ g min$^1$) | $R^2$ |
|---|---|---|---|
| Zn(0.5cur)O | 0.4655 | 0.8367 | 0.9999 |
| Zn(1.0cur)O | 0.4922 | 5.9892 | 0.9999 |
| Zn(2.0cur)O | 0.4836 | 1.0542 | 0.9996 |

| b) | $q_{e(cal)}$ (mg g$^{-1}$) | $k_{ad}$ (mg g$^{-1}$ min$^1$) | $R^2$ |
|---|---|---|---|
| Zn(1.0cur)O | 31.5160 | 0.009579 | 0.9993 |
| Zn(2.0cur)O | 30.4785 | 0.005681 | 0.9996 |

The sorption kinetics can also be described from a mechanistic point of view.

The adsorption process may be controlled by one or more steps, e.g. film or external

diffusion, pore diffusion, surface diffusion and adsorption on the pore surface, or a

combination of more than one step[176]. A process is diffusion-controlled when its rate

depends on the rate at which components diffuse towards one another. The possibility

of intra-particle diffusion was explored by using the intra-particle diffusion model,

according to the equation: $q_t = k_{id} t^{0.5}$     (eq. 3.4)

Where $k_{id}$ is the intra-particle diffusion rate constant (mg/(g.min$^{0.5}$). If the so-called

Weber–Morris [27] plot of $q_t$ versus $t^{0.5}$ gives a straight line, then the sorption process is

controlled by intra-particle diffusion only. However, if the data exhibit multi-linear plots, then two or more steps influence the sorption process. It is assumed that the external resistance to mass transfer surrounding the particles is significant only in the early stages of adsorption: this is represented by the first sharper portion. The second linear portion is the gradual adsorption stage with controlling intra-particle diffusion.

Fig. 3.2e presents the plots of 100 ppb arsenic uptake versus $t^{0.5}$ for Zn(1.0cur)O. Similar multi-linear plot profiles were obtained for all the adsorbents presented in figure 3.2 a and b. In the figure 3.2e, the data points are related by two straight lines – the first straight portion depicting macropore and mesopore diffusion and the second representing micropore diffusion. The deviation of straight lines from the origin (Fig. 3.2e) may be due to difference in rate of mass transfer in the initial and final stages of adsorption. The slope of the plot is defined as a rate parameter, characteristic of the rate of adsorption in the region where intra-particle diffusion is rate controlling.

The arsenic species present at pH 6 is $H_3AsO_3$. As(III) species is thought to adsorb on the phenyl rings of curcumin band/or to the hydroxyls groups. One might argue that if this's the case, higher curcumin content should reflect a higher adsorption capacity, which is not seen in the results. In fact, the higher curcumin content (2 mg) incorporated in ZnO could be blocking the adsorption sites by stacking of phenyl rings or hydrogen bonding of hydroxyl groups of curcumin preventing adsorption of As(III).

b. Sensing of arsenic by Zn(cur)O

The sensing of arsenic was done for two concentration ranges: from 0 to 1000 ppb (1 ppm) and from 1 ppm to 10 ppm; thus, stock solutions of respectively 3 ppm and

30 ppm of arsenic in water were used for this purpose. A stock solution of 0.3 g/L Zn(cur)O (1.0) in ethanol was also prepared. Zinc oxide was tested as a control for arsenic removal, following the same procedure. The following samples were prepared with a final volume of 3 mL setting the final concentration of Zn(cur)O to 0.1 g/L. The samples were prepared as following.

**Table 3.3: Concentrations and volumes used of As and Zn(cur)O in samples prepared ▲using 3 ppm stock ▼using 30 ppm stock**

| Zn(cur)O μL | [Zn(cur)O] g/L | V(As) μL | V(H$_2$O) μl | [As] ppb ▲ | [As] ppm ▼ |
|---|---|---|---|---|---|
| 1000 | 0.1 | 100 | 1900 | 100 | 1 |
| 1000 | 0.1 | 200 | 1800 | 200 | 2 |
| 1000 | 0.1 | 300 | 1700 | 300 | 3 |
| 1000 | 0.1 | 500 | 1500 | 500 | 5 |
| 1000 | 0.1 | 700 | 1300 | 700 | 7 |
| 1000 | 0.1 | 800 | 1200 | 800 | 8 |
| 1000 | 0.1 | 1000 | 1000 | 1000 | 10 |

The steady-state fluorescence (emission and excitation) measurements were recorded with resolution increment 1 nm, slit 5 using Jobin-Yvon-Horiba Fluorolog III fluorometer and the FluorEssence program. The excitation source was a 100 W Xenon lamp, and the detector used was R-928 operating at a voltage of 950 V.
The emission spectra were obtained for excitations at 280 nm and 425 nm.
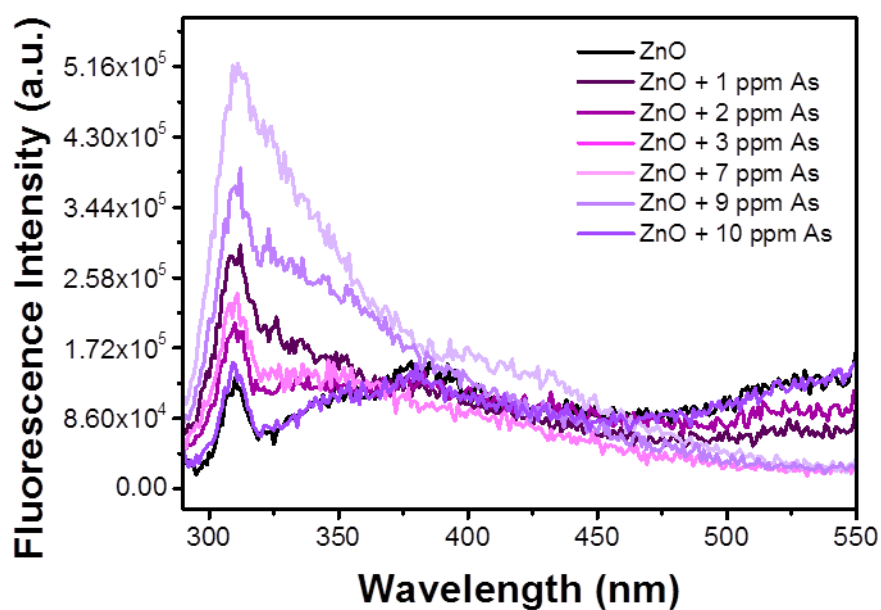
**Figure 3.3: Fluorescence sensing of As in the concentration range 1 to 10 ppm using ZnO**
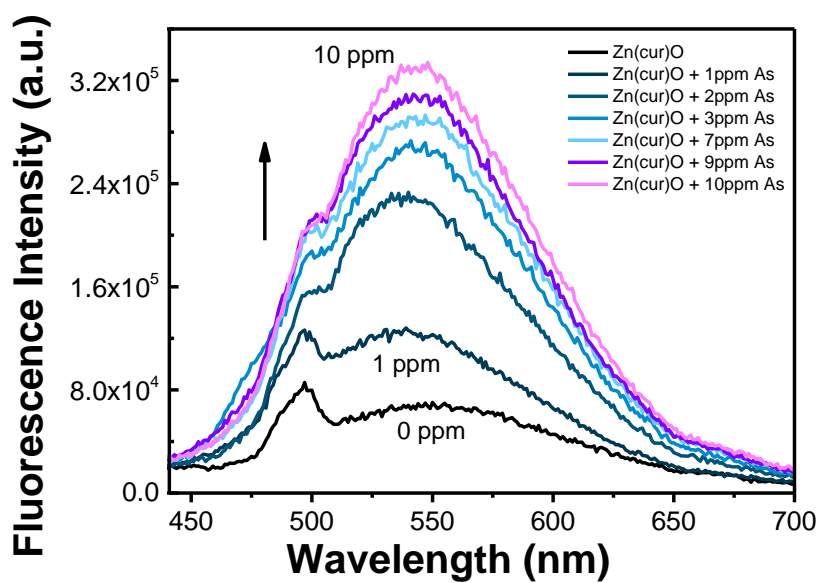


**Figure 3.4: Fluorescence sensing of As in the concentration range 1 to 10 ppm using Zn(1.0cur)O**
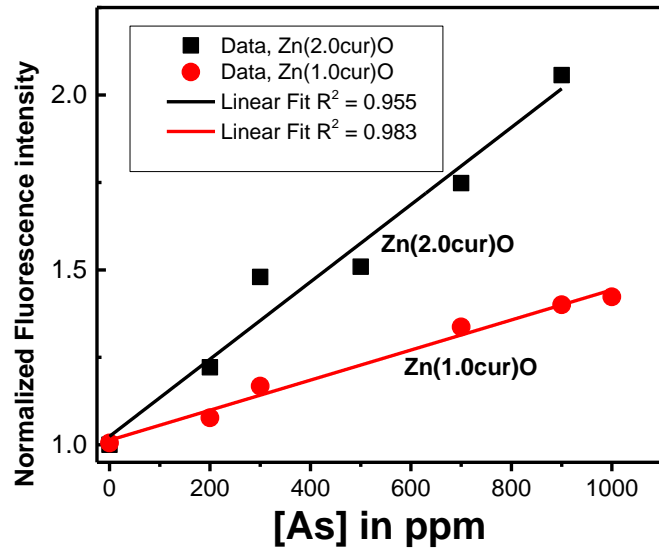
**Figure 3.5:** **Fluorescence intensity response of Zn(1.0cur)O and Zn(2.0cur)O in the As concentration range 200 to 1000 ppb at excitation wavelength 425 nm and emission wavelength 550 nm.**
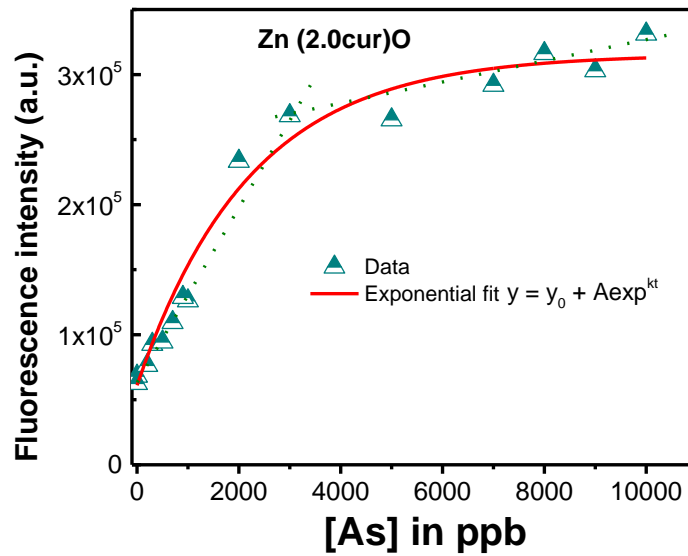


**Figure 3.6:** **Fluorescence intensity response of Zn(2.0cur)O in the As concentration range 0 to 10000 ppb (10 ppm) at excitation wavelength 425 nm and emission wavelength 550 nm.**

ZnO didn't show any systematic fluorescence alteration in both the range of arsenic concentrations used at excitation wavelengths 280 nm (Fig. 3.3) and 425 nm (not shown), which limits use of ZnO to sense As. However, Zn(cur)O (1.0) showed an increased photoluminescence (PL) intensity with increasing [As] from 1 to 10 ppm (Fig. 3.4). To test effect of curcumin concentration in Zn(cur)O, a comparison was made for response for Zn (1.0cur)O and Zn (2.0cur)O as depicted in Fig. 3.5 in the concentration range 0 to 1000 ppb and both of them showed good linear change in fluorescence signal. The higher fluorescence intensity change for Zn(2.0cur)O is due to higher fluorescence of Zn(2.0cur)O compared to Zn(1.0cur)O as found in fluorescence spectroscopic study in Chapter 2. Further, the response was extended up to 10000 ppb (10 ppm) using Zn(2.0cur)O as fluorescence probe for sensing application. As shown in Fig. 3.6 the fluorescence response showed an exponential increase and at higher concentration it started saturating. From Fig. 3.6 it can be estimated that the linear changes for sensing application is till around 3000 ppb of As, where the present method could be applicable to determine As in water samples.

## B. Curcumin-sensitized ZnO for enhanced photodegradation of PAHs under sunlight

### 1. Introduction

Polycyclic aromatic hydrocarbons (PAHs) are hydrocarbons containing two or more fused benzene rings. PAHs exhibit different physical and chemical properties depending on their molecular weight[177]. PAHs are neutral nonpolar compounds that are highly stable which makes it a difficult task to get these compounds to be degraded. Generally, as the number of fused benzene rings in PAHs increase, its hydrophobicity increases and its solubility and volatility decrease. As PAHs accumulate in soil, water, and air causing environmental pollution, humans are exposed to these chemicals as part of everyday living. They come at the top of the pollutants list of US EPA and European Union, especially those with four or more rings, due to their toxic, mutagenic, and carcinogenic potential [178]. PAHs can act as an endocrine disruptor or carcinogenic/mutagenic affecting growth, reproduction, the immune system and even survival of exposed organisms. These compounds are introduced to the environment through natural and anthropogenic processes. The main natural sources are volcanic eruptions and forest and prairie fires, which introduce PAHs into the atmosphere[179]. Also, fungi are proposed to be the major precursor carriers for perylene in sediment[180]. Anthropogenic sources of PAHs include oil spills from crude and refined petroleum, introduced to aquatic environments through accidental discharge from tanks and municipal and urban pipes. These sources were found to yield high molecular weight PAHs[181-183]. On the other hand, the generation of low molecular weight PAHs is produced by incomplete combustion of fossil fuels (coal and petroleum) and biomass at high temperatures, such as burning wood, which are released into the

environment in the form of exhaust and solid residues[184-187]. Also, smoking, gas cooking, unvented kerosene heating, and heating appliances can significant sources in indoor air[188-189].

Effective and economic methods to decontaminate water are needed. PAHs contaminated water can be processed efficiently by biological treatment plants or by adsorption with activated carbon or other adsorbents, or by conventional chemical treatments (thermal oxidation, ozonation, chlorination, potassium permanganate, etc.)[190]. However, these procedures have failed to achieve the purity required by law in certain cases and conditions. One of the major transformation processes resulting in the degradation of PAHs and other contaminants in water is photolysis. In these sunlight photo-alteration processes, highly reactive intermediates are generated; mainly hydroxyl radical ($^{\bullet}$OH), a powerful non-specific oxidant ($E_{\circ}$ = 2.8 V)[190].

Oxidation processes have been developed as solutions to remove persistent organic pollutants dissolved in the aquatic environment. These so called Advanced Oxidation Processes (AOPs) are based on catalytic and photochemical reactions to change profoundly the chemical structure of pollutants[190]. They can be used alone or in combination with conventional methods [191].These photocatalytic oxidation processes (PCO) employ the use of semiconductor materials (ZnO and $TiO_2$) for the removal of the residual concentrations of several PAHs from groundwater below the standard levels. Advantages of the photocatalytic process over other techniques include its mild operating conditions and its reliance on sunlight as the power source, thus reducing significantly the operating costs of electric power required.

PCO is a process that mainly relies on the generation of reactive $^{\bullet}OH$ to trigger oxidative degradation. Other reactive species such as superoxide radical anions ($^{\bullet}O_2^{-}$) and $h^{+}$ on catalyst molecules also leads to the formation of detected intermediates[192].

Many semiconductors such as $TiO_2$, $WO_3$, $ZrO_2$, $SnO_2$, $Fe_2O_3$, CdS, ZnS, $WS_2$ and $MoS_2$ among which is ZnO have been tested for the photocatalytic degradation of various environmental contaminants[35]. The pre-requisite for an efficient semiconductor catalyst is that the valence band and conduction band (CB) of the catalyst should be positioned in such a way that the oxidation potential of the hydroxyl radical ($E_o$ ($H_2O/^{\bullet}OH$) = 2.8V vs. NHE) and the reduction potential of superoxide radical ($E_o$ ($O_2/O^{\bullet}_2^{-}$) = -0.28V vs. NHE) lie well within the band gap [193]. $TiO_2$, ZnO and $ZrO_2$ suit this criterion compared to other catalysts. In fact, some recent experimental results have shown that ZnO had higher photocatalytic activities than $TiO_2$ and other semiconductor catalysts such as CdS, $WO_3$, $Fe_2O_3$, $SnO_2$ and $ZrO_2$ especially for dye degradation in aqueous solutions[194-197]. An additional advantage of ZnO is its low cost and that it absorbs over a larger portion of the solar spectrum than $TiO_2$[194]. For this reason, ZnO is considered the most suitable photocatalyst for photocatalytic removal in the presence of sunlight. Since the minimum energy required for excitation of an electron for ZnO is 3.2 eV, which corresponds to 387.5 nm, and UV light (<387 nm) in solar light is less than 4%, the application of ZnO is limited. To expand the use of ZnO photo-response to the visible region, surface modification and dye sensitization are effective methods that are similar to previously reported $TiO_2$ modification techniques.

**Table 3.4: The conduction band and valence band positions of common semiconductors catalysts at pH 1. [35]**

| Semiconductor | VB (V vs. NHE ±0.1 V) | CB (V vs. NHE ±0.1 V) | $E_g$ (eV) |
|---|---|---|---|
| ZnO | +3.0 | −0.2 | 3.2 |
| $TiO_2$ | +3.1 | −0.1 | 3.2 |
| $WO_3$ | +3.0 | +0.2 | 2.8 |
| $ZrO_2$ | +4.0 | −1.0 | 5.0 |
| $Fe_2O_3$ | +2.9 | +0.6 | 2.3 |
| $SnO_2$ | +4.1 | +0.3 | 3.8 |
| ZnS | +1.4 | −2.3 | 3.7 |
| CdS | +2.1 | −0.4 | 2.5 |
| CdSe | +1.6 | −0.1 | 1.7 |
| GaAs | +1.0 | −0.4 | 1.4 |

VB, valence band; CB, conduction band; and $E_g$, band gap energy

In their recent work, Kou et al. [198] showed that GaN:ZnO has excellent activity for the photodegradation of PAHs, with the following order of effectiveness: phenanthrene> benzo[a]anthracene > anthracene > acenaphthene, with complete degradation after 1, 3, 6 and 8 h, respectively. On the other hand, Dass et al. [199] tested the degradation of acenaphthene, anthracene, fluorene and naphthalene in aqueous suspension of $TiO_2$ under UV and natural light irradiation, which came out to be highly effective due to the formation of hydroxyl and superoxide radicals. In another study, Ireland et al. [200] obtained half-lives of 2.7 h in the case of anthracene and 380 h for fluoranthene using $TiO_2$. Wen et al. [201] found that phenanthrene (PAH of low solubility) in aqueous $TiO_2$ suspensions under UV light irradiation was completely degraded after 40 minutes without significant effect of pH or amount of photocatalyst on degradation.

Principle of ZnO photocatalysis and mechanistic pathways[35]: In heterogeneous photocatalysis, the increase in the rate of a thermodynamically allowed ($\Delta G<0$) reaction in the presence of photocatalyst is due to the arise of new reaction pathways of photogenerated species and a decrease of the activation energy[202-203]. Under UV light irradiation, ZnO absorbs energy of equivalent or greater than its band gap energy and the electron is excited from the valence band VB to the conduction band CB. The wavelength for UV light energy typically corresponds to $\lambda < 387$ nm. The excitation leaves behind a positive hole in the VB creating the electron–hole pair ($e$-$h^+$). The $e^-/h^+$ pair should be trapped by electron and hole scavengers to avoid its recombination. The positive hole is a strong oxidant which can either directly oxidize adsorbate pollutants or react with electron donors such as water or hydroxyl ions ($OH^-$) to form hydroxyl radical ($^\bullet OH$), which is also a potent oxidizing agent. As for the electron in the CB, it can be scavenged by one of the efficient electron acceptors like molecular oxygen ($O_2$). Through the reduction of $O_2$ with electron, reactive superoxide radical anions ($O_2^{\bullet -}$) are produced. Together with other oxidizing species such as hydroperoxyl radicals ($HO_2^\bullet$) and hydrogen peroxide ($H_2O_2$) additional $^\bullet OH$ radicals are generated.

Essentially $O_2^{\bullet -}$, $HO_2^\bullet$, and $^\bullet OH$ radicals as well as photogenerated holes ($h^+$) are highly reactive intermediates that will attack repeatedly in the reacting system and ultimately lead to complete mineralization of the organic pollutants.

As Zn(cur)O showed sensitization to visible light upon anchoring the natural dye curcumin to the photocatalyst, an increased photo-activity of the novel photocatalyst was expected and thus it was tested under sunlight. In line with exploring the environmental applicability of Zn(cur)O as a detoxifying material, the degradation

activity of the compound was tested on PAHs; mainly perylene, fluoranthene, and chrysene.

## 2. Experimental

Prepare 30 mL of 50 µM (12.6 µg/L) perylene from 1 mM stock solution (perylene in acetonitrile). Add 5 mg of Zn(cur)O (1.0) into the pervious solution while stirring (167 mg/L). Immediately withdraw 5 mL of the solution after centrifuging or allowing the compound (Zn(cur)O) to settle down to make sure no Zn(cur)O is being withdrawn along. Measure UV of the sample withdrawn. Keep stirring and repeat the UV measurements as indicated after 10-20 minutes interval depending on the rate of degradation. The same procedure was followed with fluoranthene (11.4 µg/L) and chrysene (11.1 µg/L). The catalytic degradation was studied by recording absorption spectra at room temperature using a JASCO V-570 UV-VIS-NIR Spectrophotometer.

## 3. Results and discussion

The photo catalytic activity of ZnO and Zn(cur)O were investigated using perylene. The catalytic degradation of perylene (Fig. 3.7) was monitored by UV-visible spectrophotometer at 406 nm wavelength for various time intervals after filtering out Zn(cur)O. Fluoranthene was monitored at 280 nm and chrysene at 360 nm. As shown in Fig. 3.7a the absorbance of perylene continued to decrease with time indicating its degradation. Note that the degradation process is so fast and onsets as soon as Zn(cur)O is added to perylene as noted from the absorbance recorded just before any addition of

the photocatalyst and immediately after mixing and filtering out Zn(cur)O. It was

observed that the extent of doping affected the rate of degradation of perylene.

The change in absorbance with time during catalytic degradation of perylene by

Zn(cur)O is given in Figure 3.7b,c. The data fitted well to a first order rate law as:

$$\frac{-d\,[PAHs]}{dt} = k\,[PAHs] \quad \text{(eq. 3.4)}$$

where $k$ is the first order rate constant. The half-life of the reaction, which is

independent of initial concentration, was used to compare activities of different

Zn(cur)O and ZnO. The half-life was calculated as:

$$t_{1/2} \;=\; \frac{ln(2)}{k} \qquad \text{(eq. 3.5)}$$
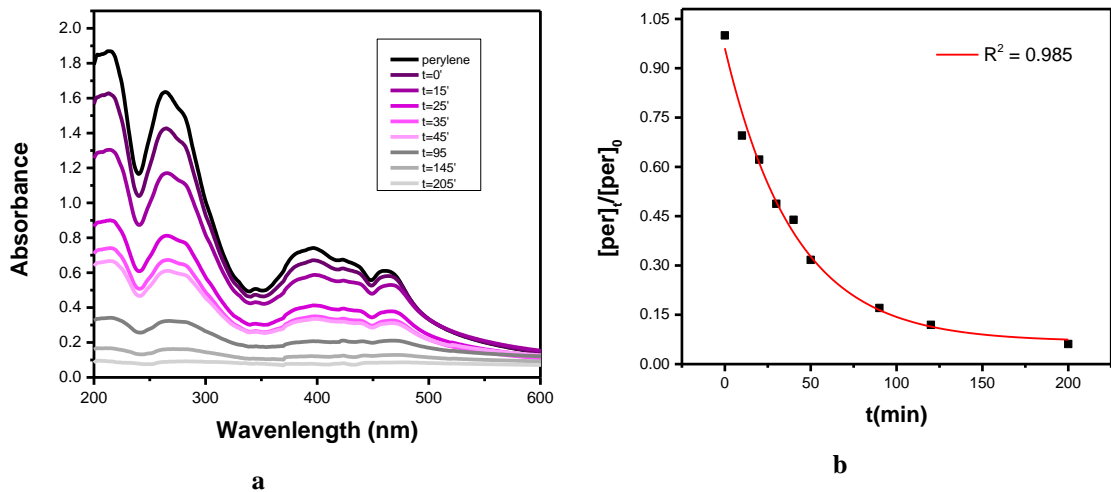


**Figure 3.7: (a) UV-visible absorption spectra of perylene during degradation by Zn(cur)O; (b) Plot of change absorbance change with time, the fitting shown a first order rate equation**

It was found that when 0.5 mg of curucmin was used during synthesis of

Zn(cur)O, the half-life reduced about 24 % than that of bare ZnO. Such an increase is

expected as the curcumin incorporation allows exploiting the sun's visible light energy

and thus a faster degradation is expected. There was a slight decrease in half-life when 1.5 mg of curcumin was incorporated. It is clear that the extent of curcumin doping during preparation of Zn(cur)O affects the catalytic activity of Zn(cur)O in some way. The recyclability of Zn(cur)O was tested where the degradation of perylene was studied in three consecutive cycles by reusing the same compound over and over again. The half-life of perylene degradation increased exponentially in each cycle indicating that the catalytic activity of Zn(cur)O gets reduced hugely.

The degradation of other PAHs like chrysene and fluoranthene (Fig. 3.9 and 3.10 respectively) was also tested by the suggested Zn(cur)O catalyst. In comparison to perylene, it was found that the half-life reduced appreciably by 33 % for chrysene and remarkably by 99 % for fluoranthene (Fig. 3.10). A possible explanation for this increase in the rate of degradation when going from perylene to chrysene then to fluoranthene is the decreased number of aromatic rings or in other words the loss of conjugation that confers stability and resistance to the molecule. In fact, fluoranthene is a non-alternate PAH (presence of a 5 membered ring) whereas both perylene and chrysene are alternate PAHs, with perylene having more cyclic rings than chrysene. Thus, perylene and chrysene- being highly aromatic and more stable than fluoranthene- are expected to be less easily degraded compared to fluoranthene as confirmed by the results. It's worth noting, that the relatively low Zn(cur)O loading of 167 mg/L showed good degradation ratios of 88% for relatively high concentrations of 12.6 μg/L perylene after 3.4 h, 93% for 11.4 μg/L fluoranthene in 25 minutes and 11.1 μg/L chrysene in 2.2 h.
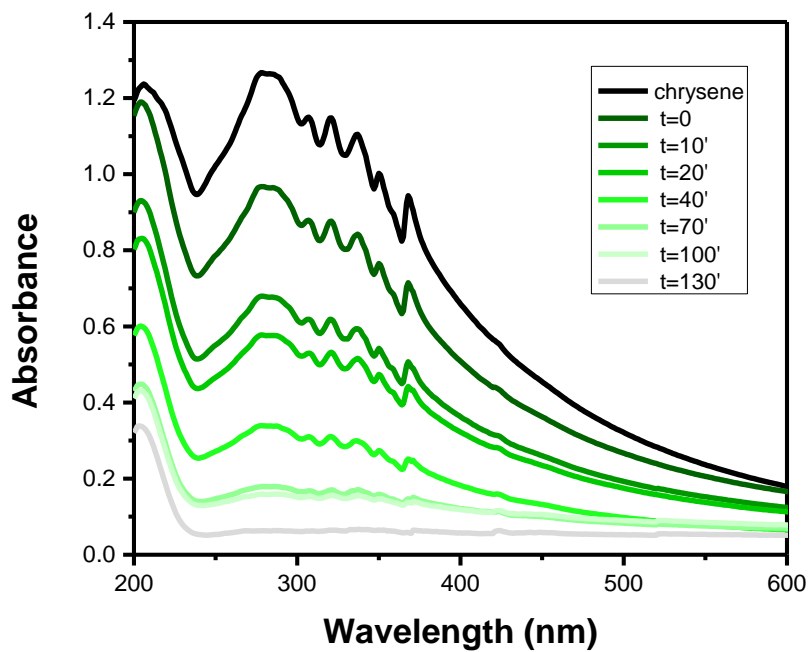
**Figure 3.9: UV-visible absorption spectra of chrysene during degradation by Zn(cur)O**
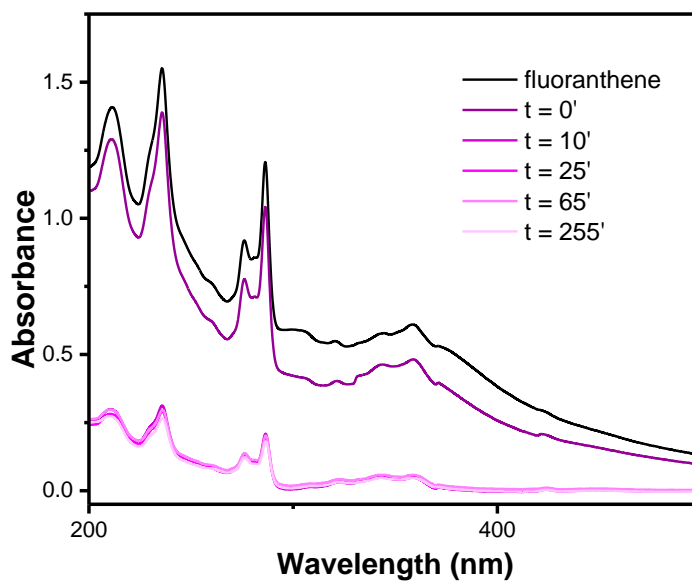


**Figure 3.10: UV-visible absorption spectra of fluoranthene during degradation by Zn(cur)O**
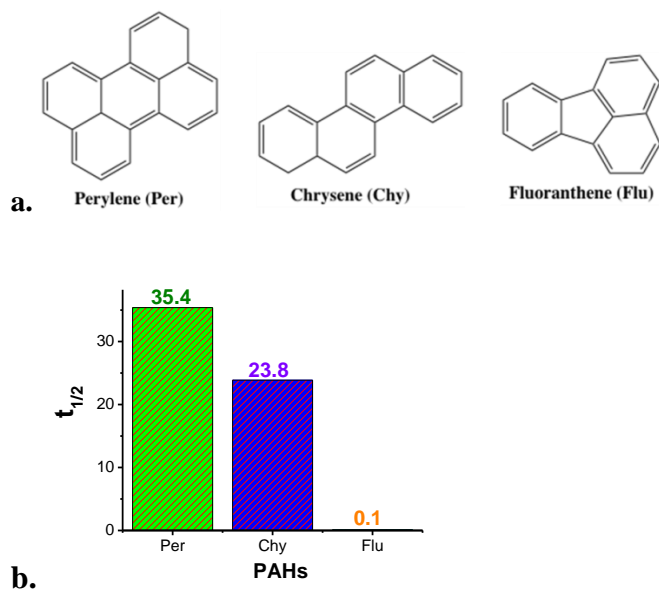
**Figure 3.11: (a) Structure of perylene, chrysene and fluoranthene.(b) Comparison of half-life value during PAHs degradation by Zn(cur)O.**

The light utilized is that of sunlight (i.e., both UV and visible light). Photolysis is one of the major transformation processes affecting the fate of PAHs in the aquatic environment. Sunlight photoalteration processes are well known to play an important role in the degradation of PAHs and other contaminants in water by generation of highly reactive intermediates, mainly hydroxyl radical ($^*$OH), a powerful non-specific oxidant (E∘ = 2.8 V)[190]. PAHs' degradation could be due to direct photolysis since those compounds absorb light in the 200–400 nm range which overlaps the emission spectrum of sunlight. However, under sunlight and with no photocatalyst, the PAHs are found to degrade slowly compared with the reaction rates in the presence of photocatalysts, especially ZnO. Based on a work done on the "removal of polycyclic aromatic hydrocarbons (PAHs) from groundwater by heterogeneous photocatalysis under natural sunlight"[190], 12% of 2-5 µg/L of fluoranthene remained after only 10 minutes with ZnO loading of 150 mg/L in comparison to 40% remaining after 50

minutes due to photolysis. The result of the current work is a 93% removal (7% remaining) of 11.4 µg/L fluoranthene with 167 mg/L Zn(cur)O loading after 10 minutes, which is comparable to the result obtained when the photocatalyst ZnO was present. This clearly rules out photolysis and attributes the degradation to the act of the photocatalyst used, i.e., to photocatalysis. The obtained results are quite promising if we take into consideration the moderate set of working conditions. For instance, the $O_2$ requirement was provided by simply letting air go through the Erlenmeyer's opening, unlike other experiments where oxygen is purged continuously into the solution. Another important parameter which has a significant effect on the rate is the light intensity which is considered weak in comparison to higher intensities used in studies.

Photocatalytic reaction mechanism in the ZnO/curcumin system

For dye sensitization to be possible, the conduction band edge of the ZnO must be lower (more positive) than the LUMO level of the dye molecule, so that the excited electron of the dye can be injected into the semiconductor's conduction band (CB). The reduction potential of the organic contaminant must be higher (more negative) than the HOMO of the dye molecule. This condition is satisfied for the ZnO/curcumin system. Therefore, upon the photo-excitation of Zn(cur)O by a light with $\lambda \geq 445$ nm and the consequent generation of electrons (e) and holes (h) in the conduction band (CB) and valence band (VB) respectively of curcumin, the excited electron is injected into the conduction band of ZnO (Eq. (2)). Then, the electron in the conduction band ($e^-_{CB}$) is transferred to molecular oxygen, leading to the formation of a series of radicals, which are active oxidizers capable of degrading organic pollutants in the system (PAHs) (Eqs.

70

(3)–(8)). Subsequently, the pollutants can be degraded through a variety of paths (Eq.11).

Positive holes are thought to be trapped at the semiconductor's surface and that they would readily react with surface absorbed water molecules or hydroxyl groups forming hydroxyl radicals (Eq. 9,10) [204-207] It is also proposed that holes can directly oxidize adsorbed organic molecules resulting in the formation of organic radical cations [208-209]which will subsequently undergo further oxidation and thus degradation. Scheme 3.1 summarizes the mechanism.
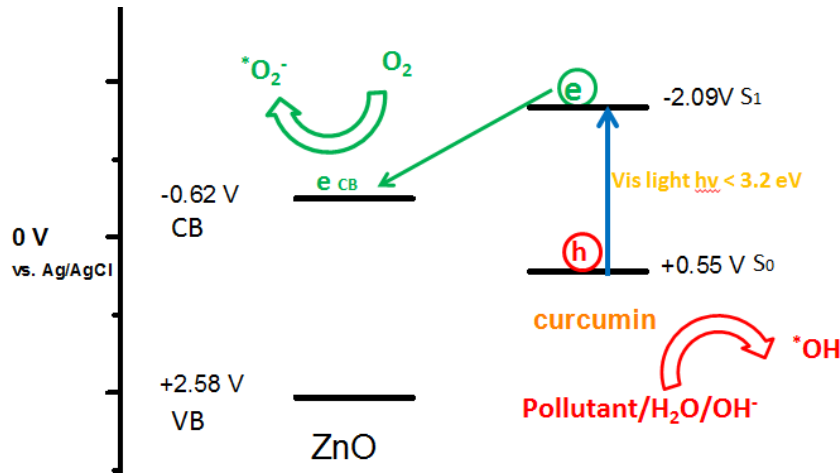


**Scheme 3.1: Schematic representation of the electron and hole transfer processes in the ZnO/curcumin systems.**

ZnO photocatalytic mechanism has been proven to be similar to that of $TiO_2$[210]. The suggested working mechanism is summarized in the following equations (1)–(11)[211]:

Curcumin/ZnO + visible light $\rightarrow$ curcumin$^*$/ZnO          (1)

curcumin$^*$/ZnO $\rightarrow$ curcumin$^{*+}$/ZnO + e$^-$ $_{CB}$          (2)

e$^-$ $_{CB}$ + $O_2$ $\rightarrow$ $^{\bullet}O_2^-$          (3)

$$H_2O + {}^\bullet O_2{}^- \rightarrow {}^\bullet OOH + OH^- \qquad\qquad (4)$$

$$2\ {}^\bullet OOH \rightarrow O_2 + H_2O_2 \qquad\qquad (5)$$

$${}^\bullet OOH + H_2O + e^-{}_{CB} \rightarrow H_2O_2 + OH^- \qquad\qquad (6)$$

$$H_2O_2 + e^-{}_{CB} \rightarrow {}^\bullet OH + OH^- \qquad\qquad (7)$$

$$H_2O_2 + {}^\bullet O_2{}^- \rightarrow {}^\bullet OH + OH^- + O_2 \qquad\qquad (8)$$

$$H_2O_{ads} + h^+ \rightarrow {}^\bullet OH_{ads} + H^\bullet \qquad\qquad (9)$$

$$OH^- + h^+ \rightarrow {}^\bullet OH \qquad\qquad (10)$$

$${}^\bullet OH\ /{}^\bullet O_2{}^-\ /\ curcumin^{\bullet +} + pollutants\ (PAHs) \rightarrow degraded\ products \qquad (11)$$
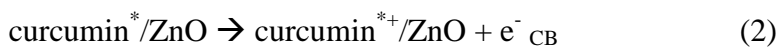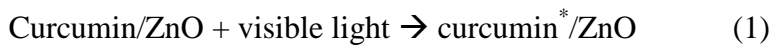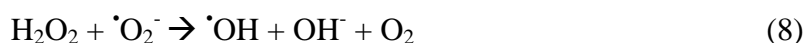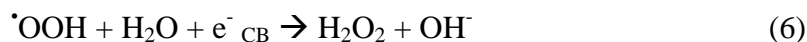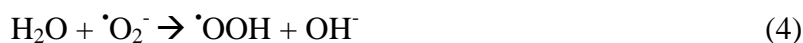
The photo catalytic study revealed that Zn(cur)O can decompose to a far extent high concentrations of perylene, fluoranthene, and chrysene faster than ZnO depending on the extent of curcumin usage during synthesis. The degradation was found to be faster for PAHs having less number of aromatic rings, particularly, it was exceptional for flouranthene degradation; 93% removal (7% remaining) of 11.4 µg/L fluoranthene with 167 mg/L Zn(cur)O loading after 10 minutes was achieved.

With a very low material loading (43 ppb), the Zn(cur)O nanostructures removed the As(III) contamination below the MCL from 100 ppb samples within 30 minutes, and almost to zero within 3 hours. Bare ZnO didn't bring down the arsenic contamination below its MCL even after 3 hours. The compound reached up to 75% removal/adsorption capacity with 903 ppb concentrations after 3 hours with the same loading, which reflects the excellent capacity of removal for such a high arsenic concentration. Kinetics of adsorption fitted very well to pseudo second order model

with exceptional adsorption rates that reflected the high affinity of the compound to As(III). Fluorescence sensing of arsenic for concentrations from 1 to 100 ppm was successful by Zn(cur)O, however, the fluorescence response started saturating after 3000 ppb of As.

# CHAPTER IV
## TUNING GOLD NANORODS SYNTHESIS THROUGH PRE-REDUCTION WITH CURCUMIN

**A. Experimental**

*1. Materials*

Gold (III) chloride hydrate (99.999% trace metal basis) was obtained from Aldrich. Hexadecyltrimethyl-ammonium bromide (CTAB) (Acros Organics). Ascorbic acid (Fluka). Curcumin (Sigma). Trisodium citrate dehydrate and silver nitrate were obtained from Sigma-Aldrich. Sodium borohydride was obtained from Acros Organics. DMSO was obtained from Merck and absolute ethanol from Sigma-Aldrich. All these chemicals were used directly without further purification. Stock solutions were prepared in de-ionized water unless otherwise indicated.

**2. Synthesis**

*a. Synthesis of gold nanorods from Citrate capped gold seeds (Procedure A)*

In a typical experiment, 2.5 mL of a 0.01M $H[AuCl_4].3H_2O$ solution and 3.6445 g (CTAB) were replenished in a 100 mL volumetric glass flask. For completely dissolving the CTAB powder, it was necessary to keep this solution at elevated temperature (33∘C) for at least 2 hours. This solution, which contained 0.1M CTAB and $2.5 \times 10^{-4}$ M $H[AuCl_4].3H_2O$, was used as *growth solution*. During the dissolution of the CTAB in the above growth solution, a *seed solution* containing small gold particles was prepared as follows: a volume of 0.5mL of 0.01M $H[AuCl_4].3H_2O$ solution ($5\times 10^{-6}$ mol, volumetric glass flask, not cooled) was added to 18.4mL of ice-cooled deionized

water in a wide-necked PE-flask (PE = Poly-Ethylene).Thereafter, 0.5 mL of freshly prepared 0.01M sodium citrate solution ($5 \times 10^{-6}$ mol, solution in a volumetric glass flask, not cooled) was added. Thereafter, immediately 0.6 mL of freshly prepared 0.1M $NaBH_4$ solution (in a glass vessel) cooled in an ice-bath was added, and the resulting solution was stirred for 30s. The solution turned red (after 24 h, particles of ~ 8nm formed). For the following final reaction steps, cooling was not required. 80 μL of a freshly prepared 0.1M curcumin solution ($8.0 \times 10^{-6}$ mol) was added without stirring to 14.4mL of the growth solution (age between 2 h and 24 h, containing $3.6 \times 10^{-6}$ mol gold). The solution was mixed by shaking, whereupon the solution became brighter yellow. After addition of 16 μL of seed solution (age between 2 h and 24 h, containing $4.0 \times 10^{-9}$ mol gold), the solution was mixed by shaking and became brownish. Then the test tubes were placed in a water bath at 33∘C overnight and then stored in a refrigerator (temperature ≈ 6∘C) to precipitate a major fraction of CTAB. Samples were withdrawn from the bottom precipitate and centrifuged at low speeds to separate the rods from the spheres. However, this method wasn't very efficient in separation. The same procedure was done except the growth solution containing the curcumin was adjusted pH to 9.2-9.6. Normally the solution pH is ~5.

### b. Synthesis of gold nanorods from CTAB capped gold seeds (Procedure B)

The gold nanoparticle seeds were prepared as follows [212]: 250 μL of a 10.0 mM aqueous $HAuCl_4$ solution was added to a plastic conical centrifuge tube. To this, 7.50 mL of a 100 mM aqueous CTAB solution was added. The mixture of these reagents changed the solution color from bright yellow to deep orange. To this, 600 μL of a freshly prepared, ice-cold 10.0 mM $NaBH_4$ solution was added, which immediately

changed the solution color to pale brown. The reaction was then left undisturbed for

~3.0 h to ensure complete $Au^{3+}$ reduction; however, the seeds were used within 2-4

hours after synthesis. After seed generation, Au nanorods were prepared in a 25.0 mL

scale. For this, 23.75 mL of 100 mM CTAB was mixed with 1.0 mL of 10.0 mM

$HauCl_4$ in a conical centrifuge tube. To this, 150 µL of 10.0 mM $AgNO_3$ and 160 µL of

100 mM curcumin (in ethanol) were added. All of these solutions were freshly prepared,

added to the reaction in the listed order, and the system was mixed by inversion after the

addition of each solution. Finally, 105 µL of the Au seed solution was added followed

by gentle mixing, after which the reaction was left undisturbed for at least 3.0 h at 25.0

°C before use. Washings were done with 1-2 mM CTAB as they preserve the nanorods.

When changing the initial concentrations of reactants one at a time, we slightly changed

the way we prepare CTAB capped gold seeds for the sake of comparison with literature.

It was prepared as following [213]: Typically, a 10 mL solution of Au seeds was

prepared by the reduction of $HAuCl_4.3H_2O$ ($2.5 \times 10^{-4}$ M) by ice-cold $NaBH_4$ ($6.0 \times 10^{-4}$

M) in the presence of (CTAB, $7.5 \times 10^{-2}$ M). The $NaBH_4$ solution was added at a time to

the solution containing CTAB and $HAuCl_4$ and the reaction mixture was then shaken

(or magnetically stirred) for two minutes allowing the escape of the gas formed during

the reaction. These seeds were 4 nm or smaller in diameter. The citrate capped gold

seeds were prepared as above.

### c. Synthesis of curcumin conjugated of gold nanoparticles

We wanted to investigate whether curcumin-capped seed solution would serve

to yield nanorods where these seeds had an average size of 18 nm (as confirmed by

HRTEM studies[214]), which are almost 5 times larger than CTAB capped gold NPs. This solution was designated as S(I) and was used as the seed solution in samples 1@S(I), @S(I), and 3@S(I).

To prepare curcumin conjugated gold NPs [214], the following stocks were prepared in deionized water; 10 mM H[AuCl$_4$].3H$_2$O and 150 mM K$_2$CO$_3$. A stock solution of 100 mM curcumin in 99.8% DMSO was also prepared. Initially, **5** ml of 0.25 mM curcumin solution was adjusted using K$_2$CO$_3$ to pH = 9.2 -9.6. Within 2 minutes of adjusting curcumin pH, 5 ml of 1 mM H[AuCl$_4$].3H$_2$O solution was added drop wise with simultaneous shaking to curcumin solution. The solution turns from red to light brownish orange then darkens to burgundy red. The samples were kept undisturbed at room temperature for 3 days after which they were centrifuged at 10,000 rpm for 15 minutes for analysis.

## 3. Characterization

The instruments used were as given previously in Chapter 2.

## B. Results and discussion

### 1. Gold nanorods prepared from citrate capped Au seeds

Gold nanorods were synthesized from citrate capped Au seeds using curcumin as the reducing agent as indicated in procedure A. This procedure –initially using AA as reducing agent- was adopted because it has rendered the seed mediated synthesis procedure simpler, decreased the susceptibility to impurities, and improved the reproducibility of the product distribution.

When examining the samples done in this work (using curcumin) with SEM, spherical particles of 30-60 nm were detected alongside fewer triangular particles. This's usually seen in other publications on seed-mediated growth of high aspect ratio gold nanorods. The aspect ratio distribution of nanorods was broad as seen in fig. 4.1a; high to low aspect ratio nanorods with varying lengths (100 – 800 nm) and widths (30-40). The yield was relatively low. When AA was used, nanorods of aspect ratios around 6 in the average and 10 or more at maximum were obtained [215]. In addition significant quantities of spherical (of typically 30 nm– 60nm) and, to a lesser extent, triangular particles also arose.
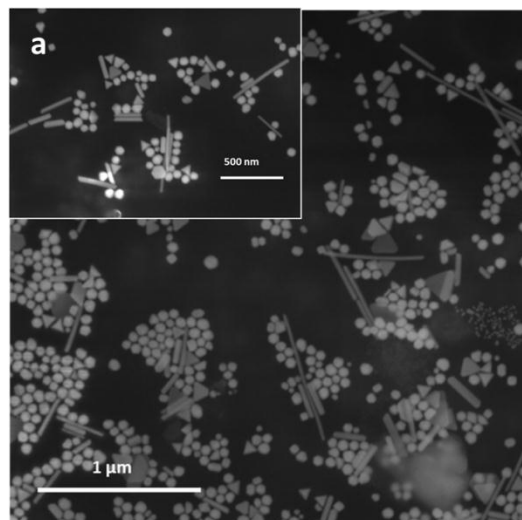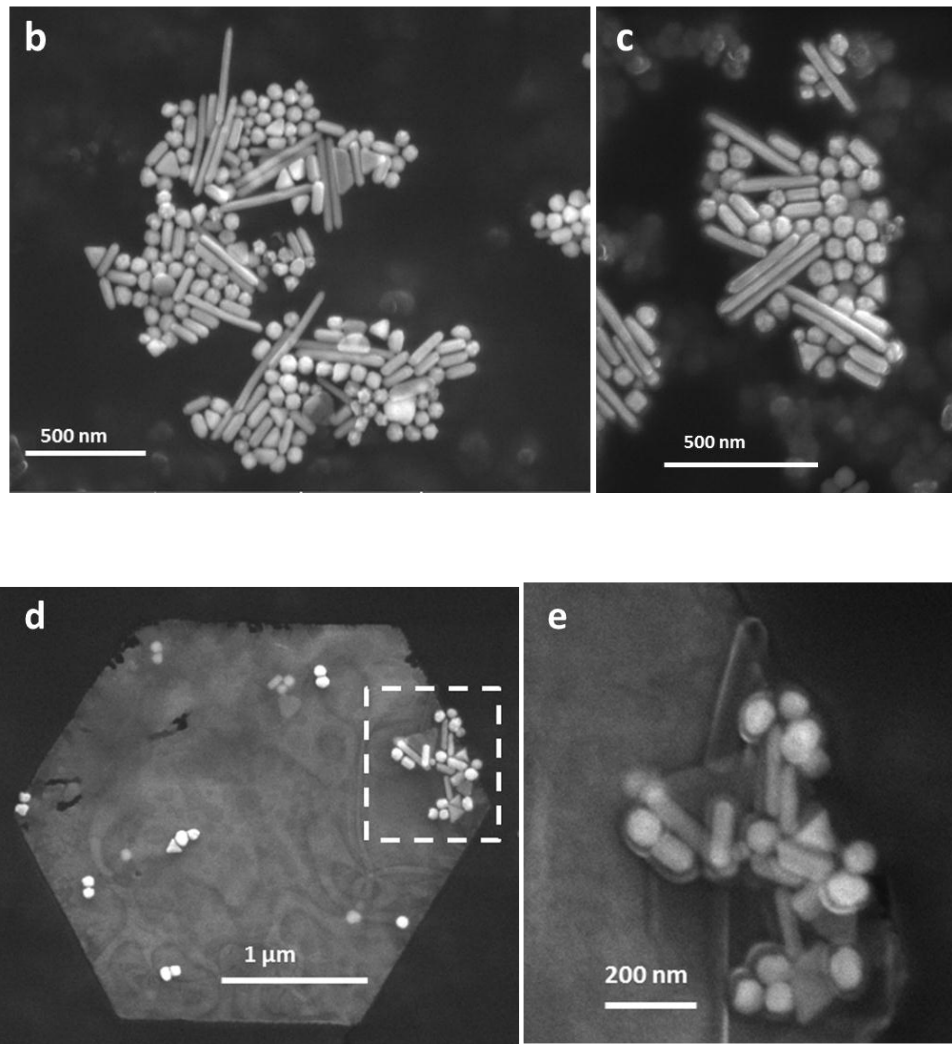
**Figure 4.1 (a-e): SEM images of gold nanorods prepared from citrate capped Au seeds (procedure A)**

A particularly interesting thing to notice in fig. 4.1 d (closer look is given in fig. 4.1 e), besides the apparent layer around the nanorods, which is the CTAB bilayer formed around, is the ghostly nanorod form so to speak. We couldn't relate this shadowy template but to the CTAB micelle formed before any gold becomes adsorbed on it. This could be a hint to the mechanism of formation of the gold nanorods. In fact, there is more than one mechanism proposed in literature.
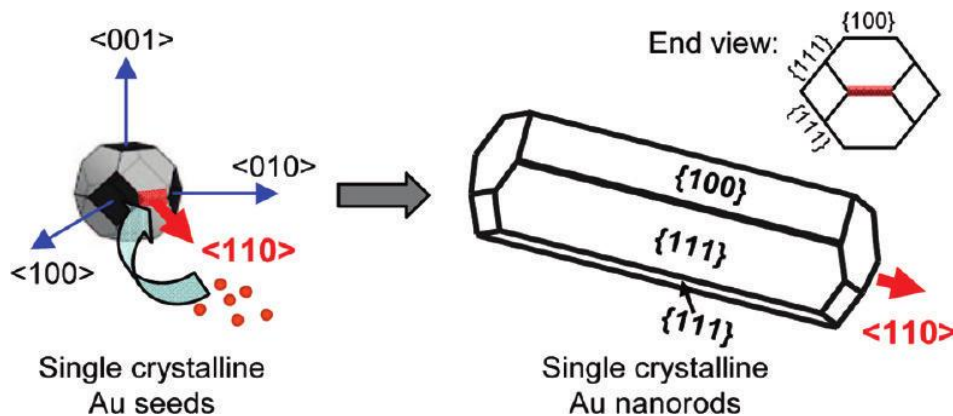
**Scheme 4.1: Structural Model of Single Crystalline Au Nanorods and Proposed Growth Mechanism[74]**

Garg and coworkers constructed a structural model (scheme 1) based on the HR-TEM results and proposed a mechanism for the seeding growth of [110] oriented, single crystalline Au nanorods[93]. The CTAB capped Au seeds are typically quasi-spherical particles (~2 nm) enclosed by low-index [111] and [100] facets; with the [111] facets possessing the lowest surface energy (hence, the most stable facet) among the three types of facets. The [110] facets have the highest surface energy and thus it's not favored that these facets be exposed; the [100] facets come in between. One of the major roles of Br- ions in the nanorod growth process is their etching interaction with the Au seeds which leads to small single crystalline, polyhedral particles at the early stage of the growth process (Scheme1). Twinned particles may be dissolved due to Br-etching. And it appeared to them that this etching process occurs much easier on smaller seeds as larger particles are more difficult to be etched by Br- to form the right type of polyhedral seeds for rod growth. Since the Au[111] and Au[100] facets are more stable than [110], it's expected that the single crystalline seeds prefer to elongate along the [110] direction to maximize[111] facets (see the red highlighted (110) facet in Scheme 1). So <110> elongation of the single crystalline seeds results in [111] and [100] side

facets (Scheme 1). As the side facets are passivated by Br-, the radial (or side) growth is retarded and further elongation along the [110] direction is facilitated. The preferred growth of [110] nanorods, as opposed to [100] or [111] nanorods, was energetically favorable according to the theoretical calculations by Barnard and Curtiss [216]. It is thought that $CTA^+$ mainly provides steric protection of the formed nanorods, but its templating role couldn't be dismissed.

Murphy et al. proposed a mechanism that fall in line with the above stated one as it suggests CTAB would bind preferentially to the Au[100] and [110] seed facets and then the thermodynamically favorable intermolecular interactions of the 16- carbon cetyl chains take action to promote surface adhesion scheme 4.2. This preferential binding regime agrees with the size of the quaternary ammonium head group relative to the larger binding sites available on the Au [100] and Au [110] faces of the crystalline rods than at the [111] face [97,114].
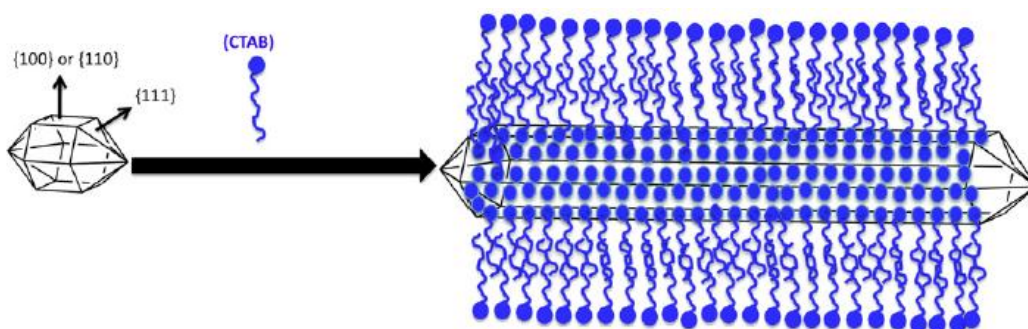


**Scheme 4.2: A cartoon that demonstrates the proposed mechanism of gold nanorod growth (in the absence of silver)[93].**

However, our result stands opposite to the above mechanisms for nanorod growth and the cylindrical CTAB micelle-templated based growth mechanism seems to

be operative rather than the preferential binding of CTAB molecules onto certain facets of developing NRs adopted when AA is used. It could be that these two mechanisms exist and one of them would take place under certain conditions. It's suggested that the presence of curcumin could have favored the cylindrical CTAB micelles growth (seen in SEM image) in some way. In fact, it has been shown that introducing certain aromatic compounds could modify (improve) the micellization behavior of CTAB surfactant[217]. This suggestion is consistent with the proposed mechanism by Liz-Marzan and coworkers that considered the CTAB micellar structure promoted the deposition of the metal at the tips of gold seed particles that are also surrounded by CTAB [218]. The mode of action proposed is that $AuCl_4^-$ ions displace $Br^-$ ions and then tightly bind to $CTA^+$ micelles. Upon addition of curcumin, $AuCl_4^-$ is reduced to $AuCl_2^-$ at the micelle surface, and the rate of growth of the different nanorod facets would be determined by the approach of the micelle, and thus gold species, toward the facets of the seed that are also covered with CTAB. Liz-Marzan et al. supported this mechanism by performing calculations for the surface potential of metal ellipsoids in 1 mM NaCl, which showed that this potential decays more rapidly at the nanorod tip than at the sides, and thus the micelle can more readily approach the tips of the rods than the sides and allow deposition of gold[93]. It is crucial, however, to have initially a twinning plane or stacking fault in the seed to cause an asymmetric electric field [97,218].

Gold nanorods give rise to two absorption bands. One of them is caused by transverse oscillations of the electrons (transverse absorption band), located in the visible wavelength region and can interfere with the absorption of spherical gold particles. The other is due to the longitudinal oscillations of the electrons (longitudinal

absorption band), shifted from the visible towards the near-infrared region with increasing aspect ratio. The longitudinal absorption band of such particles in UV-Vis-NIR spectra falls in the absorption region of water (ca. 1300 nm–above 2500 nm) and is therefore not accessible in the aqueous solutions finally resulting from the nanorod synthesis.

When AA is used, UV-Vis showed peaks in the region of 500–700nm to be "attributed to the more or less spherical particles, triangles and the transversal plasmon absorption of the nanorods and that around 1955nm to the longitudinal absorption of the nanorods" (a technique based on embedding the particles in poly(vinyl alcohol) (PVAL) was used to detect bands beyond 1000 nm [215]).

UV-Vis absorption is sensitive to the shape and aggregation state of the materials and will shift or change the position of the plasmon bands. The nanorods reduced with AA displayed two plasmon bands at 552nm for the transverse surface plasmon and 759nm for the longitudinal surface plasmon in the visible region of the spectrum as shown in fig. 4.2. The longitudinal band for nanorods reduced with curcumin didn't show clearly and the transverse band is lower in intensity than AA reduced-Au NRs due to probably loss of material during decanting. It also shows an additional peak at ~ 404 nm attributed to curcumin absorption. The longitudinal band might be located beyond 1000 nm.
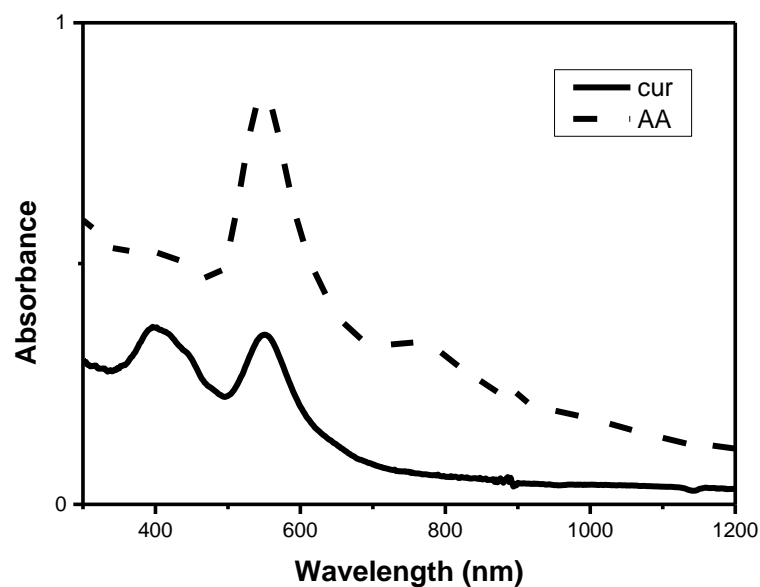
**Figure 4.2: Comparison of UV-Vis of Au NRs prepared from Citrate capped Au seeds reduced with curcumin (Cur) and Ascorbic acid (AA) (procedure A)**

a. Effect of pH

The slow reduction of gold is crucial for nanorod formation and mild reducing agents are used for this purpose. As a confirmation, we increased the reducing ability of curcumin by adjusting the pH to its pka value (~9.3-9.6). As expected, no nanorods were observed and much smaller spherical particles (see Fig. 4.3) appeared as further confirmed by the blue shift in the UV-Vis spectrum (band at 505 nm, see fig. 4.4).
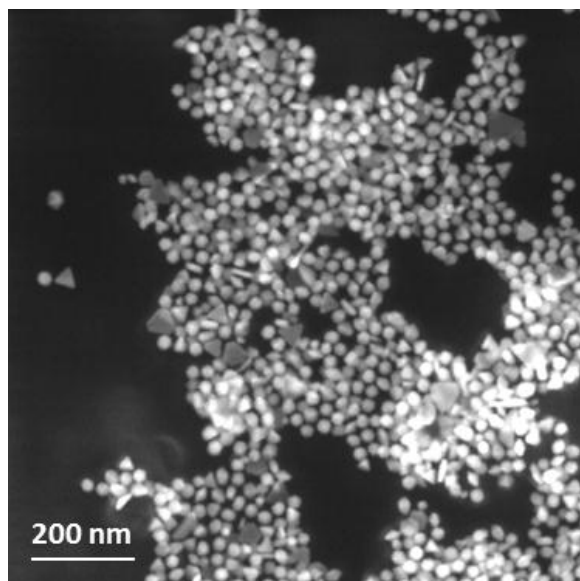
**Figure 4.3: SEM image of gold nanorods from citrate capped Au seeds (procedure A), pH of growth solution adjusted to ~ 9.3**
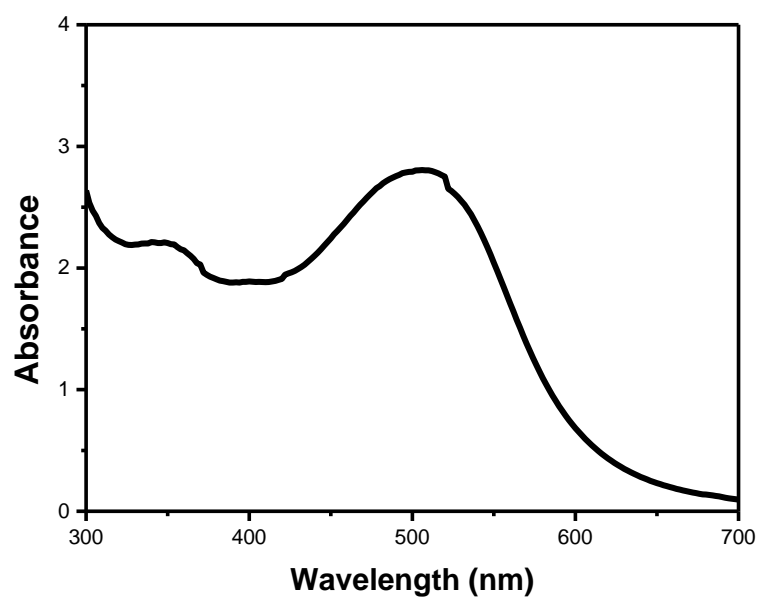


**Figure 4.4: UV-Vis of gold nanorods from citrate capped Au seed; pH of growth solution containing curcumin was adjusted to 9.3**

b. Effect of seed concentration

**Table 4.1: Concentrations of reactants in growth solutions differing in seed concentration**

|  | [CTAB] mM | [Au]$_{seed}$ $10^{-7}$ M | [Au$^{3+}$] mM | [curcumin] mM |
|---|---|---|---|---|
| 1s | 100 | 2.76 | 0.25 | 0.533 |
| 2s | 100 | 2 | 0.25 | 0.533 |
| 3s | 100 | 1 | 0.25 | 0.533 |

Previous results using ascorbic acid didn't provide a definite trend for increasing the seed concentration. Typically, increasing the seed concentration resulted in a decrease in AR of NRs. However, the results of some reports were in contrary to expectations where AR increased upon increasing the amount of seed. In our case, when we decreased the seed concentration from $2.76 \times 10^{-7}$ M (in sample 1s) to $2 \times 10^{-7}$ M (in sample 2s), there was an increase in the AR and yield of NRs, however, further decreasing to $1 \times 10^{-7}$ M reversed the outcome seen in fig. 4.5. There is no clear trend of NR formation with the seed concentration at least in our case. The UV-Vis spectra of the samples is in agreement with what is seen in SEM images. The thinnest NRs observed in fig. 4.6 has the transverse PB blue-shifted while the thicker NRs of the other samples lie at higher wavelengths.
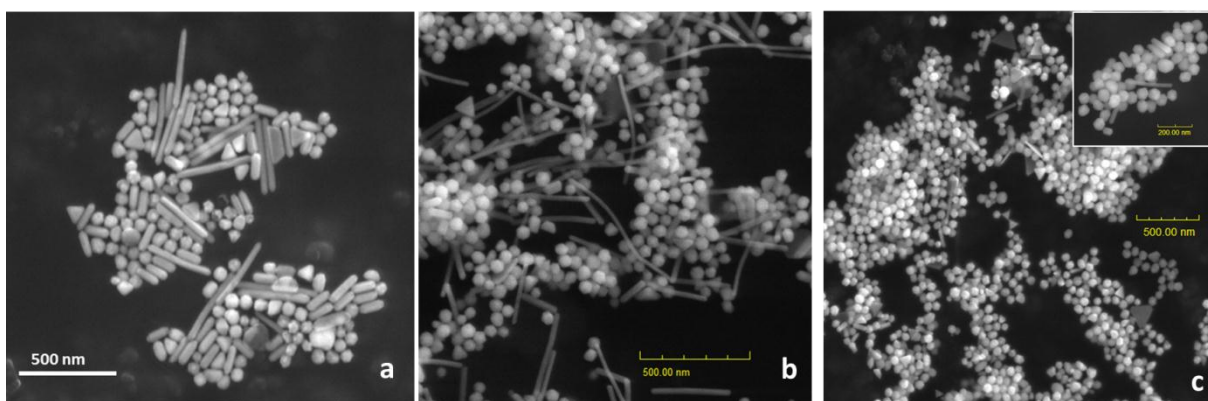
**Figure 4.5: SEM images of samples (a)1s (b)2s (c) 3s**
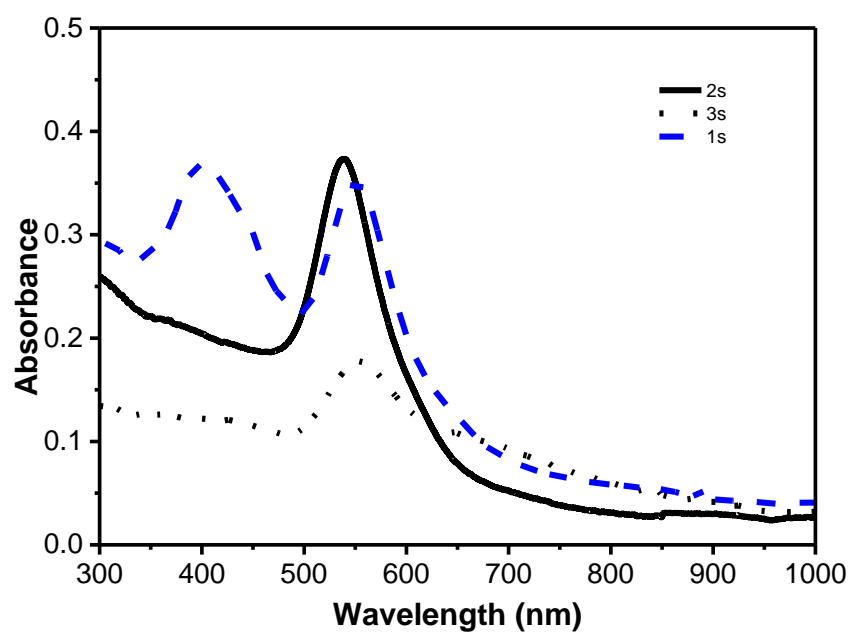


**Figure 4.6: UV-Vis spectra of samples 1s, 2s, and 3s**

c. Effect of curcumin concentration

Sample 1cur shows high AR gold NRs and spherical NPs (20-30 nm) (fig. 4.7 a). Upon doubling the curcumin concentration in sample 2cur (fig 4.7 b), we notice a tremendous decreasein AR in accordance to what is seen in literature. Furthur increasing curcumin by 5 folds (sample 3cur, fig. 4.7 h)results in larger spherical particles (50 – 70 nm).

**Table 4.2: Concentrations of reactants in growth solutions differing in curcumin concentration**

|  | [CTAB] mM | [Au]$_{seed}$ $10^{-7}$M | [Au$^{3+}$] mM | [curcumin] mM |
|---|---|---|---|---|
| 1cur | 100 | 2 | 0.25 | 0.533 |
| 2cur | 100 | 2 | 0.25 | 1.067 |
| 3cur | 100 | 2 | 0.25 | 5.330 |
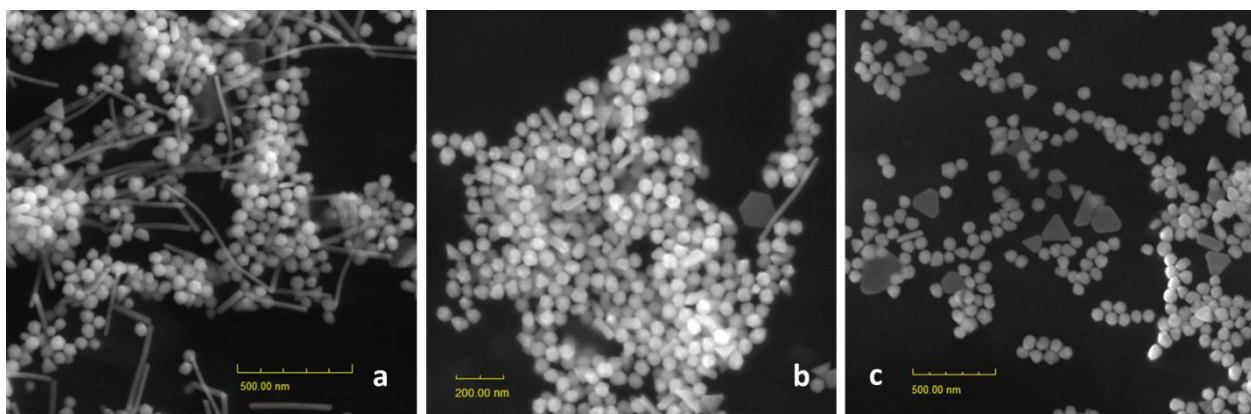


**Figure 4.7: SEM images of (a)1cur and (b)2cur and (c) 3cur**
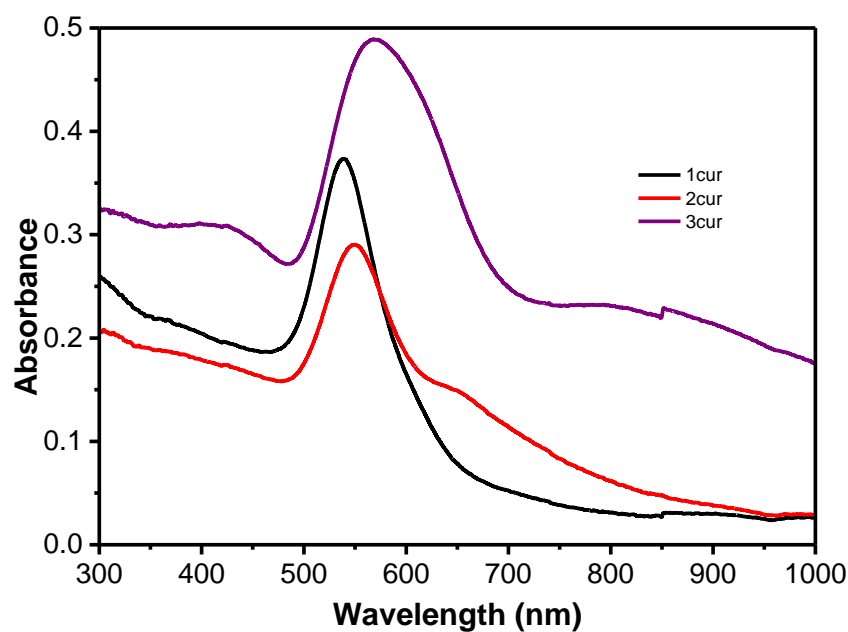
**Figure 4.8: UV-Vis spectra of samples 1cur, 2cur, and 3cur**

Peaks in the region of 500–700nm correspond to the more or less spherical particles, triangles and the transversal plasmon absorption of the nanorods. So shoulders or broad bands seen in the spectra are basically attributed to the minority shapes present in the sample. Spcifically, shoulders at 656 nm and 795 nm for samples 2cur and 3cur respectively are attributed to the triangular shapes observed more clearly in the sample containing the highest curcumin concentration (fig. 4.8). The band at 537 nm for 1cur is red shifted to 549 nm and 568 nm respectively for higher [cur] indicating spherical size increase. As the concentration of curcumin is increasing, there is a faster supply of gold to the seeds resulting in shorter rods and larger spheres and triangles (morphological change). Similar observations have been reported for ascorbic acid[112].

89
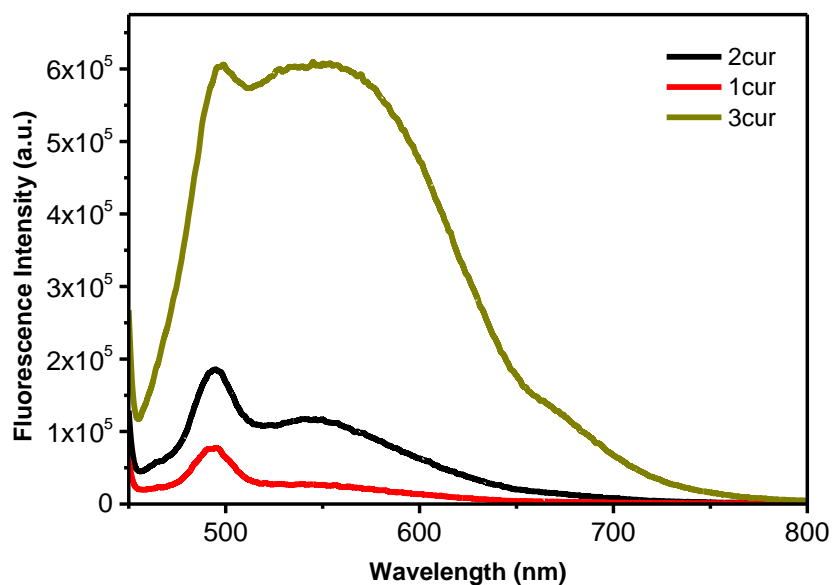
**Figure 4.9 Photoluminescence (emission) spectra of 1cur, 2 cur and 3cur at excitation wavelength 425 nm**

The photoluminescence spectra of 1cur, 2cur and 3cur at excitation wavelength 425 nm are sown in Fig 4.9. All of them gave an emission maximum around 550 nm and another band around 670 nm. The maximum around 550 nm is due to curcumin conjugated gold nanoparticles that includes nanorods, triangles etc. shapes whereas the emission at around 670 nm is due to gold particles/nanorods (triangles etc.). The fluorescence intensity at around 550 nm provided interesting information, as the curcumin concentration increased to 2 fold (for 2cur) and subsequently 10 fold (for 3cur) the fluorescence intensity similarly enhanced roughly in the same order. This indicates amount of curcumin conjugated to gold particles depends on the curcumin concentration. As more curcumin is present in the solution, the attachment of curcumin per gold nanoparticles increases where it doesn't necessarily transfer into gold nanorods solely. In other words increase in curcumin concentration per gold discourages formation of gold nanorods.

90

It's noted that adding $AgNO_3$ would increase the nanorod yield but would at the same time decrease the aspect ratio of the rods (aspect ratio achievable is typically <6 versus ~25 without $AgNO_3$)[97]. However, there's a critical $[Ag^+]$, above which the aspect ratio of the nanorods decreases again [79]. In fact, silver also affects the growth mechanism, the crystal structure of nanorods, and the results of varying different parameters. As the addition of silver into the growth solution is thought to alter the chemistry at the interface of the growing particle and the growth solution, it is convenient to differentiate seed-mediated approaches performed in the absence and in the presence of silver. Silver was added at different concentrations in an attempt to understand its effect. We expected a raise in the yield of nanorods; however, this addition caused the total disappearance of rods at high Ag concentrations (2A-4A) (fig. 4.10). At low concentration (1A), few nanorods appeared much less than the silverless procedure (fig. 4.10d). Although the silver concentrations used are similar and even lower than those used in literature, it seems the critical $[Ag^+]$ when curcumin is used is much below the concentrations used or it might be due to an interaction of curcumin with silver. No trace of silver was detected in EDX (fig. 4.11) which goes along the assumption that silver maybe directly interacting with curcumin instead of assisting in gold nanorod formation. Since this interaction affects the nanorod growth, it's expected to result in smaller spherical particles as seen in SEM images and in the blue shift of the Surface Plasmon Band (SPB) (fig. 4.12).

**Table 4.3: Concentrations of reactants in growth solutions differing in silver content**

|  | [CTAB] mM | [Au] $_{seed}$ $10^{-7}$ M | [Au $^{3+}$] mM | [AgNO$_3$] $10^{-5}$ M | [curcumin] mM |
|---|---|---|---|---|---|
| 1A | 100 | 2 | 0.25 | 0.16 | 0.53 |
| 2A | 100 | 2.76 | 0.25 | 1.4 | 0.53 |
| 3A | 100 | 2 | 0.25 | 1.6 | 0.53 |
| 4A | 100 | 2.76 | 0.25 | 2.7 | 0.53 |
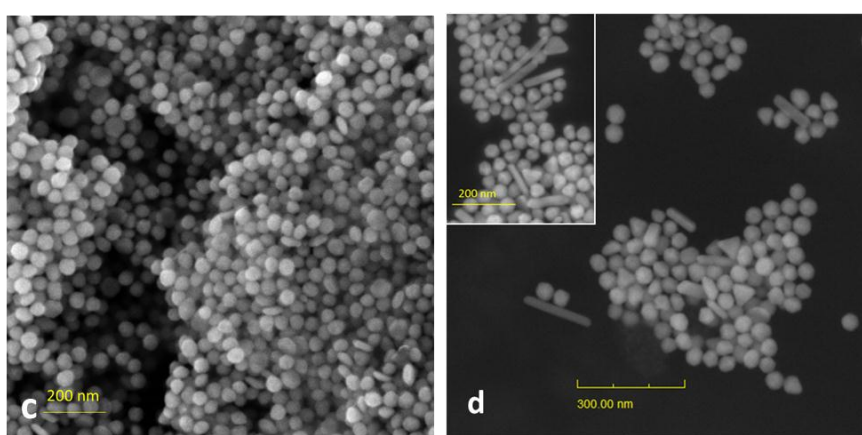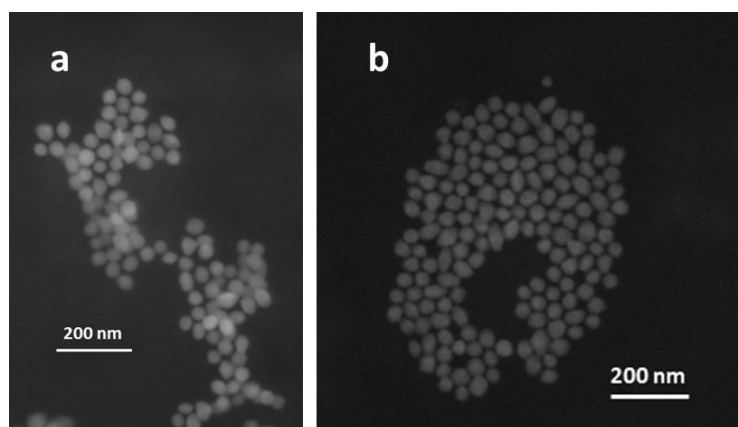


**Figure 4.10: SEM images of (a) 2A (b) 4A (c) 3A (d) 1A**
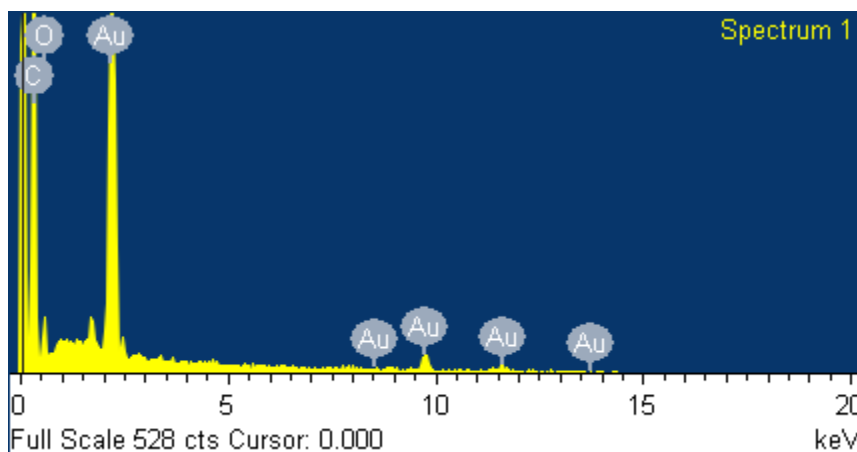
**Figure 4.11: EDX of gold nanoparticles made from citrate capped gold nanoparticles in presence of silver.**

In the UV-Vis spectrum (fig. 4.12), all the samples exhibited a band around 540 nm and only 1A showed LSPB at around 983 nm since the rods are shorter than the silverless procedure. The bands seen at around 405 nm is due to curcumin left after washing. Except a change in fluorescence intensity, the fluorescence spectra shown in Fig. 4.13 did not show any difference in the spectral shape at low (with Au nanorod formation, 1A) and high (without Au nanorod formation, 3A) concentration of silver (10 fold increase). The band at around 670 nm was not clear due to low intensity in this region. The increase in fluorescence intensity suggests that reduction in formation of nanorods increases possibility of smaller nanospheres formation that increases the overall surface area, thus, reflecting higher curcumin conjugation with gold.
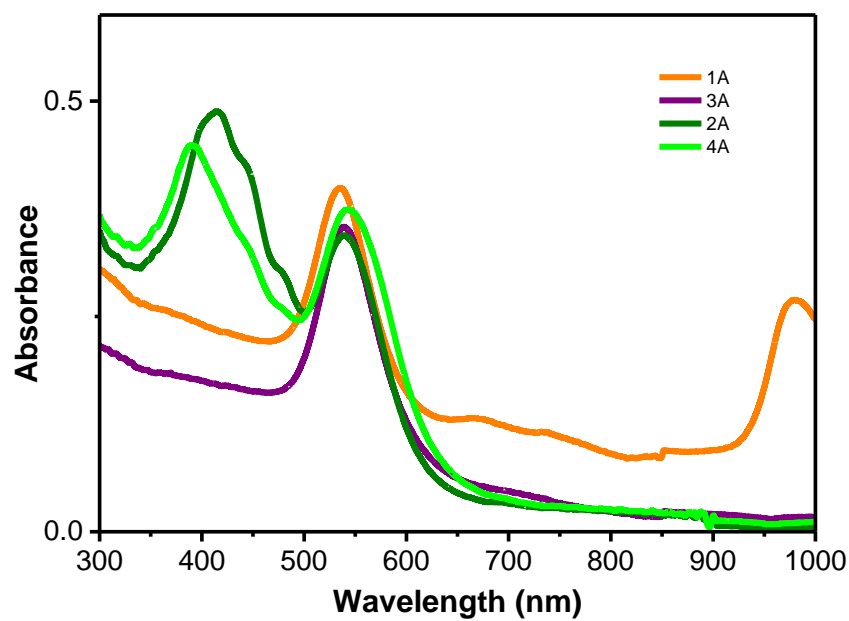
**Figure 4.12: UV-Vis of Au NPs from citrate capped Au seeds (procedure A) in presence of different silver content**
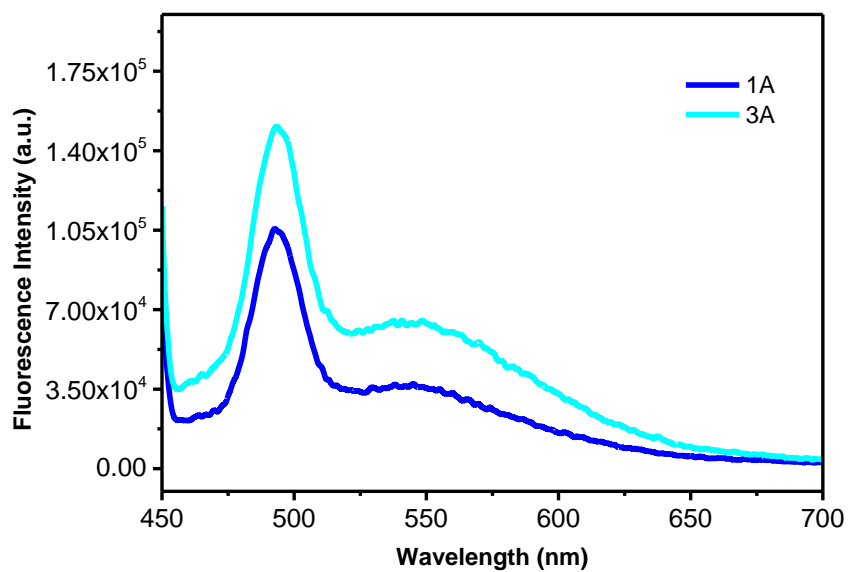


**Figure 4.13: Photoluminescence (emission) spectra of 1A and 3A at excitation wavelength 425 nm**

## 2. Gold nanorods prepared from CTAB capped Au seeds

Gold nanorods were synthesized from CTAB capped Au seeds (fig. S2) using curcumin as the reducing agent as indicated in procedure B. Interestingly, much higher aspect ratio nanorods were obtained when curcumin was used as the reducing agent compared to ascorbic acid (AR ~3)[212]. The average length, width, and aspect ratio of the nanorods were determined by counting the nanostructures in several images. Nanorods of ~30 nm by 410 nm were obtained (~30% yield) (fig. 4.14). The average length, width, and AR of the nanorods are 410 nm (spanning from 118 nm to 848 nm), 30 nm (in the range 17nm-44 nm), and 15 respectively (from 3 to 32). Spherical particles of ~ 60 nm made up the majority of the nanostructures.
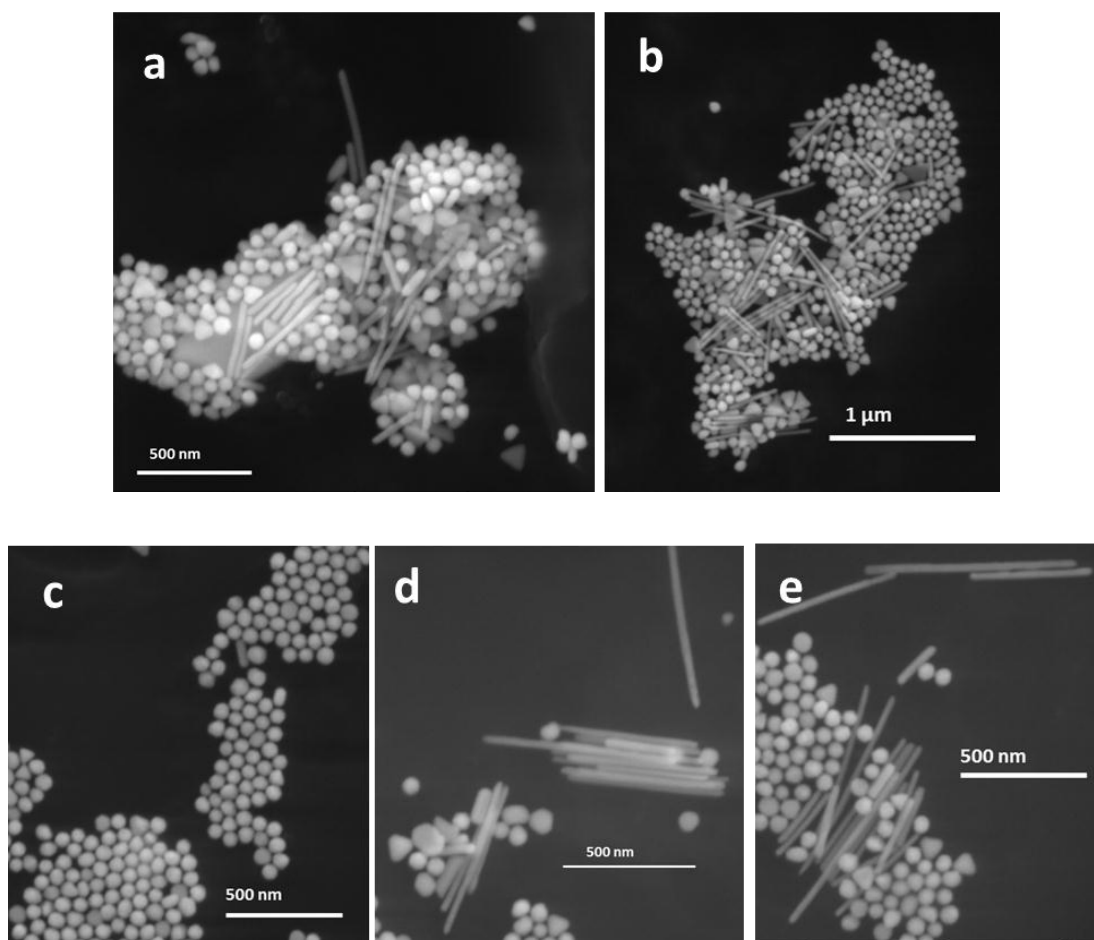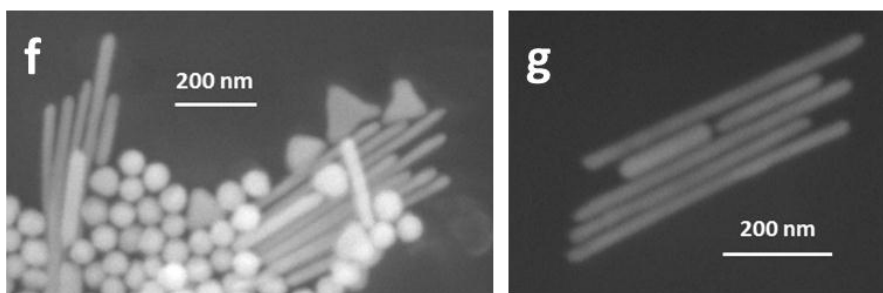
**Figure 4.14 (a-g): SEM images of gold nanorods prepared from CTAB capped Au seeds (procedure B)**

The gold NRs reduced with curcumin display a transverse PB around 550 nm that probably is also attributed to the spherical particles (see fig. 4.15). Having obtained a higher AR, the longitudinal band would appear in the IR region.
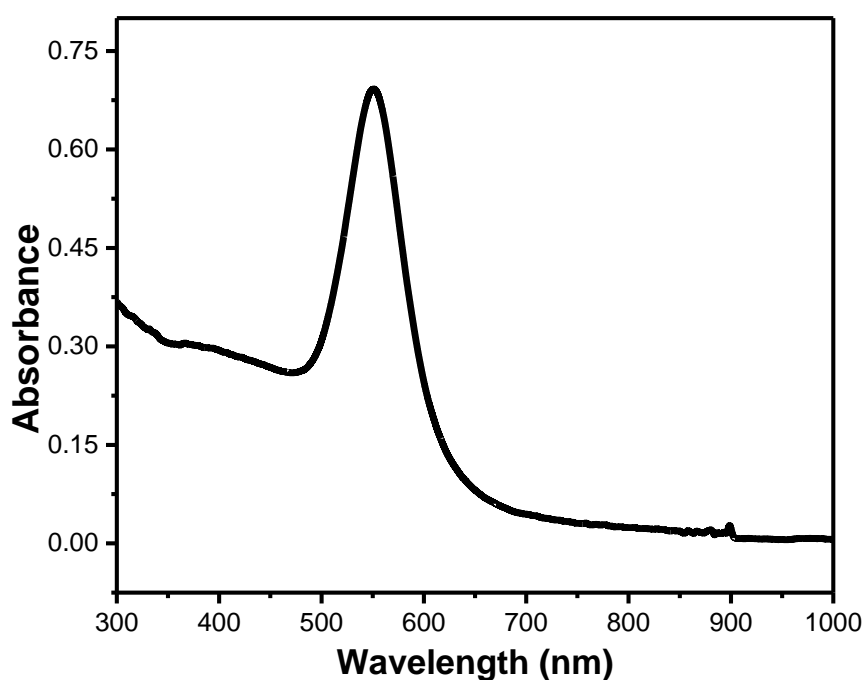


**Figure 4.15: UV-Vis spectrum of gold nanorods prepared from CTAB capped Au seeds (procedure B)**

In an attempt to increase the AR of nanorods obtained in sample 11s, we increased the seed concentrations in 22s and 33s by 10 and 100 times respectively; however, we couldn't notice any noteworthy changes in the SEM images (fig. 4.16). Also no significant change was detected in the UV-Vis spectra in terms of the SPB (fig. 4.17).

**Table 4.4: Concentrations of reactants in growth solutions differing in seed concentration**

|  | [CTAB] mM | [Au]$_{seed}$ $10^{-7}$ M | [Au$^{3+}$] mM | [curumin] mM |
|---|---|---|---|---|
| 11s | 16 | 0.125 | 0.2 | 3 |
| 22s | 16 | 0.25 | 0.2 | 3 |
| 33s | 16 | 2.50 | 0.2 | 3 |
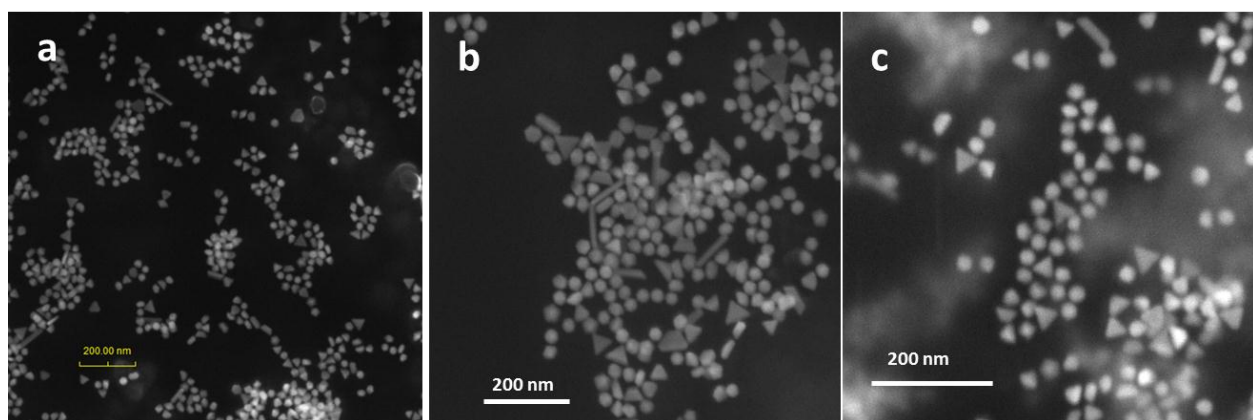


**Figure 4.16: SEM images of (a) 11s (b) 22s (c) 33s**
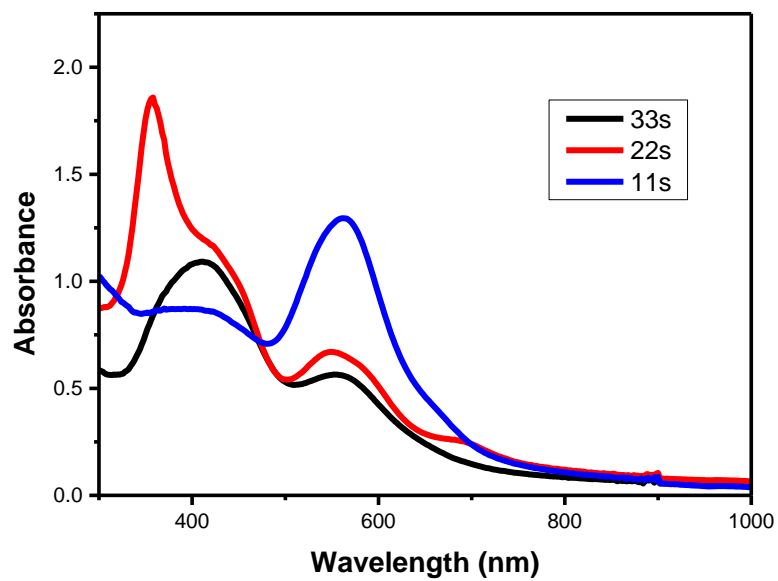
**Figure 4.17: UV-Vis spectra of gold nanorods differing in their seed concentration**
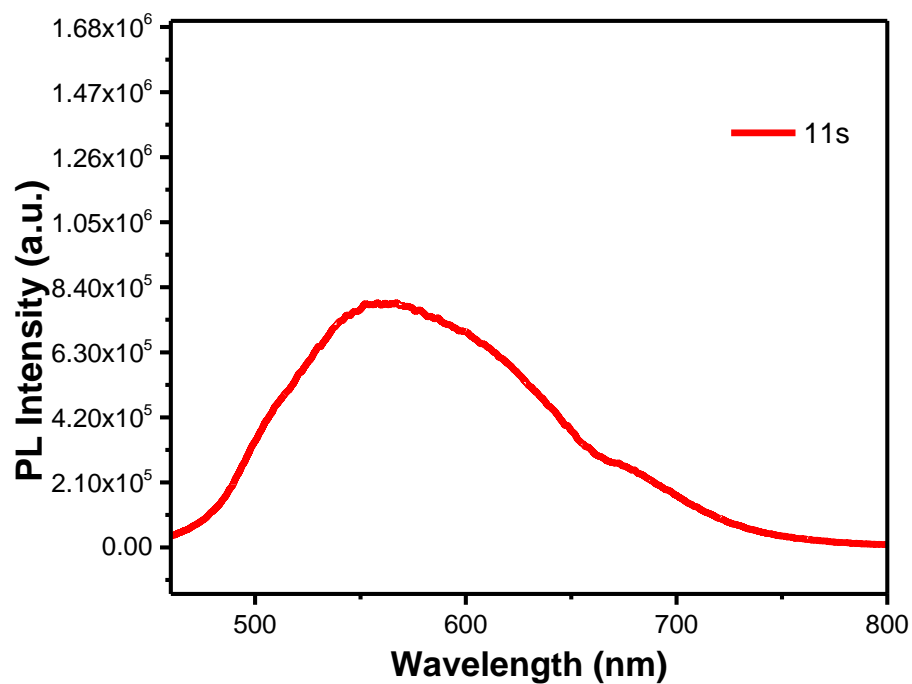


**Figure 4.18: Photoluminescence (emission) spectra of 11s at excitation wavelength 425 nm**

The photoluminescence spectra of 11s at excitation wavelength 425 nm is sown in Fig. 4.18, as expected emission maximum around 550 nm for curcumin conjugated gold nanoparticles and another band around 670 nm due to gold nanorods/nanoparticles were obtained. To further confirm that the fluorescence at longer wavelength band (above 670 nm) is due to gold nanorods/nanospeheres, excitation spectra of nanorods/nanosparticles were recorded at emission wavelength 610 nm. As depicted in Fig. 4.19, the excitation spectrum showed two maximum, one at around 425 nm corresponding to curcumin (coming from curcumin conjugated nanorod) and other at around 540 nm conforming the absorption of gold nanorods/nanospeheres (compare with Fig 4.17).
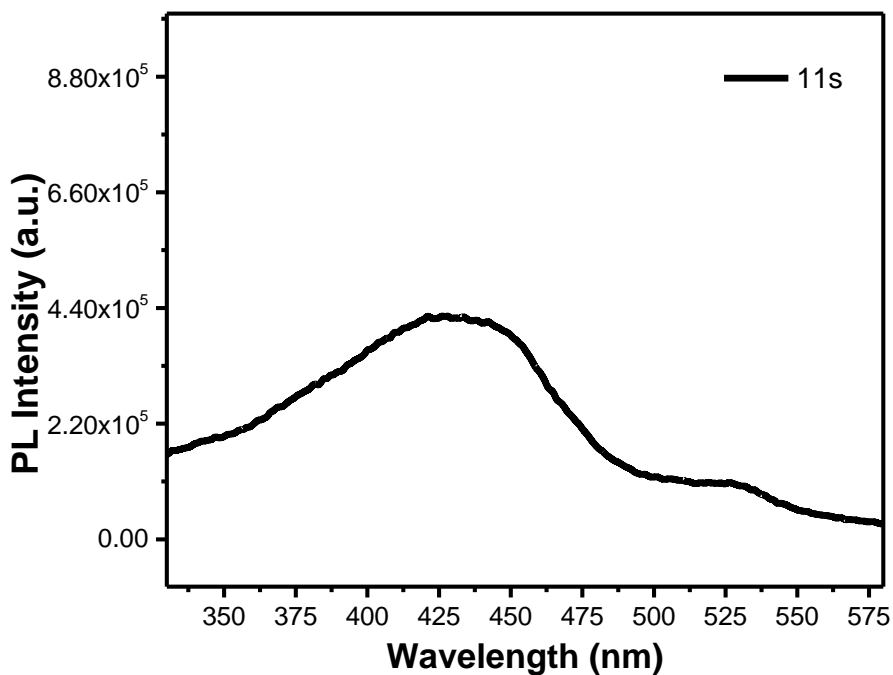


**Figure 4.19: Excitation spectra of 11s at emission wavelength 610 nm**

b. Effect of curcumin concentration

   Sample 11cur (fig 4.20 a) seemed to constitute almost all shapes from hexagons,
pentagons (see inset of fig. 4.20a) and triangles, to spheres (~25 nm) and rods which is
translated in the shoulders seen for the sample's UV-Vis spectrum in fig. 4.21 at 620 nm
and 644 nm. Spherical particles made up the bulk of the sample (band seen at 540nm).
The SEM image suggests that hexagons originate from triangles that seem to be
chopped at their vertices. Intermediate structures that look like rectangular
parallelograms under SEM (notice the ends of the nanorods) are noticed and seems to
originate from triangles. Upon decreasing the curcumin's concentration to half in
sample 22cur (Fig 4.20b), we only notice that triangles appear smaller by almost half
their size in sample 11cur. The fluorescence excitation and emission spectra further
confirmed presence of curcumin conjugation and formation of gold nanoparticles (see
Fig. 4.22 and 4.23).

**Table 4.5 Concentrations of reactants in growth solutions differing in curcumin concentration**

|  | [CTAB] mM | $[Au]_{seed}$ $10^{-7}$ M | $[Au^{3+}]$ mM | [curcumin] mM |
|---|---|---|---|---|
| 11cur | 16 | 0.125 | 0.2 | 6 |
| 22cur | 16 | 0.125 | 0.2 | 3 |
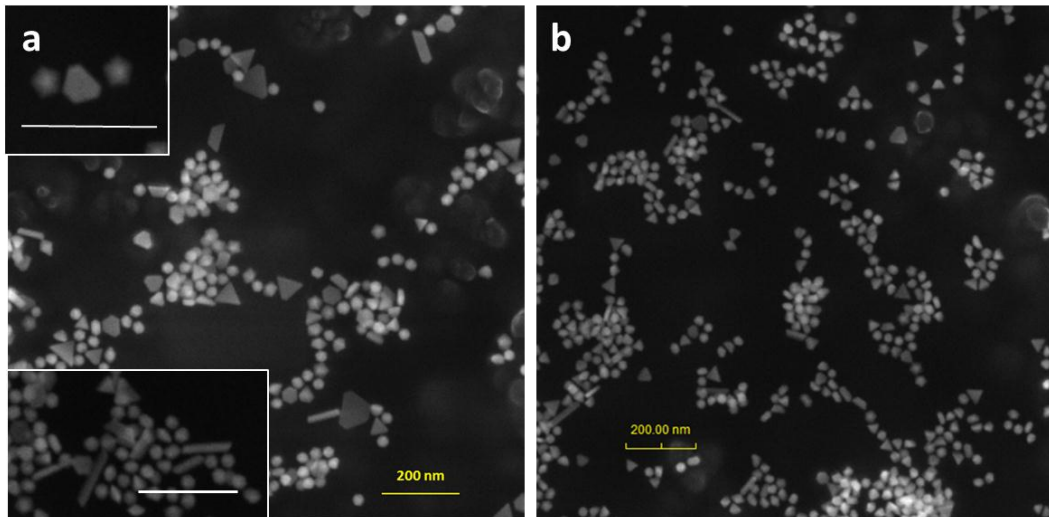
**Figure 4.20: SEM images of samples (a) 11cur and (b) 22cur**
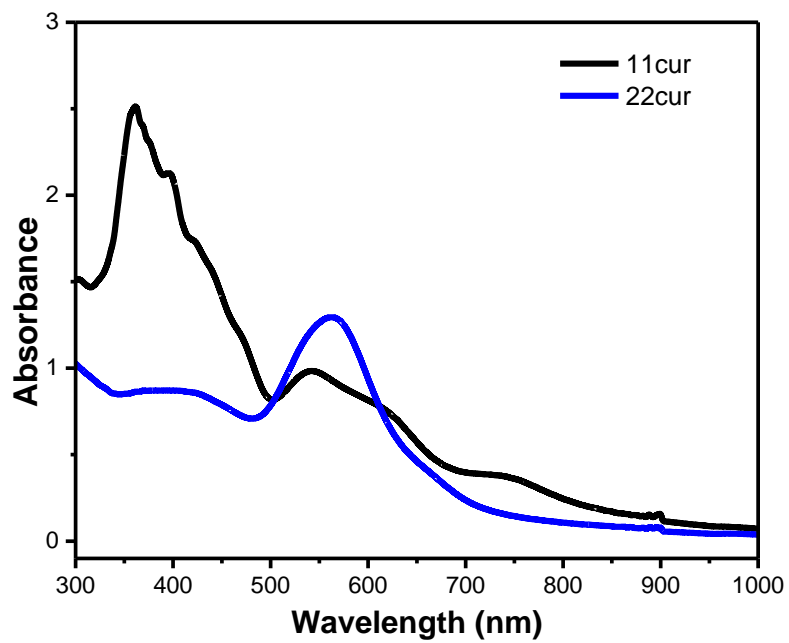


**Figure 4.21: UV-Vis spectra of gold nanorods differing in the curcumin concentration**
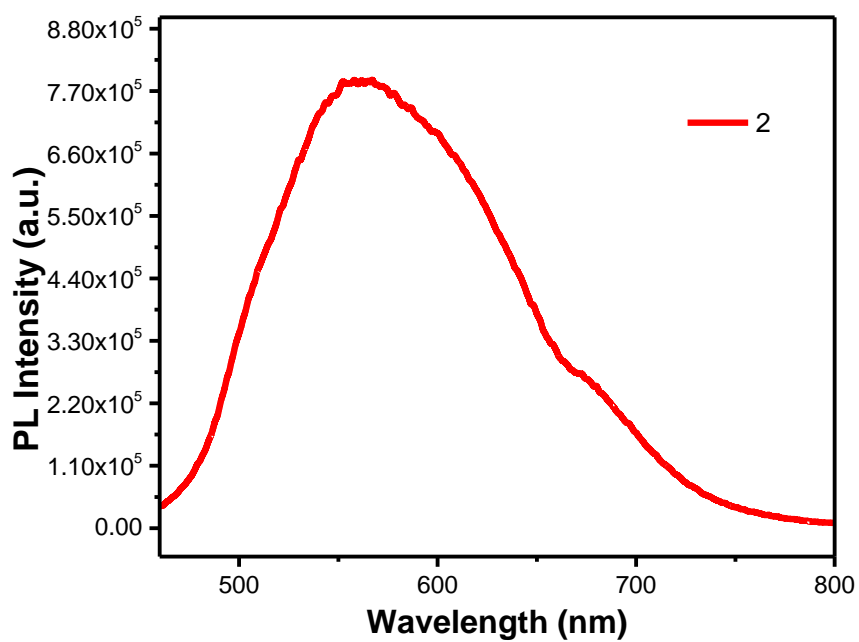
**Figure 4.22: Photoluminescence (emission) spectra of 22cur at excitation wavelength 425 nm**
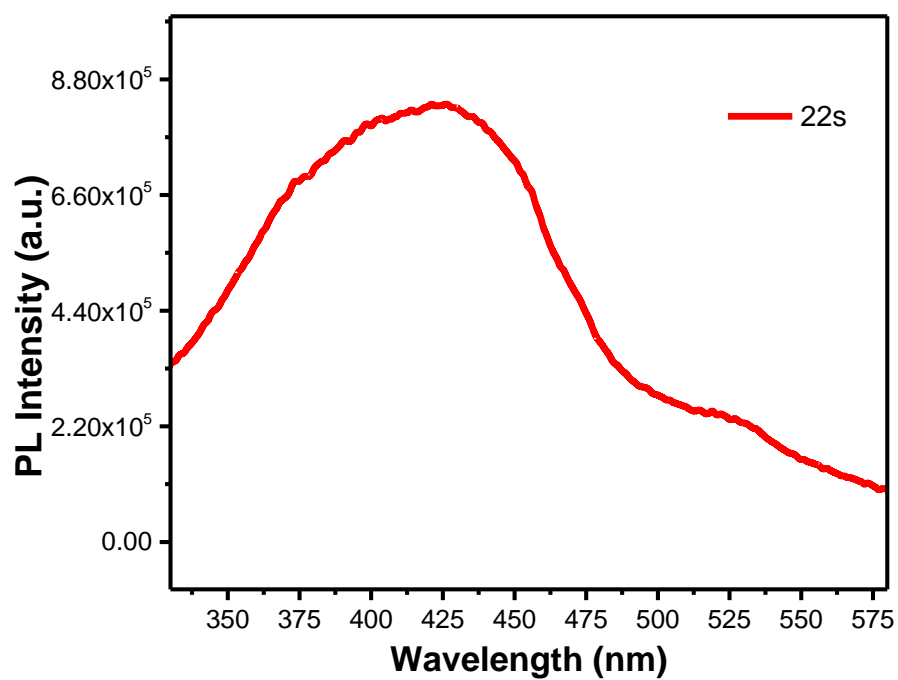


**Figure 4.23: Excitation spectra of 22cur at emission wavelength 610 nm**

It should be recalled that when silver was used in procedure A where we used citrate capped Au seeds, no nanorods were obtained. However, when CTAB capped Au seeds were used in procedure B, gold nanorods were obtained that were even better than procedure A without silver. This suggests curcumin may not be able to interact directly with the silver ion (thus not able to reduce involvement of silver in nanorods formation) in the presence of CTAB-capped gold seed. This can be explained based on the proposed mechanism by Nikoobakht and El-Sayed who considered the silver ions located between the head groups of the capping surfactant (CTAB) as Ag–Br pairs. This would lead to the decrease of the charge density on the bromide ions and consequently the repulsion between neighboring head-groups on the gold surface and results in CTAB template elongation [79].The growth solution contains gold and silver ions, and when curcumin is added only gold ions are reduced because silver ions and curcumin can't come close to each other due to the favorable hydrophobic interaction between the alkyl chain of the CTAB molecule[219] and curcumin and the unfavorable interaction between silver ion and surfactant (the silver will be present near to the Stern layer). Furthermore, Guyot-Sionnest and coworkers proposed that, during seed-mediated synthesis, underpotential deposition (UPD) of silver preferentially occurs on the [110] gold facets compared to the [111] and [100] facets leading to nanorod growth in the [100] direction[111].  As the silver monolayer will cover the [110] facet, and, although the silver may be oxidized and replaced by gold, other facets will grow faster because they are less covered with silver (scheme 3). Therefor differing degrees of silver passivation on the [110] facets lead to varying ratios of growth on this facet and the nanorod's end facets. As this is the case, the curcumin will reduce gold at the [111] and

[110] faces which are not covered by silver and exposed towards the cetyl chains of

CTAB where curcumin itself is embedded, thus elongation occurs in the 110 direction.
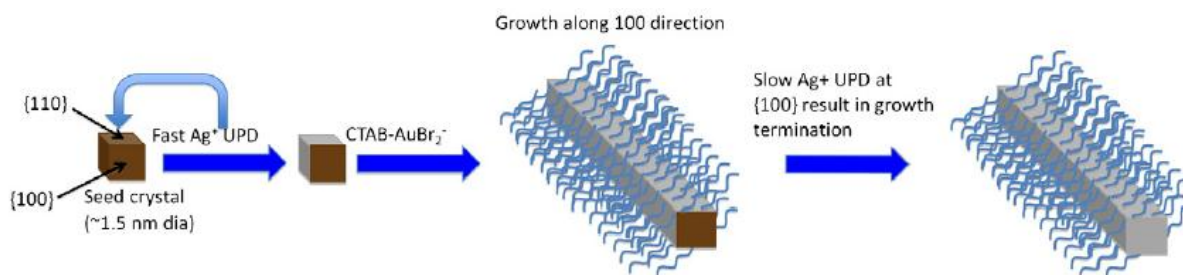


**Scheme 4.3: One of the proposed mechanisms that explain the role of silver in the silver-assisted, seed-mediated method of gold nanorod synthesis.[93]**

## 2. Morphology of gold nanorods: Curcumin versus ascorbic acid

➢ In sample 5, citrate-capped Au seed is used, for all the others we used CTAB-

capped Au seed solution.

**Table 4.6: Concentrations of reactants in growth solutions under different reaction conditions**

|  | [CTAB] mM | [Au] $_{seed}$ $10^{-7}$ M | [Au $^{3+}$] mM | [AgNO$_3$] $10^{-5}$ M | [curumin] mM |
|---|---|---|---|---|---|
| 4 | 95 | 1.25 | 0.4 | 6 | 6 |
| 5 | 50 | 6.25 | 0.5 | - | 3 |
| 6 | 16 | 0.125 | 0.4 | - | 1.2 |
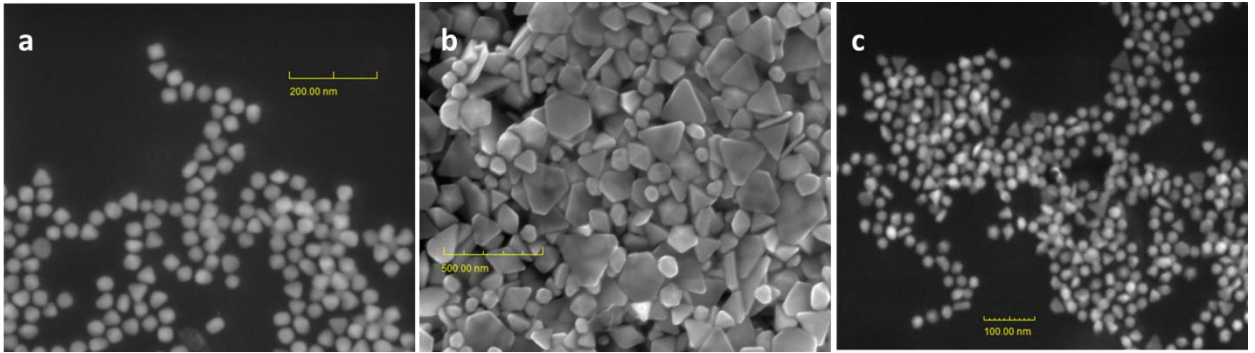
**Figure 4.24: SEM images of samples (a) 4, (b) 5, (c) 6**
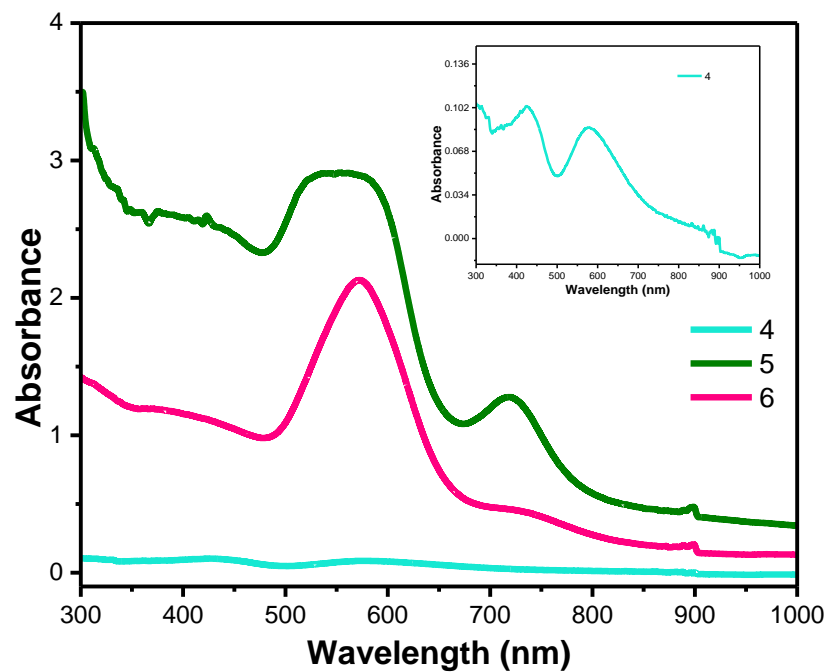


**Figure 4.25: UV-Vis spectra of samples 4, 5, and 6**

As stated earlier, the CTAB capped Au seeds are faceted with the most stable

[111] face in solvent[220] and CTAB molecules appear to bind more strongly to the

[100] than the [111] faces[114]. Thus, it has been suggested that lower CTAB and

higher AA concentration conditions that would favor the faster formation and

deposition of $Au^0$ onto the [111] faces, leading to their disappearance and the formation of [100] faces leading to the formation of the cubic shapes[213].

Good yield of Cubic shaped nanostructures were claimed to be formed also at low [AA] conditions, such as for [AA] = 1.6 × [$Au^{3+}$], if a small quantity of $AgNO_3$ were added to the system. This condition seemed to hold true for curcumin in sample 4 (Fig. 4.24a) which showed roughly equal amounts of cubes and triangles. For sample 5(fig. 4.24 b) where [CTAB] is ~6 times in other samples, we don't see any rods at all, but rather large triangular and hexagonal sheets and irregular shapes appear. Sample 6 looked pretty similar to sample 11cur (fig. 4.24c). When AA was used instead of curcumin under the same conditions in samples 4, 5, and 6, branched particles were obtained [213] but none gave such morphology when curcumin was utilized. The emission and excitation spectra further establish curcumin conjugation and formation of gold nanoparticles (see Fig. 4.26 and 4.27).
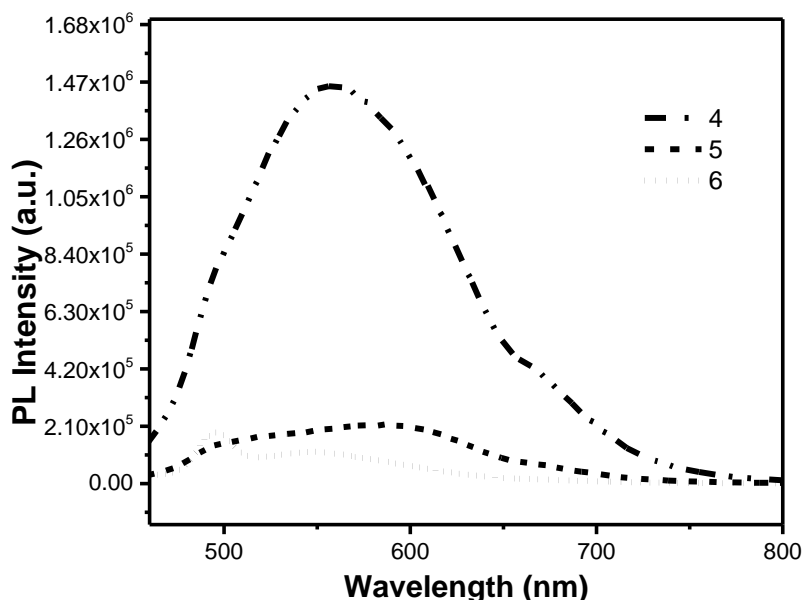


**Figure 4.26: Photoluminescence (emission) spectra of 4, 5 and 6 at excitation wavelength 425 nm**
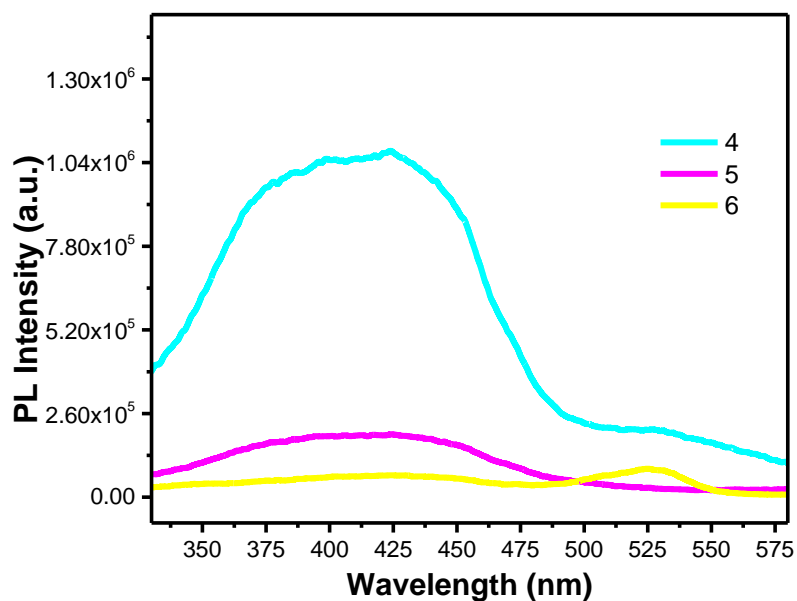
**Figure 4.27: Excitation spectra of 4, 5 and 6 at emission wavelength 610 nm**

## 3. Gold nanorods prepared from curcumin conjugated gold nanoparticles

Under different reaction conditions, the curcumin conjugated nanoparticles S(I) (fig. S3 and S4 for UV-Vis and SEM) confirmed to be a good candidate for nanorods formation if used as the seed solution. Very few nanorods were observed in a pool of spheres (50 nm on average) and triangular sheets (sample 1@S(I), fig. 4.28a). Increasing the seed solution 10 times in sample 2@S(I) didn't induce significant changes. At much higher CTAB concentration (increase by ~6 folds) and lower curcumin concentrations (12 times higher), @S(I) shows thin and long gold nanorods (high AR) in a relatively higher yield than that observed for 1@S(I) and 2@S(I).

All samples show a peak around 540 nm to the spherical NPs that have almost similar sizes and to probably the transverse absorption of the nanorods (fig. 4.29). On the other hand, low AR gold NRs will either appear as small broad bands reflecting the low yield and broadness of distribution, and for very low yields, it'll be hard to visualise any.

107

**Table 4.7: Concentrations of reactants in growth solutions under different reaction conditions**

|  | [CTAB] mM | [Au$^{3+}$] mM | [curumin] mM | Volume µL (Au)$_{seed}$ |
|---|---|---|---|---|
| 1@S(I) | 16 | 0.2 | 6 | 0.5 |
| 2@S(I) | 16 | 0.2 | 6 | 5 |
| 3@S(I) | 100 | 0.25 | 0.533 | 4 |
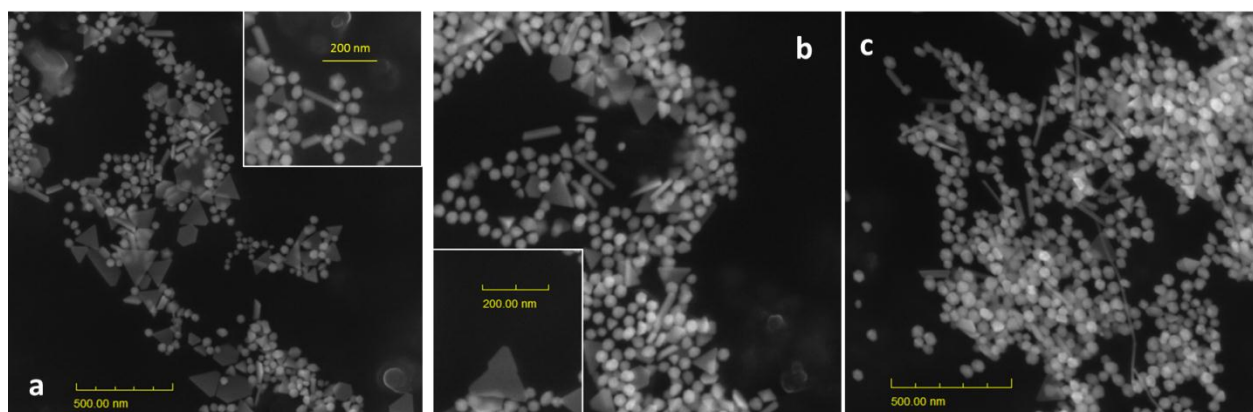


**Figure 4.28: SEM images of (a)1@S(I),  (b)2@S(I),  and (c) 3@S(I)**
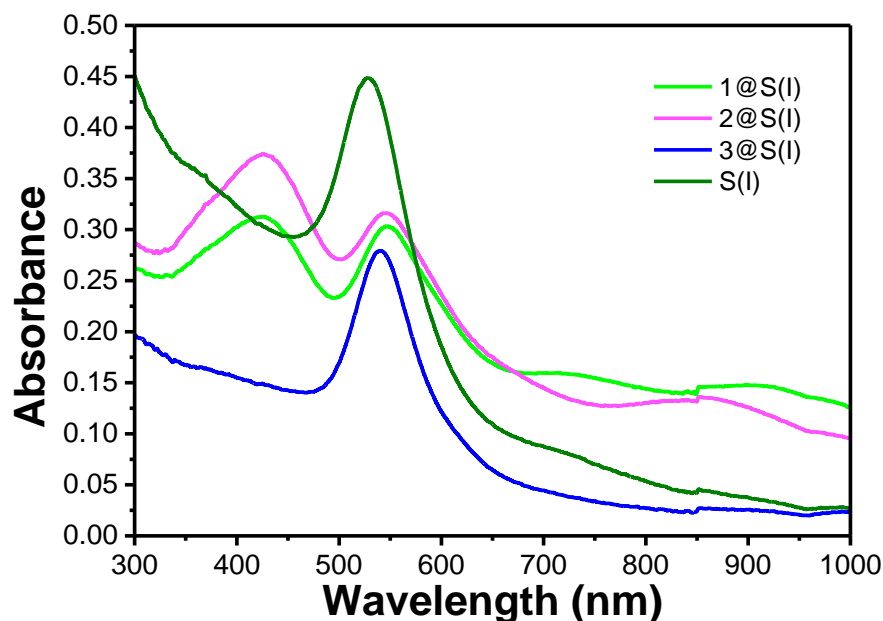
**Figure 4.29: UV-Vis spectra of samples 1@S(I), 2@S(I), and 3@S(I)**

As for 1@S(I) and 2@S(I) samples (fig. 4.29) we clearly see the absorption of curcumin at around 420 nm another at 548 nm as reffered before to the spherical particles and transverse absorption of NRs. The longitudinal plasmon band of 1@S(I) and 2@S(I) seems to be situated at 733 nm and 855 nm respectively.

## 4. Testing gold nanoparticle for nuleic acid sensing

For applications in sensing we tested the smaller gold nanoparticles prepared directly from curcumin rather than using gold nanorods, which indeed have also similar potential. The SEM images of gold nanoparticles (fig. 4.30) reveal small undefined shapes in the range size 20nm-50 nm that seem like aggregations of the gold NPs.
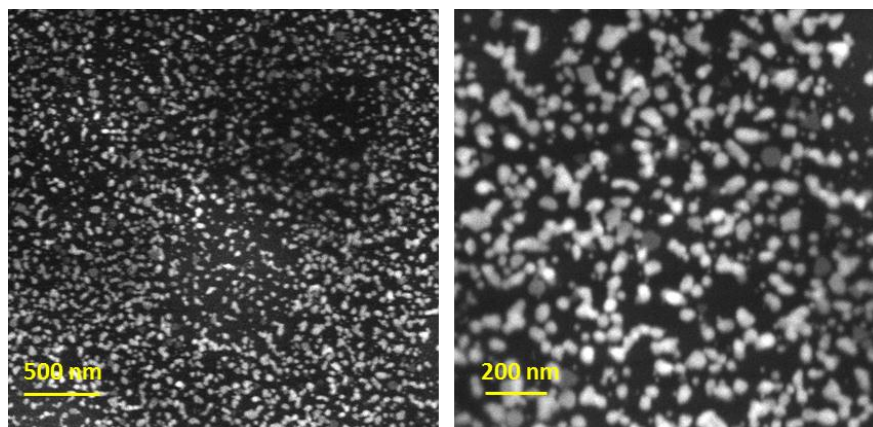
**Figure 4.30: SEM images of curcumin conjugated NPs**

To measure resonance Rayleigh scattering spectra, synchronous fluorescence spectra were obtained by simultaneously scanning excitation and emission monochromators over the range 220 – 600 nm with wavelength interval ($\Delta\lambda$) in synchronous fluorescence scan mode. The resonance light scattering intensity was measured in the form of synchronous fluorescence scan (SFS) intensity. In the field of nanoparticles research and analytical chemistry, Resonance Rayleigh Scattering (RRS) or surface Plasmon resonance (SPR) is getting utilized [221]. The principle behind this phenomenon is elastic scattering. RRS is produced when the wavelength of Rayleigh scattering is located at or close to the molecular absorption band. When the analyte interacts with the probe, the intensity of RRS is greatly increased.

Fig. 4.31a depicts RRS spectra of curcumin conjugated Au NPs with $Al^{3+}$, of DNA with $Al^{3+}$, and of curcumin Au NPs in the presence of $Al^{3+}$ and increasing concentrations of DNA. DNA along with $Al^{3+}$ did not have much RRS intensity, and presence of Au NPs along with $Al^{3+}$ had even lower RRS intensity. However, when DNA was mixed with $Al^{3+}$ and curucmin conjugated Au NPs a significant increase in SFS intensity was observed compared to the mentioned combinations. This

enhancement increased linearly with increasing DNA concentrations which indicates there is a strong interaction between curucmin conjugated Au NPs-$Al^{3+}$ and DNA. It is reported earlier that $Al^{3+}$ forms an adduct with the double stranded DNA [222] through both phosphate groups and base residues sites [223]. The curucmin conjugated Au NPs formed large aggregates which caused the increase in RRS intensity. The aggregation of gold nanoparticles with DNA is well known in literature[224-225]. When the analyte DNA was replaced with RNA, similar results were obtained as depicted in Fig. 4.32a. Both DNA and RNA showed linear increase which fitted well (high correlation coefficients $R^2 = 0.97$ and 0.996 respectively) into linear equations given in Fig. 4.31b and fig. 4.32b respectively. The good correlation coefficients render the present method eligible for the determination of DNA concentrations in the range 3.33μg/mL – 100μg/mL. For lower concentrations of DNA and RNA the sensitivity of the gold nanoparticles was not high and didn't show a systematic trend.
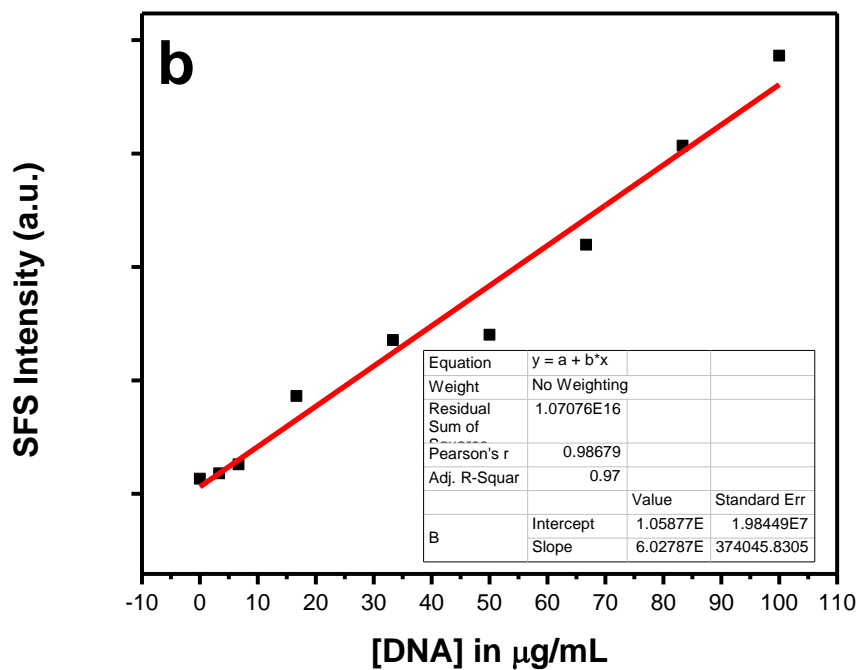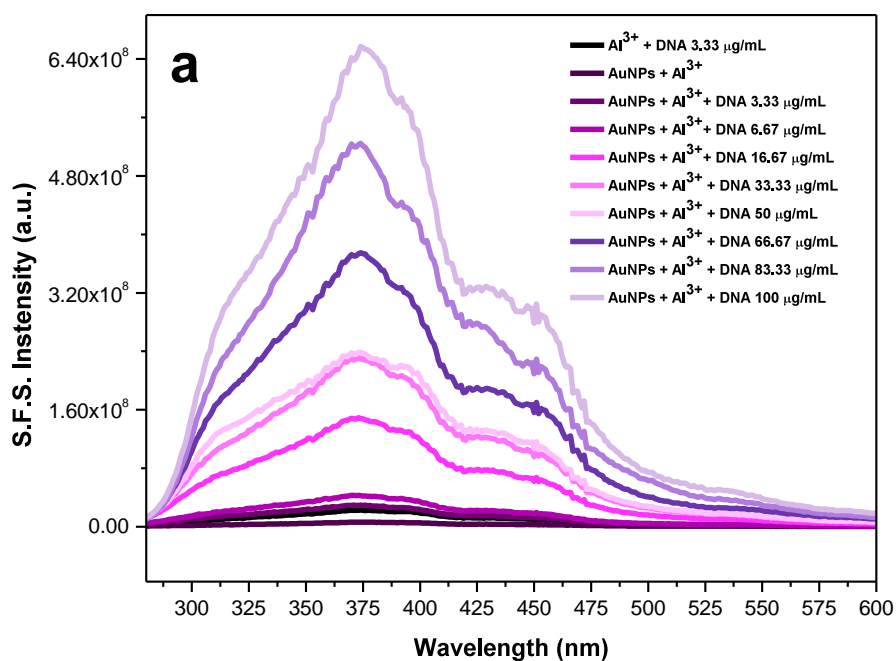
**Figure 4.31: (a) Resonance Rayleigh Scattering spectra of curcumin conjugated Au NPs with increasing concentration of DNA and in the presence of aluminum nitrate; (b) Linear fit of Fig. 4.30a with $R^2$ = 0.97**
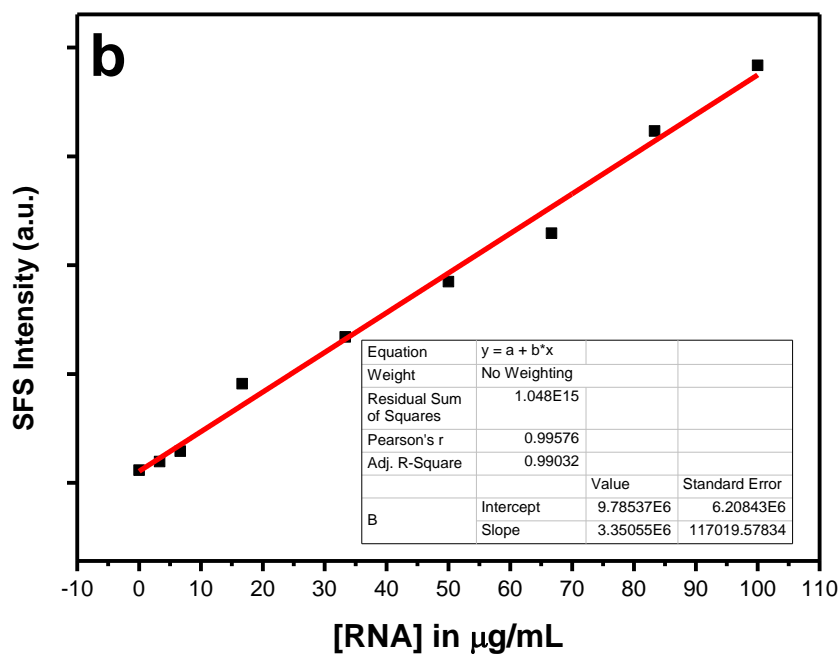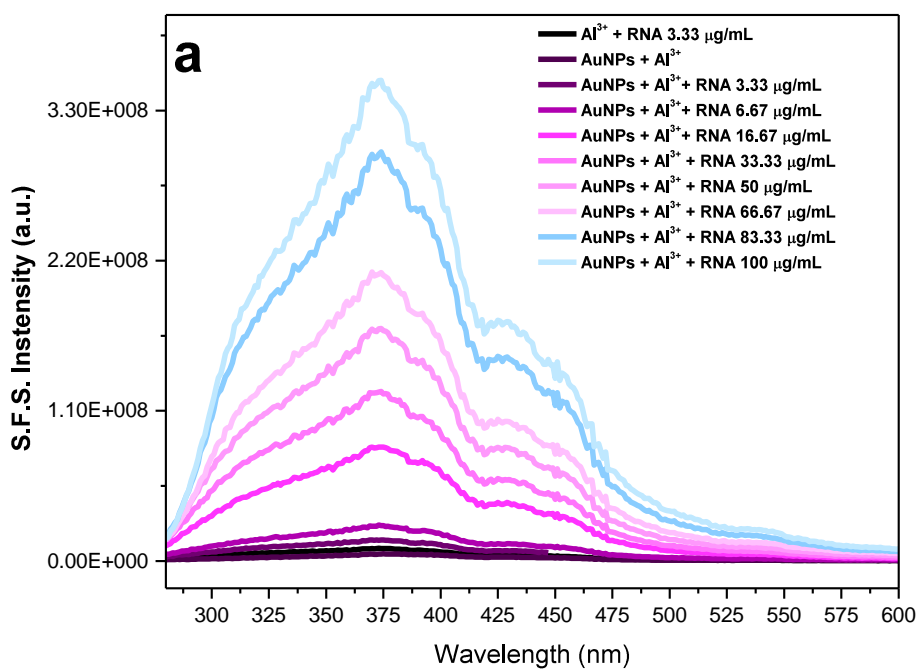
**Figure 4.32: (a) Resonance Rayleigh Scattering spectra of curcumin conjugated Au NPs with increasing concentration of RNA and in the presence of aluminum nitrate; (b) linear fit of Fig. 4.32a with R$^2$ = 0.996**

The study on gold nanorods produced through reduction with curcumin seemed to stress the micelle-templated growth of nanorods as revealed by the direct witness of micelle formation under SEM. At the same time, the rational of curcumin being embedded into the alkyl chains of CTAB and its consequent reduction along the [110] direction complies with the mechanism of preferential binding of CTAB molecules onto certain facets of the gold NRs. The behavior of curcumin was affected by the choice of the capping agent used for the gold seeds. In the presence of silver, CTAB-capped gold seeds gave higher AR NRs than when citrate-capped seeds where used. In fact, silver hindered the formation of NRs upon using citrate-capped seeds which was attributed to an interaction between curcumin and silver. Such an interaction doesn't take place in case of CTAB-capped seeds since silver is found at the surface of seeds by forming Ag-Br pairs and curcumin is located among the hydrophobic part of CTAB. The outcome of varying seed curcumin concentrations separately was similar to results observed with AA as well. Although we tried different combinations, some of which are similar to those reported for AA reduced Au NRs, only one combination - preserving the condition of [reducing agent (AA or curcumin)] = $1.6 \times [Au^{3+}]$, -gave an expected cubic shape. The conjugation of curcumin into the different shapes of nanoparticles was confirmed by the fluorescence signature of curcumin. Curcumin conjugated nanoparticles proved to yield nanorods in principle. The RRS response for curcumin conjugated NPs showed a linear increase with increasing concentrations of RNA and DNA which rendered the method eligible for their determination in the concentration range 3.33μg/mL – 100μg/mL.

# CHAPTER V
# CONCLUSION

The synthesis of the curcumin-zinc oxide nanostructures need to be optimized to yield smaller monodisperse nanostructures. This will open the door for biomedical applications of the hybrid compound that also might be a potential solution addressing the bioavailability problem of curcumin. Once this goal is realized, several factors that affect photocatalysis can be studied; such as, effect of light intensity and wavelength, effect of co-occurring substances, effect of oxidizing agents/electron acceptor, effect of pH, etc. The development of this photo catalyst and the knowledge of the specific working parameters may open the door to a large-scale utilization of heterogeneous cost-effective photo catalysis via visible light to address water contamination and environmental pollution.

Prominent work have been done as demonstrated above on gold nanorods, however, these studies illustrate the lack of fundamental understanding of how the kinetic, thermodynamic, or other factors influence the underlying mechanism in these and other interesting systems. Thus, considerable research is needed to explore the mechanisms governing morphology and geometry control over particle growth as they are still not well understood. The ultimate goal behind using curcumin is to obtain nanorods synthesized through green chemistry and on the way of reaching such a goal, results should be analyzed carefully to gain more understanding of the formation process and the parameters affecting it for a better design of materials.

# REFERENCES

1. Shenhar, R.; Rotello, V. M., Nanoparticles: Scaffolds and Building Blocks. *Accounts of Chemical Research* **2003,** *36* (7), 549-561.

2. Ipe, B. I.; Yoosaf, K.; Thomas, K. G., Functionalized gold nanoparticles as phosphorescent nanomaterials and sensors. *Journal of the American Chemical Society* **2006,** *128* (6), 1907-1913.

3. Taylor-Pashow, K. M.; Della Rocca, J.; Huxford, R. C.; Lin, W., Hybrid nanomaterials for biomedical applications. *Chemical Communications* **2010,** *46* (32), 5832-5849.

4. Lebeau, B.; Sanchez, C., Sol-gel derived hybrid inorganic-organic nanocomposites for optics. *Current Opinion in Solid State and Materials Science* **1999,** *4* (1), 11-23.

5. Uboldi, C.; Bonacchi, D.; Lorenzi, G.; Hermanns, M. I.; Pohl, C.; Baldi, G.; Unger, R. E.; Kirkpatrick, C. J., Gold nanoparticles induce cytotoxicity in the alveolar type-II cell lines A549 and NCIH441. *Part Fibre Toxicol* **2009,** *6*, 18.

6. Connor, E. E.; Mwamuka, J.; Gole, A.; Murphy, C. J.; Wyatt, M. D., Gold nanoparticles are taken up by human cells but do not cause acute cytotoxicity. *Small* **2005,** *1* (3), 325-327.

7. Manson, J.; Kumar, D.; Meenan, B. J.; Dixon, D., Polyethylene glycol functionalized gold nanoparticles: the influence of capping density on stability in various media. *Gold bulletin* **2011,** *44* (2), 99-105.

8. Djurišić, A. B.; Leung, Y. H., Optical properties of ZnO nanostructures. *Small* **2006,** *2* (8-9), 944-961.

9. Nakamura, I.; Negishi, N.; Kutsuna, S.; Ihara, T.; Sugihara, S.; Takeuchi, K., Role of oxygen vacancy in the plasma-treated $TiO_2$ photocatalyst with visible light activity for NO removal. *Journal of Molecular Catalysis A: Chemical* **2000,** *161* (1), 205-212.

10. Ihara, T.; Miyoshi, M.; Iriyama, Y.; Matsumoto, O.; Sugihara, S., Visible-light-active titanium oxide photocatalyst realized by an oxygen-deficient structure and by nitrogen doping. *Applied Catalysis B: Environmental* **2003,** *42* (4), 403-409.

11. Liu, J.; Yang, R.; Li, S., Preparation and characterization of the $TiO_2$-$V_2O_5$ photocatalyst with visible-light activity. *Rare Metals* **2006,** *25* (6), 636-642.

12.     Qiu, R.; Zhang, D.; Mo, Y.; Song, L.; Brewer, E.; Huang, X.; Xiong, Y., Photocatalytic activity of polymer-modified ZnO under visible light irradiation. *Journal of hazardous materials* **2008,** *156* (1), 80-85.

13.     Song, L.; Qiu, R.; Mo, Y.; Zhang, D.; Wei, H.; Xiong, Y., Photodegradation of phenol in a polymer-modified TiO< sub> 2</sub> semiconductor particulate system under the irradiation of visible light. *Catalysis Communications* **2007,** *8* (3), 429-433.

14.     Liao, S. H.; Jhuo, H. J.; Cheng, Y. S.; Chen, S. A., Fullerene Derivative-Doped Zinc Oxide Nanofilm as the Cathode of Inverted Polymer Solar Cells with Low-Bandgap Polymer (PTB7-Th) for High Performance. *Advanced Materials* **2013,** *25* (34), 4766-4771.

15.     Li, Z.; Xiong, Y.; Xie, Y., Selected-control synthesis of ZnO nanowires and nanorods via a PEG-assisted route. *Inorganic chemistry* **2003,** *42* (24), 8105-8109.

16.     Hariharan, R.; Senthilkumar, S.; Suganthi, A.; Rajarajan, M., Photodynamic action of curcumin derived polymer modified ZnO nanocamposites. *Mater. Res. Bull* **2012,** *47*, 3090-3099.

17.     Könenkamp, R.; Word, R. C.; Schlegel, C., Vertical nanowire light-emitting diode. *Applied Physics Letters* **2004,** *85* (24), 6004-6006.

18.     Srinivasan, S. S.; Wade, J.; Stefanakos, E. K., Visible light photocatalysis via CdS/TiO 2 nanocomposite materials. *Journal of Nanomaterials* **2006,** *2006*.

19.     Hao, S.; Wu, J.; Huang, Y.; Lin, J., Natural dyes as photosensitizers for dye-sensitized solar cell. *Solar energy* **2006,** *80* (2), 209-214.

20.     A. Zyoud, N. Z.; Saadeddin, I.; Helal, M. H.; Campet, G.; Hakim, M.; Park, D. H.; Hilal, H. S., Alternative natural dyes in water purification: Anthocyanin as TiO2-sensitizer in methyl orange photo-degradation. *Solid State Sci* **2011,** *13*, 1268-1275,.

21.     Tennakone, K.; Bandara, J., Photocatalytic activity of dye-sensitized tin (IV) oxide nanocrystalline particles attached to zinc oxide particles: long distance electron transfer via ballistic transport of electrons across nanocrystallites. *Applied Catalysis A: General* **2001,** *208* (1), 335-341.

22.     Yamazaki, E.; Murayama, M.; Nishikawa, N.; Hashimoto, N.; Shoyama, M.; Kurita, O., Utilization of natural carotenoids as photosensitizers for dye-sensitized solar cells. *Solar Energy* **2007,** *81* (4), 512-516.

23.     Buddee, S.; Wongnawa, S.; Sriprang, P.; Sriwong, C., Curcumin-sensitized TiO2 for enhanced photodegradation of dyes under visible light. *Journal of Nanoparticle Research* **2014,** *16* (4), 1-21.

24.     Goel, A.; Kunnumakkara, A. B.; Aggarwal, B. B., Curcumin as "Curecumin": From kitchen to clinic. *Biochemical Pharmacology* **2008,** *75* (4), 787-809.

25.    Aggarwal, B. B.; Harikumar, K. B., Potential therapeutic effects of curcumin, the anti-inflammatory agent, against neurodegenerative, cardiovascular, pulmonary, metabolic, autoimmune and neoplastic diseases. *The International Journal of Biochemistry & Cell Biology* **2009,** *41* (1), 40-59.

26.    Srivastava, R. M.; Singh, S.; Dubey, S. K.; Misra, K.; Khar, A., Immunomodulatory and therapeutic activity of curcumin. *International Immunopharmacology* **2011,** *11* (3), 331-341.

27.    Anand, P.; Nair, H. B.; Sung, B.; Kunnumakkara, A. B.; Yadav, V. R.; Tekmal, R. R.; Aggarwal, B. B., Design of curcumin-loaded PLGA nanoparticles formulation with enhanced cellular uptake, and increased bioactivity< i> in vitro</i> and superior bioavailability< i> in vivo</i>. *Biochemical pharmacology* **2010,** *79* (3), 330-338.

28.    Kittitheeranun, P.; Sanchavanakit, N.; Sajomsang, W.; Dubas, S. T., Loading of curcumin in polyelectrolyte multilayers. *Langmuir* **2010,** *26* (10), 6869-6873.

29.    Bong, P.-H., Spectral and photophysical behaviors of curcumin and curcuminoids. *BULLETIN-KOREAN CHEMICAL SOCIETY* **2000,** *21* (1), 81-86.

30.    Janisch, R.; Gopal, P.; Spaldin, N. A., Transition metal-doped $TiO_2$ and ZnO—present status of the field. *Journal of Physics: Condensed Matter* **2005,** *17* (27), R657.

31.    Wahab, R.; Ansari, S. G.; Y.S. Kim; Seo, H. K.; Kim, G. S.; Khang, G.; Shin, H. S., *Mater. Res. Bull.* **2007,** *42*, 1640–1648.

32.    Nishio, J.; Tokumura, M.; Znad, H. T.; Kawase, Y., Photocatalytic decolorization of azo-dye with zinc oxide powder in an external UV light irradiation slurry photoreactor. *Journal of Hazardous materials* **2006,** *138* (1), 106-115.

33.    Li, Y.; Meng, G. W.; Zhang, L. D.; Philip, F., *Appl. Phys. Lett.* **2000,** *76*, 2011–2017.

34.    Omichi, K.; Kaiya, K.; Takahashi, N.; Nakamura, T.; Okamoto, S.; Yamamoto, H., Growth of ZnO thin films exhibiting room-temperature ultraviolet emission by means of atmospheric pressure vapor-phase epitaxy. *J. Mater. Chem.* **2001,** *11* (2), 262-263.

35.    Lam, S.-M.; Sin, J.-C.; Abdullah, A. Z.; Mohamed, A. R., Degradation of wastewaters containing organic dyes photocatalysed by zinc oxide: a review. *Desalination and Water Treatment* **2012,** *41* (1-3), 131-169.

36.    Ning, W. S.; Shen, H. Y.; Liu, H. Z., Study of the effect of preparation method on CuO–ZnO–Al2O3 catalyst. *Appl. Catal. A: Gen.* **2001,** *211*, 153–157.

37.    Shen, G.; Bando, Y.; Lee, C.-J., Synthesis and evolution of novel hollow ZnO urchins by a simple thermal evaporation process. *The Journal of Physical Chemistry B* **2005,** *109* (21), 10578-10583.

38.     Jiang, C.; Zhang, W.; Zou, G.; Yu, W.; Qian, Y., Precursor-induced hydrothermal synthesis of flowerlike cupped-end microrod bundles of ZnO. *The Journal of Physical Chemistry B* **2005,** *109* (4), 1361-1363.

39.     Z.Wang; Qian, X.; Yin, J.; Zh, Z., *Langmuir* **2004,** *20*, 3441–3448.

40.     Gao, P. X.; Ding, Y.; Mai, W.; Hughes, W. L.; Lao, C.; Wang, Z. L., Conversion of zinc oxide nanobelts into superlattice-structured nanohelices. *Science* **2005,** *309* (5741), 1700-1704.

41.     Zhang, J.; Yang, Y.; Xu, B.; Jiang, F.; Li, J., Shape-controlled synthesis of ZnO nano-and micro-structures. *Journal of crystal growth* **2005,** *280* (3), 509-515.

42.     Lao, J.; Huang, J.; Wang, D.; Ren, Z., ZnO nanobridges and nanonails. *Nano Letters* **2003,** *3* (2), 235-238.

43.     Ganesh, T.; Kim, J. H.; Yoon, S. J.; Kil, B.-H.; Maldar, N. N.; Han, J. W.; Han, S.-H., Photoactive curcumin-derived dyes with surface anchoring moieties used in ZnO nanoparticle-based dye-sensitized solar cells. *Materials Chemistry and Physics* **2010,** *123* (1), 62-66.

44.     Patra, D.; El Khoury, E.; Ahmadieh, D.; Darwish, S.; Tafech, R. M., Effect of Curcumin on Liposome: Curcumin as a Molecular Probe for Monitoring Interaction of Ionic Liquids with 1, 2-Dipalmitoyl-sn-Glycero-3-Phosphocholine Liposome. *Photochemistry and photobiology* **2012,** *88* (2), 317-327.

45.     Zhou, S.-S.; Xue, X.; Wang, J.-F.; Dong, Y.; Jiang, B.; Wei, D.; Wan, M.-L.; Jia, Y., Synthesis, optical properties and biological imaging of the rare earth complexes with curcumin and pyridine. *J. Mater. Chem.* **2012,** *22* (42), 22774-22780.

46.     Ciszewski, A.; Milczarek, G.; Lewandowska, B.; Krutowski, K., Electrocatalytic properties of electropolymerized Ni (II) curcumin complex. *Electroanalysis* **2003,** *15* (5-6), 518-523.

47.     Renfrew, A. K.; Bryce, N. S.; Hambley, T. W., Delivery and release of curcumin by a hypoxia-activated cobalt chaperone: a XANES and FLIM study. *Chemical Science* **2013,** *4* (9), 3731-3739.

48.     Caruso, F.; Rossi, M.; Benson, A.; Opazo, C.; Freedman, D.; Monti, E.; Gariboldi, M. B.; Shaulky, J.; Marchetti, F.; Pettinari, R., Ruthenium–arene complexes of curcumin: X-ray and density functional theory structure, synthesis, and spectroscopic characterization, in vitro antitumor activity, and DNA docking studies of (p-cymene) Ru (curcuminato) chloro. *Journal of medicinal chemistry* **2012,** *55* (3), 1072-1081.

49.     Khalil, M. I.; Al-Qunaibit, M. M.; Al-zahem, A. M.; Labis, J. P., Synthesis and characterization of ZnO nanoparticles by thermal decomposition of a curcumin zinc complex. *Arabian Journal of Chemistry* **2013**.

50.     Zayats, M.; Baron, R.; Popov, I.; Willner, I., Biocatalytic Growth of Au Nanoparticles:  From Mechanistic Aspects to Biosensors Design. *Nano Letters* **2004,** *5* (1), 21-25.

51.     Suzuki, D.; Kawaguchi, H., Modification of Gold Nanoparticle Composite Nanostructures Using Thermosensitive Core−Shell Particles as a Template. *Langmuir* **2005,** *21* (18), 8175-8179.

52.     Daniel, M.-C.; Astruc, D., Gold Nanoparticles:  Assembly, Supramolecular Chemistry, Quantum-Size-Related Properties, and Applications toward Biology, Catalysis, and Nanotechnology. *Chemical Reviews* **2003,** *104* (1), 293-346.

53.     Hu, M.; Chen, J.; Li, Z.-Y.; Au, L.; Hartland, G. V.; Li, X.; Marquez, M.; Xia, Y., Gold nanostructures: engineering their plasmonic properties for biomedical applications. *Chemical Society Reviews* **2006,** *35* (11), 1084-1094.

54.     Wei, W.; Li, S.; Qin, L.; Xue, C.; Millstone, J. E.; Xu, X.; Schatz, G. C.; Mirkin, C. A., Surface Plasmon-Mediated Energy Transfer in Heterogap Au− Ag Nanowires. *Nano letters* **2008,** *8* (10), 3446-3449.

55.     Murphy, C. J., Spatial Control of Chemistry on the Inside and Outside of Inorganic Nanocrystals. *ACS Nano* **2009,** *3* (4), 770-774.

56.     Tabor, C.; Van Haute, D.; El-Sayed, M. A., Effect of Orientation on Plasmonic Coupling between Gold Nanorods. *ACS Nano* **2009,** *3* (11), 3670-3678.

57.     Wiley, B.; Sun, Y.; Xia, Y., Synthesis of Silver Nanostructures with Controlled Shapes and Properties. *Accounts of Chemical Research* **2007,** *40* (10), 1067-1076.

58.     Yu; Chang, S.-S.; Lee, C.-L.; Wang, C. R. C., Gold Nanorods:  Electrochemical Synthesis and Optical Properties. *The Journal of Physical Chemistry B* **1997,** *101* (34), 6661-6664.

59.     Gao, H.; Henzie, J.; Odom, T. W., Direct Evidence for Surface Plasmon-Mediated Enhanced Light Transmission through Metallic Nanohole Arrays. *Nano Letters* **2006,** *6* (9), 2104-2108.

60.     Ni, W.; Ambjörnsson, T.; Apell, S. P.; Chen, H.; Wang, J., Observing Plasmonic−Molecular Resonance Coupling on Single Gold Nanorods. *Nano Letters* **2009,** *10* (1), 77-84.

61.     Dieringer, J. A.; Wustholz, K. L.; Masiello, D. J.; Camden, J. P.; Kleinman, S. L.; Schatz, G. C.; Van Duyne, R. P., Surface-Enhanced Raman Excitation Spectroscopy of a Single Rhodamine 6G Molecule. *Journal of the American Chemical Society* **2008,** *131* (2), 849-854.

62.     Chang, S.-S.; Shih, C.-W.; Chen, C.-D.; Lai, W.-C.; Wang, C. R. C., The Shape Transition of Gold Nanorods. *Langmuir* **1998,** *15* (3), 701-709.

63.     Hubert, F.; Testard, F.; Spalla, O., Cetyltrimethylammonium Bromide Silver Bromide Complex as the Capping Agent of Gold Nanorods. *Langmuir* **2008,** *24* (17), 9219-9222.

64.     Jin, R.; Cao, Y.; Mirkin, C. A.; Kelly, K. L.; Schatz, G. C.; Zheng, J. G., Photoinduced Conversion of Silver Nanospheres to Nanoprisms. *Science* **2001,** *294* (5548), 1901-1903.

65.     Jin, R.; Charles Cao, Y.; Hao, E.; Metraux, G. S.; Schatz, G. C.; Mirkin, C. A., Controlling anisotropic nanoparticle growth through plasmon excitation. *Nature* **2003,** *425* (6957), 487-490.

66.     Liu; Guyot-Sionnest, P., Synthesis and Optical Characterization of Au/Ag Core/Shell Nanorods. *The Journal of Physical Chemistry B* **2004,** *108* (19), 5882-5888.

67.     Pérez-Juste, J.; Pastoriza-Santos, I.; Liz-Marzán, L. M.; Mulvaney, P., Gold nanorods: Synthesis, characterization and applications. *Coordination Chemistry Reviews* **2005,** *249* (17–18), 1870-1901.

68.     Lu, X.; Tuan, H.-Y.; Chen, J.; Li, Z.-Y.; Korgel, B. A.; Xia, Y., Mechanistic Studies on the Galvanic Replacement Reaction between Multiply Twinned Particles of Ag and HAuCl4 in an Organic Medium. *Journal of the American Chemical Society* **2007,** *129* (6), 1733-1742.

69.     Burgin, J.; Liu, M.; Guyot-Sionnest, P., Dielectric Sensing with Deposited Gold Bipyramids. *The Journal of Physical Chemistry C* **2008,** *112* (49), 19279-19282.

70.     Hill, H. D.; Millstone, J. E.; Banholzer, M. J.; Mirkin, C. A., The Role Radius of Curvature Plays in Thiolated Oligonucleotide Loading on Gold Nanoparticles. *ACS Nano* **2009,** *3* (2), 418-424.

71.     Smith, D. K.; Miller, N. R.; Korgel, B. A., Iodide in CTAB Prevents Gold Nanorod Formation. *Langmuir* **2009,** *25* (16), 9518-9524.

72.     Khalavka, Y.; Becker, J.; Sönnichsen, C., Synthesis of Rod-Shaped Gold Nanorattles with Improved Plasmon Sensitivity and Catalytic Activity. *Journal of the American Chemical Society* **2009,** *131* (5), 1871-1875.

73.     Kawasaki, H.; Nishimura, K.; Arakawa, R., Influence of the Counterions of Cetyltrimetylammonium Salts on the Surfactant Adsorption onto Gold Surfaces and the Formation of Gold Nanoparticles. *The Journal of Physical Chemistry C* **2007,** *111* (6), 2683-2690.

74.     Garg, N.; Scholl, C.; Mohanty, A.; Jin, R., The Role of Bromide Ions in Seeding Growth of Au Nanorods. *Langmuir* **2010,** *26* (12), 10271-10276.

75.     Eustis, S.; El-Sayed, M., Aspect Ratio Dependence of the Enhanced Fluorescence Intensity of Gold Nanorods: Experimental and Simulation Study. *The Journal of Physical Chemistry B* **2005,** *109* (34), 16350-16356.

76.     Jena, B. K.; Raj, C. R., Shape-Controlled Synthesis of Gold Nanoprism and Nanoperiwinkles with Pronounced Electrocatalytic Activity. *The Journal of Physical Chemistry C* **2007,** *111* (42), 15146-15153.

77.     Yoo, H.; Millstone, J. E.; Li, S.; Jang, J.-W.; Wei, W.; Wu, J.; Schatz, G. C.; Mirkin, C. A., Core−Shell Triangular Bifrustums. *Nano Letters* **2009,** *9* (8), 3038-3041.

78.     Ming, T.; Feng, W.; Tang, Q.; Wang, F.; Sun, L.; Wang, J.; Yan, C., Growth of Tetrahexahedral Gold Nanocrystals with High-Index Facets. *Journal of the American Chemical Society* **2009,** *131* (45), 16350-16351.

79.     Nikoobakht, B.; El-Sayed, M. A., Preparation and growth mechanism of gold nanorods (NRs) using seed-mediated growth method. *Chemistry of Materials* **2003,** *15* (10), 1957-1962.

80.     Jana, N. R.; Gearheart, L.; Murphy, C. J., Wet Chemical Synthesis of High Aspect Ratio Cylindrical Gold Nanorods. *The Journal of Physical Chemistry B* **2001,** *105* (19), 4065-4067.

81.     Kim, F.; Song, J. H.; Yang, P., Photochemical synthesis of gold nanorods. *Journal of the American Chemical Society* **2002,** *124* (48), 14316-14317.

82.     Kim, J. U.; Cha, S. H.; Shin, K.; Jho, J. Y.; Lee, J. C., Preparation of Gold Nanowires and Nanosheets in Bulk Block Copolymer Phases under Mild Conditions. *Advanced Materials* **2004,** *16* (5), 459-464.

83.     Vasilev, K.; Zhu, T.; Wilms, M.; Gillies, G.; Lieberwirth, I.; Mittler, S.; Knoll, W.; Kreiter, M., Simple, One-Step Synthesis of Gold Nanowires in Aqueous Solution. *Langmuir* **2005,** *21* (26), 12399-12403.

84.     Halder, A.; Ravishankar, N., Ultrafine Single-Crystalline Gold Nanowire Arrays by Oriented Attachment. *Advanced Materials* **2007,** *19* (14), 1854-1858.

85.     Shao, Y.; Jin, Y.; Dong, S., Synthesis of gold nanoplates by aspartate reduction of gold chloride. *Chemical Communications* **2004,** (9), 1104-1105.

86.     Ha, T. H.; Koo, H.-J.; Chung, B. H., Shape-Controlled Syntheses of Gold Nanoprisms and Nanorods Influenced by Specific Adsorption of Halide Ions. *The Journal of Physical Chemistry C* **2006,** *111* (3), 1123-1130.

87.     Millstone, J. E.; Park, S.; Shuford, K. L.; Qin, L.; Schatz, G. C.; Mirkin, C. A., Observation of a Quadrupole Plasmon Mode for a Colloidal Solution of Gold Nanoprisms. *Journal of the American Chemical Society* **2005,** *127* (15), 5312-5313.

88.     Jin, R.; Egusa, S.; Scherer, N. F., Thermally-Induced Formation of Atomic Au Clusters and Conversion into Nanocubes. *Journal of the American Chemical Society* **2004,** *126* (32), 9900-9901.

89.     Seo, D.; Park, J. C.; Song, H., Polyhedral Gold Nanocrystals with Oh Symmetry:  From Octahedra to Cubes. *Journal of the American Chemical Society* **2006,** *128* (46), 14863-14870.

90.     Li, C.; Shuford, K. L.; Park, Q. H.; Cai, W.; Li, Y.; Lee, E. J.; Cho, S. O., High-Yield Synthesis of Single-Crystalline Gold Nano-octahedra. *Angewandte Chemie International Edition* **2007,** *46* (18), 3264-3268.

91.     Chen, H. M.; Hsin, C. F.; Liu, R.-S.; Lee, J.-F.; Jang, L.-Y., Synthesis and Characterization of Multi-Pod-Shaped Gold/Silver Nanostructures. *The Journal of Physical Chemistry C* **2007,** *111* (16), 5909-5914.

92.     Xie, J.; Lee, J. Y.; Wang, D. I. C., Seedless, Surfactantless, High-Yield Synthesis of Branched Gold Nanocrystals in HEPES Buffer Solution. *Chemistry of Materials* **2007,** *19* (11), 2823-2830.

93.     Murphy, C. J.; Thompson, L. B.; Chernak, D. J.; Yang, J. A.; Sivapalan, S. T.; Boulos, S. P.; Huang, J.; Alkilany, A. M.; Sisco, P. N., Gold nanorod crystal growth: From seed-mediated synthesis to nanoscale sculpting. *Current Opinion in Colloid & Interface Science* **2011,** *16* (2), 128-134.

94.     Haes, A. J.; Zou, S.; Schatz, G. C.; Van Duyne, R. P., Nanoscale optical biosensor: short range distance dependence of the localized surface plasmon resonance of noble metal nanoparticles. *The Journal of Physical Chemistry B* **2004,** *108* (22), 6961-6968.

95.     Orendorff, C. J.; Sau, T. K.; Murphy, C. J., Shape-Dependent Plasmon-Resonant Gold Nanoparticles. *Small* **2006,** *2* (5), 636-639.

96.     Jana, N. R.; Gearheart, L.; Murphy, C. J., Seeding growth for size control of 5-40 nm diameter gold nanoparticles. *Langmuir* **2001,** *17* (22), 6782-6786.

97.     Murphy, C. J.; Sau, T. K.; Gole, A. M.; Orendorff, C. J.; Gao, J.; Gou, L.; Hunyadi, S. E.; Li, T., Anisotropic metal nanoparticles: synthesis, assembly, and optical applications. *The Journal of Physical Chemistry B* **2005,** *109* (29), 13857-13870.

98.     Alvarez-Puebla, R.; Liz-Marzán, L. M.; García de Abajo, F. J., Light concentration at the nanometer scale. *The Journal of Physical Chemistry Letters* **2010,** *1* (16), 2428-2434.

99.     Fu, Y.; Zhang, J.; Lakowicz, J. R., Plasmon-enhanced fluorescence from single fluorophores end-linked to gold nanorods. *Journal of the American Chemical Society* **2010,** *132* (16), 5540-5541.

100.    Anker, J. N.; Hall, W. P.; Lyandres, O.; Shah, N. C.; Zhao, J.; Van Duyne, R. P., Biosensing with plasmonic nanosensors. *Nature materials* **2008,** *7* (6), 442-453.

101.    Murphy, C. J.; Gole, A. M.; Hunyadi, S. E.; Stone, J. W.; Sisco, P. N.; Alkilany, A.; Kinard, B. E.; Hankins, P., Chemical sensing and imaging with metallic nanorods. *Chemical Communications* **2008,** (5), 544-557.

102.    Huang, X.; El-Sayed, M. A., Gold nanoparticles: optical properties and implementations in cancer diagnosis and photothermal therapy. *Journal of Advanced Research* **2010,** *1* (1), 13-28.

103.    Murphy, C. J.; Gole, A. M.; Stone, J. W.; Sisco, P. N.; Alkilany, A. M.; Goldsmith, E. C.; Baxter, S. C., Gold nanoparticles in biology: beyond toxicity to cellular imaging. *Accounts of Chemical Research* **2008,** *41* (12), 1721-1730.

104.    Huang, X.; El-Sayed, I. H.; Qian, W.; El-Sayed, M. A., Cancer cell imaging and photothermal therapy in the near-infrared region by using gold nanorods. *Journal of the American Chemical Society* **2006,** *128* (6), 2115-2120.

105.    von Maltzahn, G.; Centrone, A.; Park, J. H.; Ramanathan, R.; Sailor, M. J.; Hatton, T. A.; Bhatia, S. N., SERS-coded gold nanorods as a multifunctional platform for densely multiplexed near-infrared imaging and photothermal heating. *advanced materials* **2009,** *21* (31), 3175-3180.

106.    Grzelczak, M.; Pérez-Juste, J.; Mulvaney, P.; Liz-Marzán, L. M., Shape control in gold nanoparticle synthesis. *Chemical Society Reviews* **2008,** *37* (9), 1783-1791.

107.    Xu, Q.; Bao, J.; Capasso, F.; Whitesides, G. M., Surface Plasmon Resonances of Free-Standing Gold Nanowires Fabricated by Nanoskiving. *Angewandte Chemie* **2006,** *118* (22), 3713-3717.

108.    Foss Jr, C. A.; Tierney, M. J.; Martin, C. R., Template synthesis of infrared-transparent metal microcylinders: comparison of optical properties with the predictions of effective medium theory. *The Journal of Physical Chemistry* **1992,** *96* (22), 9001-9007.

109.    Tian, M.; Wang, J.; Kurtz, J.; Mallouk, T. E.; Chan, M., Electrochemical growth of single-crystal metal nanowires via a two-dimensional nucleation and growth mechanism. *Nano Letters* **2003,** *3* (7), 919-923.

110.    Busbee, B. D.; Obare, S. O.; Murphy, C. J., An Improved Synthesis of High-Aspect-Ratio Gold Nanorods. *Advanced Materials* **2003,** *15* (5), 414-416.

111.    Liu, M.; Guyot-Sionnest, P., Mechanism of silver (I)-assisted growth of gold nanorods and bipyramids. *The Journal of Physical Chemistry B* **2005,** *109* (47), 22192-22200.

112.     Sau, T. K.; Murphy, C. J., Seeded high yield synthesis of short Au nanorods in aqueous solution. *Langmuir* **2004,** *20* (15), 6414-6420.

113.     Wu, H.-Y.; Huang, W.-L.; Huang, M. H., Direct High-Yield Synthesis of High Aspect Ratio Gold Nanorods. *Crystal Growth & Design* **2007,** *7* (4), 831-835.

114.     Johnson, C. J.; Dujardin, E.; Davis, S. A.; Murphy, C. J.; Mann, S., Growth and form of gold nanorods prepared by seed-mediated, surfactant-directed synthesis. *Journal of Materials Chemistry* **2002,** *12* (6), 1765-1770.

115.     Wu, H.-Y.; Chu, H.-C.; Kuo, T.-J.; Kuo, C.-L.; Huang, M. H., Seed-Mediated Synthesis of High Aspect Ratio Gold Nanorods with Nitric Acid. *Chemistry of Materials* **2005,** *17* (25), 6447-6451.

116.     Meulenkamp, E. A., Synthesis and growth of ZnO nanoparticles. *The Journal of Physical Chemistry B* **1998,** *102* (29), 5566-5572.

117.     Xiong, H.-M.; Xie, D.-P.; Guan, X.-Y.; Tan, Y.-J.; Xia, Y.-Y., Water-stable blue-emitting ZnO@ polymer core–shell microspheres. *J. Mater. Chem.* **2007,** *17* (24), 2490-2496.

118.     Mishra, K.; Srivastava, R. K.; Prakash, S. G., Photoluminescence and photoconductivity studies of ZnO nanoparticles prepared by solid state reaction method. *J. Mater. Sci.: Mater. Electron* **2013,** *24*, 125 -134.

119.     El-Rahman, S. N. A.; Al-Jameel, S. S., Research Article Protection of Curcumin and Curcumin Nanoparticles against Cisplatin Induced Nephrotoxicity in Male Rats.

120.     Lu, Z.; Zhou, J.; Wang, A.; Wang, N.; Yang, X., Synthesis of aluminium-doped ZnO nanocrystals with controllable morphology and enhanced electrical conductivity. *Journal of Materials Chemistry* **2011,** *21* (12), 4161-4167.

121.     Xiong, H.-M.; Ma, R.-Z.; Wang, S.-F.; Xia, Y.-Y., Photoluminescent ZnO nanoparticles synthesized at the interface between air and triethylene glycol. *Journal of Materials Chemistry* **2011,** *21* (9), 3178-3182.

122.     Kolev, T. M.; Velcheva, E. A.; Stamboliyska, B. A.; Spiteller, M., DFT and experimental studies of the structure and vibrational spectra of curcumin. *International Journal of Quantum Chemistry* **2005,** *102* (6), 1069-1079.

123.     Tayyari, S.; Rahemi, H.; Nekoei, A.; Zahedi-Tabrizi, M.; Wang, Y., Vibrational assignment and structure of dibenzoylmethane: A density functional theoretical study. *Spectrochimica Acta Part A: Molecular and Biomolecular Spectroscopy* **2007,** *66* (2), 394-404.

124.     Xiong, H.-M., Photoluminescent ZnO nanoparticles modified by polymers. *Journal of Materials Chemistry* **2010,** *20* (21), 4251-4262.

125.    Djurišić, A.; Choy, W. C.; Roy, V. A. L.; Leung, Y. H.; Kwong, C. Y.; Cheah, K. W.; Gundu Rao, T.; Chan, W. K.; Fei Lui, H.; Surya, C., Photoluminescence and electron paramagnetic resonance of ZnO tetrapod structures. *Advanced Functional Materials* **2004,** *14* (9), 856-864.

126.    van Dijken, A.; Meulenkamp, E. A.; Vanmaekelbergh, D.; Meijerink, A., The kinetics of the radiative and nonradiative processes in nanocrystalline ZnO particles upon photoexcitation. *The Journal of Physical Chemistry B* **2000,** *104* (8), 1715-1723.
127.    Dijken, A. v.; Meulenkamp, E. A.; Vanmaekelbergh, D.; Meijerink, A., *J. Lumin.* **2000,** *454*, 87–89.

128.    Vanheusden, K.; Warren, W.; Seager, C.; Tallant, D.; Voigt, J.; Gnade, B., Mechanisms behind green photoluminescence in ZnO phosphor powders. *Journal of Applied Physics* **1996,** *79* (10), 7983-7990.

129.    Vanheusden, K.; Seager, C.; Warren, W. t.; Tallant, D.; Voigt, J., Correlation between photoluminescence and oxygen vacancies in ZnO phosphors. *Applied Physics Letters* **1996,** *68* (3), 403-405.

130.    Zhou, H.; Alves, H.; Hofmann, D.; Kriegseis, W.; Meyer, B.; Kaczmarczyk, G.; Hoffmann, A., Behind the weak excitonic emission of ZnO quantum dots: ZnO/Zn (OH) 2 core-shell structure. *Applied physics letters* **2002,** *80* (2), 210-212.

131.    Spanhel, L., Colloidal ZnO nanostructures and functional coatings: A survey. *Journal of sol-gel science and technology* **2006,** *39* (1), 7-24.

132.    Xiong, H. M.; Shchukin, D. G.; Möhwald, H.; Xu, Y.; Xia, Y. Y., Sonochemical synthesis of highly luminescent zinc oxide nanoparticles doped with magnesium (II). *Angewandte Chemie International Edition* **2009,** *48* (15), 2727-2731.

133.    Zhang, J.; Liu, H.; Wang, Z.; Ming, N.; Li, Z.; Biris, A. S., Polyvinylpyrrolidone-Directed Crystallization of ZnO with Tunable Morphology and Bandgap. *Advanced Functional Materials* **2007,** *17* (18), 3897-3905.

134.    Mousavi, S. H.; Haratizadeh, H.; Minaee, H., The effect of morphology and doping on photoluminescence of ZnO nanostructures. *Optics Communications* **2011,** *284* (14), 3558-3561.

135.    Wei, S.; Lian, J.; Jiang, Q., Controlling growth of ZnO rods by polyvinylpyrrolidone (PVP) and their optical properties. *Applied Surface Science* **2009,** *255* (15), 6978-6984.

136.    Patra, D.; Barakat, C.; Tafech, R. M., Study on effect of lipophilic curcumin on sub-domain IIA site of human serum albumin during unfolded and refolded states: a synchronous fluorescence spectroscopic study. *Colloids and Surfaces B: Biointerfaces* **2012,** *94*, 354-361.

137.    Patra, D.; Barakat, C., Synchronous fluorescence spectroscopic study of solvatochromic curcumin dye. *Spectrochimica Acta Part A: Molecular and Biomolecular Spectroscopy* **2011,** *79* (5), 1034-1041.

138.    A, S.; E, L.; M, R., *Bull World Health Organ* **2000,** *78* 1093.

139.    C, H.-R.; M, B.; A, S., *Int J Epidemiol* **1995,** *27* (4), 561.

140.    Xia, Y.; Liu, J., An overview on chronic arsenism via drinking water in PR China. *Toxicology* **2004,** *198* (1), 25-29.

141.    Saha, K., Review of arsenicosis in west Bengal, India—A clinical perspective. *Critical reviews in environmental science and technology* **2003,** *33* (2), 127-163.

142.    Welch, A. H.; Lico, M. S.; Hughes, J. L., Arsenic in ground water of the western United States. *Groundwater* **1988,** *26* (3), 333-347.

143.    Korte, N. E.; Fernando, Q., A review of arsenic (III) in groundwater. *Crit. Rev. Environ. Control,* **1991,** *21*, 1-11.

144.    Choong, T. S.; Chuah, T.; Robiah, Y.; Gregory Koay, F.; Azni, I., Arsenic toxicity, health hazards and removal techniques from water: an overview. *Desalination* **2007,** *217* (1), 139-166.

145.    Goldberg, S., Competitive adsorption of arsenate and arsenite on oxides and clay minerals. *Soil Science Society of America Journal* **2002,** *66* (2), 413-421.

146.    Saha, B.; Bains, R.; Greenwood, F., Physicochemical characterization of granular ferric hydroxide (GFH) for arsenic (V) sorption from water. *Separation science and technology* **2005,** *40* (14), 2909-2932.

147.    Borho, M.; Wilderer, P., Optimized removal of arsenate (III) by adaptation of oxidation and precipitation processes to the filtration step. *Water Science and Technology* **1996,** *34* (9), 25-31.

148.    Lee, H.; Choi, W., Photocatalytic oxidation of arsenite in TiO2 suspension: kinetics and mechanisms. *Environmental science & technology* **2002,** *36* (17), 3872-3878.

149.    Kim, Y.; Kim, C.; Choi, I.; Rengaraj, S.; Yi, J., Arsenic removal using mesoporous alumina prepared via a templating method. *Environmental science & technology* **2004,** *38* (3), 924-931.

150.    McNeill, L. S.; Edwards, M., Review of iron pipe corrosion in drinking water distribution systems. *J. AWWA* **2001,** *93* (7), 88-100.

151.    Hering, J. G.; Chen, P.-Y.; Wilkie, J. A.; Elimelech, M.; Liang, S., Arsenic removal by ferric chloride. *Journal-American Water Works Association* **1996,** *88* (4), 155-167.

152.    Pande, S. P.; Deshpande, L. S.; Patni, P.; Lutade, S., Arsenic removal studies in some ground waters of West Bengal, India. *Journal of Environmental Science & Health Part A* **1997,** *32* (7), 1981-1987.

153.    Pierce, M. L.; Moore, C. B., Adsorption of arsenite and arsenate on amorphous iron hydroxide. *Water Research* **1982,** *16* (7), 1247-1253.

154.    Matis, K. A.; Papadoyannis, I. N.; Zouboulis, A. I., Separation of germanium and arsenic ions from effluents by flotation techniques. *Int. J. Min. Process* **1987,** *21*, 83–92.

155.    Driehaus, W.; Jekel, M.; Hildebrandt, U., Granular ferric hydroxide – a new adsorbent for the removal of arsenic from natural water. *J. Water Supply: Res. Technol.–AQUA* **1998,** *47*, 30-35.

156.    C. Quan, G. K.; Bangster, D., Adsorption of sodium lauryl sulfate onto arsenic-bearing ferrihydrite. *Water Res.* **2001,** *35*, 478–484.

157.    Raven, K. P.; Jain, A.; Loeppert, R. H., Arsenite and arsenate adsorption on ferrihydrite: kinetics, equilibrium, and adsorption envelopes. *Environmental Science & Technology* **1998,** *32* (3), 344-349.

158.    Zeng, L., A method for preparing silica-containing iron (III) oxide adsorbents for arsenic removal. *Water research* **2003,** *37* (18), 4351-4358.

159.    Reed, B. E.; Vaughan, R.; Jiang, L., As (III), As (V), Hg, and Pb removal by Fe-oxide impregnated activated carbon. *Journal of Environmental Engineering* **2000,** *126* (9), 869-873.

160.    Zang, S.; Li, P.; Li, W.; Zhang, D.; Hamilton, A., Degradation mechanisms of benzo [< i> a</i>] pyrene and its accumulated metabolites by biodegradation combined with chemical oxidation. *Chemosphere* **2007,** *67* (7), 1368-1374.

161.    Thirunavukkarasu, O.; Viraraghavan, T.; Subramanian, K., Arsenic removal from drinking water using iron oxide-coated sand. *Water, air, and soil pollution* **2003,** *142* (1-4), 95-111.

162.    Haron, M.; Wan Yunus, W.; Yong, N.; Tokunaga, S., Sorption of arsenate and arsenate anions by iron (III)-poly (hydroxamic acid) complex. *Chemosphere* **1999,** *39* (14), 2459-2466.

163.    Meng, X.; Bang, S.; Korfiatis, G. P., Effects of silicate, sulfate, and carbonate on arsenic removal by ferric chloride. *Water Research* **2000,** *34* (4), 1255-1261.

164.    Min, J. H.; Hering, J. G., Arsenate sorption by Fe (III)-doped alginate gels. *Water Research* **1998,** *32* (5), 1544-1552.

165.    Peleanu, I.; Zaharescu, M.; Rau, I.; Crisan, M.; Jitianu, A.; Meghea, A., Nanocomposite materials for As (V) removal by magnetically intensified adsorption. *Separation science and technology* **2002,** *37* (16), 3693-3701.

166.    Katsoyiannis, I. A.; Zouboulis, A. I., Removal of arsenic from contaminated water sources by sorption onto iron-oxide-coated polymeric materials. *Water research* **2002,** *36* (20), 5141-5155.

167.    Daus, B.; Wennrich, R.; Weiss, H., Sorption materials for arsenic removal from water:: a comparative study. *Water Research* **2004,** *38* (12), 2948-2954.

168.    Huang, C.; Fu, P., Treatment of arsenic (V)-containing water by the activated carbon process. *Journal (Water Pollution Control Federation)* **1984**, 233-242.

169.    Gimbel, R.; Hobby, R., Discharge of arsenic and heavy metals from activated carbon filters during drinking water treatment. *BBR, Wasser Rohrbau* **2000,** *51*, 15-16.

170.    Leist, M.; Casey, R.; Caridi, D., The management of arsenic wastes: problems and prospects. *Journal of Hazardous Materials* **2000,** *76* (1), 125-138.

171.    Jekel, M., Actual problems related to inorganic water compounds. *Water Supply* **2002,** *2*, 1–9.

172.    Ruhland, A.; Jekel, M., Concept for an integrated evaluation of arsenic removal technologies: demonstrated in a case study. *Water Supply* **2002,** *2* (2), 267-274.

173.    Yang, W.; Li, Q.; Gao, S.; Shang, J. K., High efficient As (III) removal by self-assembled zinc oxide micro-tubes synthesized by a simple precipitation process. *Journal of materials science* **2011,** *46* (17), 5851-5858.

174.    Chiou, M.-S.; Li, H.-Y., Equilibrium and kinetic modeling of adsorption of reactive dye on cross-linked chitosan beads. *Journal of Hazardous Materials* **2002,** *93* (2), 233-248.

175.    Ho, Y.-S.; McKay, G., Pseudo-second order model for sorption processes. *Process Biochemistry* **1999,** *34* (5), 451-465.

176.    Fierro, V.; Torné-Fernández, V.; Montané, D.; Celzard, A., Adsorption of phenol onto activated carbons having different textural and surface properties. *Microporous and mesoporous materials* **2008,** *111* (1), 276-284.

177.    Ramamoorthy, J. W. M. S., Organic Chemicals in Natural Waters. **1984**.

178.    Kogevinas, M.; Becher, H.; Benn, T.; Bertazzi, P. A.; Boffetta, P.; Bueno-de-Mesqurta, H. B.; Coggon, D.; Colin, D.; Flesch-Janys, D.; Fingerhut, M., Cancer

mortality in workers exposed to phenoxy herbicides, chlorophenols, and dioxins an expanded and updated international cohort study. *American journal of epidemiology* **1997,** *145* (12), 1061-1075.

179.    Baek, S.; Goldstone, M.; Kirk, P.; Lester, J.; Perry, R., Phase distribution and particle size dependency of polycyclic aromatic hydrocarbons in the urban atmosphere. *Chemosphere* **1991,** *22* (5), 503-520.

180.    Grice, K.; Lu, H.; Atahan, P.; Asif, M.; Hallmann, C.; Greenwood, P.; Maslen, E.; Tulipani, S.; Williford, K.; Dodson, J., New insights into the origin of perylene in geological samples. *Geochimica et Cosmochimica Acta* **2009,** *73* (21), 6531-6543.

181.    Brun, G. L.; Vaidya, O. C.; Léger, M. G., Atmospheric deposition of polycyclic aromatic hydrocarbons to Atlantic Canada: geographic and temporal distributions and trends 1980-2001. *Environmental science & technology* **2004,** *38* (7), 1941-1948.

182.    Clemons, J.; Allan, L.; Marvin, C.; Wu, Z.; McCarry, B.; Bryant, D.; Zacharewski, T., Evidence of estrogen-and TCDD-like activities in crude and fractionated extracts of PM10 air particulate material using in vitro gene expression assays. *Environmental science & technology* **1998,** *32* (12), 1853-1860.

183.    Liu, X.; Zhang, G.; Jones, K. C.; Li, X.; Peng, X.; Qi, S., Compositional fractionation of polycyclic aromatic hydrocarbons (PAHs) in mosses (< i> Hypnum plumaeformae</i> WILS.) from the northern slope of Nanling Mountains, South China. *Atmospheric Environment* **2005,** *39* (30), 5490-5499.

184.    Freeman, D. J.; Cattell, F. C., Woodburning as a source of atmospheric polycyclic aromatic hydrocarbons. *Environmental Science & Technology* **1990,** *24* (10), 1581-1585.

185.    Shi, Z.; Tao, S.; Pan, B.; Fan, W.; He, X.; Zuo, Q.; Wu, S.; Li, B.; Cao, J.; Liu, W., Contamination of rivers in Tianjin, China by polycyclic aromatic hydrocarbons. *Environmental Pollution* **2005,** *134* (1), 97-111.

186.    Tan, Y. L.; Quanci, J. F.; Borys, R. D.; Quanci, M. J., Polycyclic aromatic hydrocarbons in smoke particles from wood and duff burning. *Atmospheric Environment. Part A. General Topics* **1992,** *26* (6), 1177-1181.

187.    Nielsen, T.; Seitz, B.; Ramdahl, T., Occurrence of nitro-PAH in the atmosphere in a rural area. *Atmospheric Environment (1967)* **1984,** *18* (10), 2159-2165.

188.    Mumford, J. L.; Williams, R. W.; Walsh, D. B.; Burton, R. M.; Svendsgaard, D. J.; Chuang, J. C.; Houk, V. S.; Lewtas, J., Indoor air pollutants from unvented kerosene heater emissions in mobile homes: studies on particles, semivolatile organics, carbon monoxide, and mutagenicity. *Environmental science & technology* **1991,** *25* (10), 1732-1738.

189.    Traynor, G. W.; Apte, M. G.; Sokol, H. A.; Chuang, J. C.; Tucker, W. G.; Mumford, J. L., Selected organic pollutant emissions from unvented kerosene space heaters. *Environmental science & technology* **1990,** *24* (8), 1265-1270.

190.    Vela, N.; Martínez-Menchón, M.; Navarro, G.; Pérez-Lucas, G.; Navarro, S., Removal of polycyclic aromatic hydrocarbons (PAHs) from groundwater by heterogeneous photocatalysis under natural sunlight. *Journal of Photochemistry and Photobiology A: Chemistry* **2012,** *232*, 32-40.

191.    Huang, C.; Dong, C.; Tang, Z., Advanced chemical oxidation: its present role and potential future in hazardous waste treatment. *Waste management* **1993,** *13* (5), 361-377.

192.    Woo, O.; Chung, W.; Wong, K.; Chow, A. T.; Wong, P., Photocatalytic oxidation of polycyclic aromatic hydrocarbons: Intermediates identification and toxicity testing. *Journal of hazardous materials* **2009,** *168* (2), 1192-1199.

193.    Rehman, S.; Ullah, R.; Butt, A.; Gohar, N., Strategies of making TiO$_2$ and ZnO visible light active. *Journal of Hazardous Materials* **2009,** *170* (2), 560-569.

194.    Sakthivel, S.; Neppolian, B.; Shankar, M.; Arabindoo, B.; Palanichamy, M.; Murugesan, V., Solar photocatalytic degradation of azo dye: comparison of photocatalytic efficiency of ZnO and TiO$_2$. *Solar Energy Materials and Solar Cells* **2003,** *77* (1), 65-82.

195.    Chen, C.-C., Degradation pathways of ethyl violet by photocatalytic reaction with ZnO dispersions. *Journal of Molecular Catalysis A: Chemical* **2007,** *264* (1), 82-92.

196.    Kansal, S.; Singh, M.; Sud, D., Studies on photodegradation of two commercial dyes in aqueous phase using different photocatalysts. *Journal of hazardous materials* **2007,** *141* (3), 581-590.

197.    Pare, B.; Jonnalagadda, S.; Tomar, H.; Singh, P.; Bhagwat, V., ZnO assisted photocatalytic degradation of acridine orange in aqueous solution using visible irradiation. *Desalination* **2008,** *232* (1), 80-90.

198.    Kou, J.; Li, Z.; Guo, Y.; Gao, J.; Yang, M.; Zou, Z., Photocatalytic degradation of polycyclic aromatic hydrocarbons in GaN: ZnO solid solution-assisted process: Direct hole oxidation mechanism. *Journal of Molecular Catalysis A: Chemical* **2010,** *325* (1), 48-54.

199.    Dass, S.; Muneer, M.; Gopidas, K., Photocatalytic degradation of wastewater pollutants. Titanium-dioxide-mediated oxidation of polynuclear aromatic hydrocarbons. *Journal of Photochemistry and Photobiology A: Chemistry* **1994,** *77* (1), 83-88.

200.    Sabate, J.; Bayona, J.; Solanas, A., Photolysis of PAHs in aqueous phase by UV irradiation. *Chemosphere* **2001,** *44* (2), 119-124.

201.    Wen, S.; Zhao, J.; Sheng, G.; Fu, J.; Peng, P. a., Photocatalytic reactions of pyrene at TiO< sub> 2</sub>/water interfaces. *Chemosphere* **2003,** *50* (1), 111-119.

202.    Carp, O.; Huisman, C. L.; Reller, A., Photoinduced reactivity of titanium dioxide. *Prog. Solid State Chem* **2004,** *32*, 33–177.

203.    Gaya, U. I.; Abdullah, A. H., Heterogeneous photocatalytic degradation of organic contaminants over titanium dioxide: A review of fundamentals, progress and problems. *J. Photochem. Photobio. C: Photochem. Rev.* **2008,** *9*, 1–12.

204.    In, J. P. H.; Bard, A. J.; Parsons, R.; (Eds.), J. J.; Inc., M. D., Standard Potentials m Aqueous Solution. *New York Basel* **1985**, 49.

205.    M. Anpo, T. S.; Kubokawa, Y., *Chem. Lett* **1985,** *1799.*

206.    Lepore, G. P.; Langford, C. H.; Vichova, J.; Vlček Jr, A., Photochemistry and picosecond absorption spectra of aqueous suspensions of a polycrystalline titanium dioxide optically transparent in the visible spectrum. *Journal of Photochemistry and Photobiology A: Chemistry* **1993,** *75* (1), 67-75.

207.    Jaeger, C. D.; Bard, A. J., Spin trapping and electron spin resonance detection of radical intermediates in the photodecomposition of water at titanium dioxide particulate systems. *Journal of Physical Chemistry* **1979,** *83* (24), 3146-3152.

208.    Fox, M. A.; Chen, C. C.; Younathan, J. N. N., *J. Org. Chem* **1984,** *49*, 1971.

209.    C. Guillard, H. D.; Hoang, V. C.; Pichat, P., J. Atmos. Chem. **1993,** *16*, 47.

210.    Dindar, B.; Içli, S., Unusual photoreactivity of zinc oxide irradiated by concentrated sunlight. *Journal of Photochemistry and Photobiology A: Chemistry* **2001,** *140* (3), 263-268.

211.    Theurich, J.; Bahnemann, D.; Vogel, R.; Ehamed, F.; Alhakimi, G.; Rajab, I., Photocatalytic degradation of naphthalene and anthracene: GC-MS analysis of the degradation pathway. *Research on chemical intermediates* **1997,** *23* (3), 247-274.

212.    Merrill, N. A.; Sethi, M.; Knecht, M. R., Structural and Equilibrium Effects of the Surface Passivant on the Stability of Au Nanorods. *ACS Applied Materials & Interfaces* **2013,** *5* (16), 7906-7914.

213.    Sau, T. K.; Murphy, C. J., Room Temperature, High-Yield Synthesis of Multiple Shapes of Gold Nanoparticles in Aqueous Solution. *Journal of the American Chemical Society* **2004,** *126* (28), 8648-8649.

214.    Sindhu, K.; Rajaram, A.; Sreeram, K.; Rajaram, R., Curcumin conjugated gold nanoparticle synthesis and its biocompatibility. *RSC Advances* **2014,** *4* (4), 1808-1818.

215.    Koeppl, S.; Solenthaler, C.; Caseri, W.; Spolenak, R., Towards a reproducible synthesis of high aspect ratio gold nanorods. *Journal of Nanomaterials* **2011,** *2011*, 15.

216.    Barnard, A. S.; Curtiss, L. A., Modeling the preferred shape, orientation and aspect ratio of gold nanorods. *Journal of Materials Chemistry* **2007,** *17* (31), 3315-3323.

217.    Hassan, P. A.; Yakhmi, J. V., Growth of Cationic Micelles in the Presence of Organic Additives. *Langmuir* **2000,** *16* (18), 7187-7191.

218.    Pérez-Juste, J.; Liz-Marzan, L.; Carnie, S.; Chan, D. Y.; Mulvaney, P., Electric-field-directed growth of gold nanorods in aqueous surfactant solutions. *Advanced Functional Materials* **2004,** *14* (6), 571-579.

219.    Patra, D.; Barakat, C., Unique role of ionic liquid [bmin][BF< sub> 4</sub>] during curcumin–surfactant association and micellization of cationic, anionic and non-ionic surfactant solutions. *Spectrochimica Acta Part A: Molecular and Biomolecular Spectroscopy* **2011,** *79* (5), 1823-1828.

220.    Petroski, J. M.; Wang, Z. L.; Green, T. C.; El-Sayed, M. A., Kinetically Controlled Growth and Shape Formation Mechanism of Platinum Nanoparticles. *The Journal of Physical Chemistry B* **1998,** *102* (18), 3316-3320.

221.    Long, X.; Zhang, H.; Bi, S., Frequency doubling scattering and second-order scattering spectra of phosphato-molybdate heteroply acid–protein system and their analytical application. *Spectrochimica Acta Part A: Molecular and Biomolecular Spectroscopy* **2004,** *60* (7), 1631-1636.

222.    Howard, J. M., The detection of DNA adducts (risk factors for DNA damage). A method for genomic DNA, the results and some effects of nutritional intervention. *Journal of Nutritional and Environmental Medicine* **2002,** *12* (1), 19-31.

223.    Zhang, R.-Y.; Liu, Y.; Pang, D.-W.; Cai, R.-X.; Qi, Y.-P., Spectroscopic and voltammetric study on the binding of aluminium (III) to DNA. *Analytical sciences* **2002,** *18* (7), 761-766.

224.    Sato, K.; Hosokawa, K.; Maeda, M., Rapid aggregation of gold nanoparticles induced by non-cross-linking DNA hybridization. *Journal of the American Chemical Society* **2003,** *125* (27), 8102-8103.

225.    Li, H.; Rothberg, L., Colorimetric detection of DNA sequences based on electrostatic interactions with unmodified gold nanoparticles. *Proceedings of the National Academy of Sciences of the United States of America* **2004,** *101* (39), 14036-14039.